



2016

THREE-DIMENSIONAL MICROSTRUCTURE-BASED MODELS FOR FATIGUE CRACK NUCLEATION AND FATIGUE CRACK BRANCHING IN HIGH STRENGTH AL ALLOYS

Lin Yang

University of Kentucky, ylining@gmail.com

Author ORCID Identifier:

<http://orcid.org/0000-0001-8278-7537>

Digital Object Identifier: <https://doi.org/10.13023/ETD.2016.505>

[Right click to open a feedback form in a new tab to let us know how this document benefits you.](#)

Recommended Citation

Yang, Lin, "THREE-DIMENSIONAL MICROSTRUCTURE-BASED MODELS FOR FATIGUE CRACK NUCLEATION AND FATIGUE CRACK BRANCHING IN HIGH STRENGTH AL ALLOYS" (2016). *Theses and Dissertations--Chemical and Materials Engineering*. 69.

https://uknowledge.uky.edu/cme_etds/69

This Doctoral Dissertation is brought to you for free and open access by the Chemical and Materials Engineering at UKnowledge. It has been accepted for inclusion in Theses and Dissertations--Chemical and Materials Engineering by an authorized administrator of UKnowledge. For more information, please contact UKnowledge@lsv.uky.edu.

STUDENT AGREEMENT:

I represent that my thesis or dissertation and abstract are my original work. Proper attribution has been given to all outside sources. I understand that I am solely responsible for obtaining any needed copyright permissions. I have obtained needed written permission statement(s) from the owner(s) of each third-party copyrighted matter to be included in my work, allowing electronic distribution (if such use is not permitted by the fair use doctrine) which will be submitted to UKnowledge as Additional File.

I hereby grant to The University of Kentucky and its agents the irrevocable, non-exclusive, and royalty-free license to archive and make accessible my work in whole or in part in all forms of media, now or hereafter known. I agree that the document mentioned above may be made available immediately for worldwide access unless an embargo applies.

I retain all other ownership rights to the copyright of my work. I also retain the right to use in future works (such as articles or books) all or part of my work. I understand that I am free to register the copyright to my work.

REVIEW, APPROVAL AND ACCEPTANCE

The document mentioned above has been reviewed and accepted by the student's advisor, on behalf of the advisory committee, and by the Director of Graduate Studies (DGS), on behalf of the program; we verify that this is the final, approved version of the student's thesis including all changes required by the advisory committee. The undersigned agree to abide by the statements above.

Lin Yang, Student

Dr. Tongguang Zhai, Major Professor

Dr. Thomas D. Dziubla, Director of Graduate Studies

THREE-DIMENSIONAL MICROSTRUCTURE-BASED MODELS FOR FATIGUE CRACK
NUCLEATION AND FATIGUE CRACK BRANCHING IN HIGH STRENGTH AL ALLOYS

DISSERTATION

A dissertation submitted in partial fulfillment of the requirements for the degree of
Doctor of Philosophy in the College of Engineering at the University of Kentucky

By

Lin Yang

Lexington, Kentucky

Director: Dr. Tongguang Zhai, Associate Professor of Materials Engineering

Lexington, Kentucky

2016

Copyright © Lin Yang 2016

ABSTRACT OF DISSERTATION

THREE-DIMENSIONAL MICROSTRUCTURE-BASED MODELS FOR FATIGUE CRACK NUCLEATION AND FATIGUE CRACK BRANCHING IN HIGH STRENGTH AL ALLOYS

This study is concerned with using numerical three-dimensional microstructure-based models to quantify the multi-site fatigue crack initiation behaviors by simulating the effects of pores in a cast aluminum alloy, and to analyze the mechanism of fatigue crack branching in thick aluminum alloy plates. It has been recently recognized the three-dimensional effects of pores on fatigue crack initiation, which provide opportunity to quantitatively identify the fatigue weak-link density and strength distribution in aluminum alloy. The stress and strain fields around a micro-pore in an A713 aluminum alloy (an elasto-plastic media) under cyclic loading were quantified as a function of pore position in depth on surface using a 3-D finite element model. The incubation life for the fatigue crack from a pore in surface could be estimated using a micro-scale Manson-Coffin equation. By matching to the experimentally measured fatigue weak-links, the minimum critical pore size for fatigue crack initiation was determined to be 11 μm in diameter at the cyclic maximum stress of 100% yield strength of the alloy.

A quantitative model which took into account the 3-D effect of a pore on the local stress/strain fields was developed to quantify the fatigue weak-link density and strength distribution in the A713 Al alloy. In the model, a digital pore structure was first constructed using single-sized (15 μm in diameter) and multi-sized pores, respectively, that had a total volume fraction same as that of the pores measured experimentally in the alloy. In the sample surface randomly selected by cross-sectioning the simulated pore structure, the size and position in depth of each pore were known in the surface. The rate of fatigue crack initiation at these pores was found to be a Weibull function of the applied stress, which was consistent with the results experimentally measured in the alloy. The density and strength distribution of fatigue weak-links could then be derived and used to evaluate the fatigue crack initiation properties of the alloy. The simulated fatigue weaklink density and strength distribution in the multi-sized pore model were in a good agreement with the experimental results. The difference in the peak of strength distribution between experimentally measured and simulated results was only $\sim 1.8\%$. It was also found that the average crack incubation life was linearly increased with decrease in the applied cyclic stress. The stochastic behaviors of the multi-site fatigue crack initiation and the reliability of fatigue crack initiation at each applied cyclic stress were quantified in the A713 cast Al alloy. The probability of fatigue crack initiation

was characterized by a two-parameter Weibull function, i.e., with 10,000 cyclic loading, the survival probability for crack initiation was 72% at 110% yield strength, and was 99% at 50% yield strength.

A detailed fractographic and microstructural study, using stereo optical and scanning electron microscopy was accomplished to characterize the behavior and mechanisms of fatigue crack branching in a thick commercial 7050-T7651 aluminum plate in the L-S orientation. The SEM fractographies of the middle tension specimen failed in crack growth experiments showed that the transition of the lead crack from a crystallographic (fatigue fracture) to non-crystallographic mode (overloading fracture) of growth at a ΔK of $\sim 17 \text{ MPa}\sqrt{\text{m}}$ with few non-through thickness branches at the mid-thickness plane. An interior branched crack grew into a through crack at a ΔK greater than $30 \text{ MPa}\sqrt{\text{m}}$. The intergranular fracture was observed in the branched cracks, indicating a relationship between crack branching and over-aging state in the alloy. A 3-D finite element model which took into account the effect of both a non-through and through thickness branched crack at the lead crack was consequently developed to simulate the growth behavior with branching. The simulated results demonstrated that the driving force, ΔK , for the lead crack was reduced significantly due to branching at the crack tip, which was responsible for the reduced crack growth rate of the lead crack as observed experimentally. The driving force for crack growth with branching was increased with increasing the lead crack length, which explained the reason why crack branching occurred relatively easily when the lead crack was long. The precipitate-free-zones along grain boundaries were responsible for crack branching parallel to the rolling (L) direction, since the grain structure was stretched in L direction in the Al alloy plate due to hot rolling.

KEYWORDS: high strength Al alloys, porosities, multi-site fatigue crack nucleation, fatigue weak-link density and strength distribution, fatigue crack branching, finite element modeling.

Lin Yang

12/09/2016

THREE-DIMENSIONAL MICROSTRUCTURE-BASED MODELS FOR FATIGUE CRACK
NUCLEATION AND FATIGUE CRACK BRANCHING IN HIGH STRENGTH AL ALLOYS

By

Lin Yang

Dr. Tongguang Zhai

Director of Dissertation

Dr. T. D. Dziubla

Director of Graduate Studies

12/09/2016

ACKNOWLEDGEMENTS

I am very grateful to my advisor Dr. Tongguang Zhai for all of his academic guidance, scientific thinking training and absolute support. Dr. Zhai shows the true spirit of being a scientist: earnest, diligent, dedicated, persistent, passionate and intelligent, which is what he is trying to let us inherit. This has led me to go through the tough but worthy journey of pursuing a Ph. D degree at the University of Kentucky. I will always remember his spirit as a light in my academic life.

I would like to thank the Department of Chemical and Materials Engineering (CME) at UK, especially my committee members, Dr. Fuqian Yang and Dr. T. John Balk, and Dr. Johnathan Wenk and Dr. John Baker from Mechanical Engineering, for their valued comments and suggestions about my research work. Meanwhile, many thanks for the technical support from Electron Microscope Center (EMC) researchers Dr. Dali Qian and Dr. Nicolas Briot. Besides, thank Prof. Zhiqiang Xu in Yanshan University and J. Raphael for helpful suggestions of finite element modeling.

I also would like to thank my former and current group members, who provided academic training for operating equipment and taught many technical skills to me, who spend the several Ph. D studying years with me, discussing each other's topic, sharing happy or awful feelings, supporting and caring each other all the time. I really appreciate that I can spend a precious time with them. They are Dr. Wei Wen, Dr. Yan Jin, Liang Chen, Pei Cai, Gongwang Zhang and Rami A. Almatani.

I gratefully acknowledge the Graduate School of University of Kentucky and the China Scholarship Council for financial support. Special thanks to the Center for Computational Sciences at the University of Kentucky provided the computation time for use of ABAQUS on the HPC (Trestles) in San Diego Supercomputer Center through XSEDE national resources.

At last, I want to mention my significant other, Sandee Huang, who cherishes my PhD degree of Materials Science and Engineering much more than I do. I am glad that I can fulfill a dream that belongs to both of us. I appreciate the unspoken love from my parents and my little brother.

TABLE OF CONTENTS

ACKNOWLEDGEMENTS	III
TABLE OF CONTENTS	IV
LIST OF TABLES.....	VII
LIST OF FIGURES.....	VIII
CHAPTER 1 INTRODUCTION	1
1.1 BACKGROUND	1
1.2 MECHANISMS FOR FATIGUE DAMAGE	2
1.2.1 <i>Fatigue damage and crack initiation</i>	2
1.2.2 <i>Fatigue crack propagation and crack deflection/branching</i>	3
1.3 EFFECTS OF POROSITY ON FATIGUE CRACK INITIATION.....	4
1.3.1 <i>History of studying porosity effects</i>	4
1.3.2 <i>Previous finite element models for crack initiation from pores</i>	6
1.4 FATIGUE PROPERTIES AND FATIGUE WEAK-LINK DENSITY.....	8
1.5 MICROSTRUCTURAL AND MECHANICAL EFFECTS ON FATIGUE CRACK BRANCHING	9
1.5.1 <i>Microstructural effects</i>	9
1.5.2 <i>Mixed-mode fracture solutions</i>	10
1.5.3 <i>Previous finite element models</i>	12
1.6 MOTIVATION OF THE STUDY	13
CHAPTER 2 EXPERIMENTAL DETAILS	20
2.1 TENSILE TEST AND FATIGUE TEST	20
2.2 MICROSTRUCTURE CHARACTERIZATION	21
2.2.1 <i>Scanning Electron Microscope (SEM)</i>	21
2.2.2 <i>Focused Ion Beam (FIB)</i>	21
2.3 NUMERICAL MODELING SOFTWARE.....	22
CHAPTER 3 QUANTIFICATION OF THE PORE EFFECTS ON FATIGUE CRACK INITIATION IN AN A713 CAST AL ALLOY USING A 3-D FEA METHOD	27
3.1 INTRODUCTION.....	27
3.2 FEA MODELING FOR CRACK INITIATION	28
3.2.1 <i>Experimental observations of the 3-D effects of pores on crack initiation</i>	28
3.2.2 <i>3-D elasto-plastic finite element modeling</i>	28
3.2.3 <i>Methodology for incubation life prediction</i>	30
3.3 RESULTS AND DISCUSSION	31
3.3.1 <i>The stress and strain distributions around a surface pore</i>	31

3.3.2	<i>Effects of pore position on stress/strain concentration</i>	31
3.3.3	<i>Effects of pore position on driving force</i>	32
3.3.4	<i>Effects of pore depth on incubation life</i>	32
3.3.5	<i>Effects of applied stress level</i>	32
3.3.6	<i>Effects of applied strain level</i>	33
3.3.7	<i>The size effect of pores on crack initiation</i>	34
3.3.8	<i>The minimum critical pore size for initiation</i>	35
3.4	CONCLUSIONS	35

CHAPTER 4 A 3-D PORE-SENSITIVE NUMERICAL MODEL FOR QUANTIFICATION OF MULTI-SITE FATIGUE CRACK NUCLEATION BEHAVIOR 55

4.1	INTRODUCTION.....	55
4.2	3-D PORE-SENSITIVE MODEL FOR MULTI-SITE CRACK NUCLEATION	57
4.2.1	<i>3-D digital pore-containing microstructure</i>	57
4.2.2	<i>Framework of the model</i>	57
4.2.3	<i>Experimental verification for the stability of the model</i>	57
4.3	DETERMINATION OF THE FATIGUE CRACK FROM A PORE	58
4.4	THE TECHNIQUE FOR QUANTIFICATION OF FATIGUE WEAK-LINKS DENSITY AND STRENGTH DISTRIBUTION	59
4.5	MULTI-SIZED PORE MODEL.....	59
4.6	PORE POSITION DISTRIBUTION	60
4.7	RESULTS AND DISCUSSION FOR QUANTIFICATION OF FATIGUE WEAK-LINKS AND STRENGTH DISTRIBUTION	61
4.7.1	<i>The crack population vs stress</i>	61
4.7.2	<i>The rate of crack initiation vs. Stress</i>	61
4.7.3	<i>Effects of number density and pore size on crack population and cracking rate</i>	62
4.7.4	<i>Fatigue weak-link density and strength distribution of fatigue weak-links</i>	62
4.7.5	<i>Validation of simulation by experiments</i>	64
4.8	PREDICTION OF CRACK INCUBATION LIFE.....	65
4.8.1	<i>Distribution of incubation lives in single-sized model</i>	65
4.8.2	<i>Distribution of incubation lives in multi-sized model</i>	66
4.8.3	<i>Percentage of fatigue initiation life</i>	67
4.9	THE FATIGUE RELIABILITY OF CRACK INITIATION	67
4.10	THE FATIGUE RELIABILITY OF FAILURE	69
4.11	CONCLUSIONS	69

CHAPTER 5 QUANTIFICATION OF MICROSTRUCTURAL EFFECTS ON FATIGUE CRACK BRANCHING IN AA 7050 AL THICK PLATES 105

5.1	INTRODUCTION.....	105
-----	-------------------	-----

5.2	EXPERIMENTAL DETAILS	106
5.2.1	<i>Materials</i>	106
5.2.2	<i>Fatigue tests</i>	107
5.2.3	<i>Fractography</i>	107
5.3	SIMULATION FOR CRACK BRANCHING IN A 3-D FEA MODEL.....	107
5.3.1	<i>Methodology for calculating the driving force</i>	107
5.3.2	<i>3-D elasto-plastic finite element modeling</i>	108
5.4	EXPERIMENTAL RESULTS	109
5.4.1	<i>Growth rates by experiments</i>	109
5.4.2	<i>Microstructure of 7050-T7651 alloy</i>	110
5.4.3	<i>Fatigue crack growth, branching and fracture</i>	110
5.5	SIMULATION RESULTS FOR CRACK BRANCHING	113
5.5.1	<i>Determination of the depth of non-through branches for FEA model</i>	113
5.5.2	<i>Effects of the depth of branch on driving force</i>	114
5.5.3	<i>Validation of the simulated fatigue crack growth rate by experiments</i>	115
5.6	CONCLUSIONS	116
	CHAPTER 6 CONCLUSIONS	139
6.1	CONCLUDING REMARKS	139
6.2	SUGGESTIONS FOR FUTURE WORK.....	141
	REFERENCES	143
	VITA	149

LIST OF TABLES

Table 3.1 Composition (wt. %) and mechanical properties of A713 cast aluminum alloy	37
Table 3.2 Parameters used in Eq. 3.2 for different applied stresses	37
Table 3.3 Parameters used in Eq. 3.2 for different applied strains	37
Table 4.1 The porosities used in the single-sized model	71
Table 4.2 The porosities used in the multi-sized model	71
Table 4.3 Parameters used in Eq. 4.4.....	71
Table 4.4 Two-parameter Weibull analysis on the fatigue incubation life in the single-sized pore model	72
Table 4.5 Two-parameter Weibull analysis on the fatigue incubation life in the multi-sized pore model	72
Table 4.6 Two-parameter Weibull analysis results on the fatigue total life in the multi-sized pore model	72
Table 5.1 Chemical compositions of 7050-T7651 aluminum alloy. (wt. %)	116
Table 5.2 Mechanical properties of 7050-T7651 aluminum alloy.	117

LIST OF FIGURES

Figure 1.1 Sketch diagram showing the geometry of slip at the materials surface according to Forsyth [24].	15
Figure 1.2 Schematic illustration of the different regimes of stable fatigue crack propagation.	15
Figure 1.3 Macroscopic crack deflection in thick AA7050 plate for L-S orientation smooth specimen fatigue tests.	16
Figure 1.4 Fracture surface after failure crack growth from a pore with an initial size of a_i .	16
Figure 1.5 Crack initiation sites near to and at the surface in nickel-based superalloys.	17
Figure 1.6 (a) Single fatigue crack initiation at a low stress level of $70\%\sigma_y$; and (b) multiple crack nucleation at a higher stress level, the maximum cyclic stress of $100\%\sigma_y$, in L-S samples in AA7075-T7651 Al alloy [37].	17
Figure 1.7 Finite element analysis results showing the pore size and location effect on the stress concentration factors, from left to right, (a) 4.4, 3.4, and 2.4 respectively, from largest pore to smallest pore; and (b) 3.9, 3.1 and 3.0, respectively, from closest pore to farthest pore to the free surface.	18
Figure 1.8 Schematic demonstrating the determination of the driving force for fatigue crack nucleation by averaging the maximum plastic shear strain in a surface domain.	19
Figure 2.1 The geometry of the dog bone shaped tensile test specimen of A713 cast aluminum alloys and AA7050 aluminum alloys.	24
Figure 2.2 The Instron 8800 servo-hydraulic test machine used for the tensile testing.	24
Figure 2.3 The actual four-point bend fatigue test rig during fatigue testing.	25
Figure 2.4 The drawing of loading condition and position of supporting and loading rollers on four-point bend samples.	25
Figure 2.5 Schematic diagram of the LMIS and lens system of an FIB.	26
Figure 2.6 Main interaction of Ga^+ with sample material in an FIB.	26
Figure 3.1 (a) SEM micrograph of a typical fracture surface where the crack initiating pore is just buried below the surface in the A713 cast Al alloy [41]; (b) multiple fatigue crack initiation at pores	

on the sample surface [126]; (c)(d) optical micrographs showing fatigue cracks initiated from locations rather than one of the large pores in surface [41]. 38

Figure 3.2 (a) Optical micrograph of a long fatigue crack initiated from a narrow irregular-shaped pore (~11.5 μm in length) on the free surface in the A713 cast Al alloy, and lines b, c, d and e are the locations of the micro cross-sections by FIB in (b)-(e), respectively; (b)-(e) SEM micrographs of the cross-sections showing the shapes of the pore in depth, from 2 μm to 10.5 μm 39

Figure 3.3 The constitutive behavior and applied stress curve for the FEA modeling (a) tensile stress-strain curve measured in a cast 713 Al-Zn alloy, (b) the sinusoidal wave of applied cyclic stress (100% σ_y) curve (at R = 0.1) shows cyclically stable behavior after the first load cycle. 40

Figure 3.4 The hysteresis loops of stress-strain curve of the first 5 cycles from FEA simulation results, from the region surrounding the micro pore when the applied maximum cyclic stress is 50% σ_y . The hysteresis loop is saturated to a steady state quickly after only 3 cycles..... 41

Figure 3.5 FEA Modeling: (a) a symmetrical quarter model with a half of surface pore, and global mesh, (b) typical pore locations in depth in surface. 42

Figure 3.6 Calculation of the average value of maximum shear strain range, γ_{max}^{p*} : (a) the contours of maximum plastic shear strain, γ_{max}^p , (for shear stress/strain: “+” means clockwise, “-” means anti-clockwise. Dark blue is the maximum absolute value in this result); (b) area *MNL* used to calculate the average value of γ_{max}^{p*} on the critical plane. 43

Figure 3.7 The stress/strain fields calculated using an FEA method around a spherical pore at a maximum cyclic stress of 70% σ_y and D/r=0. (a) The contours of Mises stress around the pore and the maximum value marked by an arrow, the stress in 10^4 MPa; (b) The contours of maximum shear strain around the pore and the maximum value (dark blue) marked by an arrow (“+” and “-“ shear stress/strains associated with strains in clockwise and anti-clockwise directions, respectively)..... 44

Figure 3.8 The effects of pore depth on stress/strain concentration (K_t), K_t vs. pore depth. 45

Figure 3.9 The effects of pore depth maximum shear strain amplitude ($\Delta\gamma_{max}^{p*}$), $\Delta\gamma_{max}^{p*}$ vs. pore depth. 46

Figure 3.10 The effects of pore depth on crack incubation life (N_{inc}), N_{inc} vs. pore depth. 47

Figure 3.11 The effects of pore depth on stress/strain concentration (K_t), maximum shear strain amplitude ($\Delta\gamma_{max}^{p*}$) and crack incubation life (N_{inc}) at different applied stress, 70% σ_y and 100% σ_y : (a) K_t vs. pore depth; (b) $\Delta\gamma_{max}^{p*}$ vs. pore depth; and (c) N_{inc} vs. pore depth.	49
Figure 3.12 Applied cyclic strain of 0.2%, 0.4% and 0.6%.....	50
Figure 3.13 The effect of pore position on effective concentration factor K_t at applied strain of 0.2%, 0.4% and 0.6%.....	50
Figure 3.14 The effect of pore position on driving force and incubation life, at applied strain of 0.2%, 0.4% and 0.6%, (a) $\Delta\gamma_{max}^{p*}$ vs. pore depth at 0.2% applied strain; (b) $\Delta\gamma_{max}^{p*}$ vs. pore depth at 0.4% applied strain; (c) $\Delta\gamma_{max}^{p*}$ vs. pore depth at 0.6% applied strain; (d) N_{inc} vs. pore depth at 0.2% applied strain. (e) N_{inc} vs. pore depth at 0.4% applied strain. (f) N_{inc} vs. pore depth at 0.6% applied strain. ...	51
Figure 3.15 Schematic diagram showing the areas ($MN'L'$ and $MN''L''$) used to average the strain shear strain amplitude on the critical plane at a small and a large pore, respectively.	52
Figure 3.16 (a) The effects of pore size on $\Delta\gamma_{max}^{p*}$, the driving force for fatigue crack nucleated from the pore; (b) the effects of pore size on crack incubation life. $D/r = 1$, applied stress=100% σ_y	53
Figure 3.17 The determination of the minimum critical pore size for fatigue crack nucleation.	54
Figure 4.1 Experimentally measured pore size distribution in A713 cast Al alloys.....	73
Figure 4.2 A 3-D pore-sensitive model. (a) the schematic of the reconstructed 3-D digital pore structure by randomly distributing spherical pores in a cube; (b) a simulated sample surface by randomly cross-sectioning the digit pore structure.....	74
Figure 4.3 Verification of the statistical stability of the model by calculating the average area fraction of the pores on the simulated surface as a function of sampling number.	75
Figure 4.4 The porosity morphology in A713 cast Al alloys with (a) low pore density and (b) high pore density [55].	76
Figure 4.5 The range in pore depth between A and B used to determine crack incubation at pores in surface under the maximum cyclic stress of 100% σ_y	76
Figure 4.6 The probability for pore position distribution with number density and pore size in single-sized pore model and multi-sized pore model.	77

Figure 4.7 The crack density vs applied stress in single-sized pore model and multi-sized pore model.	78
Figure 4.8 The rate of crack initiation vs applied stress in single-sized, 2-sized and 3-sized models.	79
Figure 4.9 The effects of number density on the crack density.	80
Figure 4.10 The effects of number density on the rate of crack initiation in single-sized pore model, (a) 15 μm pore; (b) 50 μm pore.	81
Figure 4.11 The effects of pore size on crack density.	82
Figure 4.12 The effects of pore size on the rate of crack initiation.	83
Figure 4.13 Simulated rates of fatigue crack initiation at pores in single-sized and multi-sized pore model, respectively, with a pore area fraction of 2.826%, at different maximum cyclic stresses.	84
Figure 4.14 Plots of $\ln(-\ln(1 - R/R_0))$ vs $\ln(\sigma/\sigma_0 - 1)$ of simulated fatigue weaklinks at pores in single-sized and multi-sized pore model.	85
Figure 4.15 Simulated strength distributions of the fatigue weaklinks in single-sized and multi-sized pore model.	86
Figure 4.16 Simulated rates of fatigue crack initiation at pores with an area fraction of 2.826%, in single-sized and multi-sized pore model, respectively, as compared to the experimental result with a pore area fraction of 2.826%, at different maximum cyclic stresses in the A713 Al alloy.	87
Figure 4.17 Plots of $\ln(-\ln(1 - R/R_0))$ vs $\ln(\sigma/\sigma_0 - 1)$ of experimental in the A713 Al alloy and simulated fatigue weaklinks in single-sized and multi-sized pore model.	88
Figure 4.18 Experimental and simulated strength distributions of the fatigue weaklinks in the A713 Al alloy.	89
Figure 4.19 The prediction of fatigue crack incubation life distribution at pores in the single-sized pore model in the A713 Al alloy at each given applied maximum stress, the number of cracks vs the incubation life.	90
Figure 4.20 Simulated incubation life in the single-sized model, (a) comparison of stress vs. the total life to failure in experiments and the stress vs. the incubation life spectrum in simulations; (b) the minimum value, mean value and maximum value of incubation life distribution at different stresses; (c) the percentage of crack incubation life of the total life to failure vs. stress.	91

Figure 4.21 The prediction of fatigue crack incubation life distribution at pores in the multi-sized pore model in the A713 Al alloy at each given applied maximum stress, the number of cracks vs the incubation life.	92
Figure 4.22 The simulated incubation life in the multi-sized pore model, (a) comparison of stress vs. the total life to failure in experiments and the stress vs. the incubation life spectrum in simulations; (b) the minimum value, mean value and maximum value of incubation life distribution at different stresses.	93
Figure 4.23 The percentage of crack incubation life of the total life to failure vs. stresses in the multi-sized pore model.	94
Figure 4.24 The cumulative probabilities for fatigue crack initiation life distribution at different maximum applied cyclic loading in the single-sized pore model.	95
Figure 4.25 The cumulative probabilities for fatigue crack initiation life distribution at different maximum applied cyclic loading in the multi-sized pore model.	96
Figure 4.26 The linear plots of $\ln\{\ln[1/(1 - P)]\}$ vs. $\ln N$ by a two-parameter Weibull analysis in the single-sized pore model.	97
Figure 4.27 The linear plots of $\ln\{\ln[1/(1 - P)]\}$ vs. $\ln N$ by a two-parameter Weibull analysis in the multi-sized pore model.	98
Figure 4.28 The probability of crack initiation at different applied maximum cyclic stresses in the single-sized pore model.	99
Figure 4.29 The probability of crack initiation at different applied maximum cyclic stresses in the multi-sized pore model.	100
Figure 4.30 The mean value of the simulated incubation life and the experimentally measured failure life at different applied maximum cyclic stresses in the multi-sized pore model.	101
Figure 4.31 The cumulative probabilities for fatigue total life distribution at different maximum applied cyclic loading in the multi-sized pore model.	102
Figure 4.32 The linear plots of $\ln\{\ln[1/(1 - P)]\}$ vs. $\ln N$ by a two-parameter Weibull analysis in the multi-sized pore model.	103

Figure 4.33 The probability of fatigue failure at different applied maximum cyclic stresses in multi-sized model.	104
Figure 5.1 Experimental measured stress-strain curve.	118
Figure 5.2 Pancake-shaped grain structure of 7050-T7651 in L-S plate measured by EBSD.	119
Figure 5.3 Machined specimen configuration.	119
Figure 5.4 The fractured middle tension specimen of 7050-T7651.	120
Figure 5.5 Morphology of the fracture surface of the 7050-T7651 middle tension specimen.	120
Figure 5.6 Schematic graphs for a new method to calculate the driving force with the configuration of a center crack and a branch using FEM.	121
Figure 5.7 Model geometry of the plate with a center crack and a branch. (a) the model geometry without branch, (b) the geometry of non-through thickness branch, (c) the geometry of through thickness branch.	122
Figure 5.8 Crack growth data of 7050-T7651 aluminum alloy L-S specimen, (a) da/dN vs. ΔK , (b) da/dN vs. the length of lead crack.	123
Figure 5.9 The microstructural features of 7050-T7651 alloy by STEM: (a) the precipitate free zone (PFZ) along small angle grain boundary, (b) precipitates in the grain interior, grain boundary precipitates and grain boundary. (c) large grain boundary precipitates within PFZ and the PFZ width is marked by arrow.	124
Figure 5.10 Fractographs of the middle-tension specimen with (a) crystallographic growth during the early stage of the lead crack, (b) the fatigue striations.	125
Figure 5.11 Fractographs of the middle-tension specimen during the second stage of lead crack growth (a) ductile fracture, (b) dimples containing the second phase particles.	125
Figure 5.12 Fractographs of lead crack with branched cracks, (a) intergranular fracture during the early stage of crack growth as branches along GBs (white arrow pointed), (b) high magnification of one of branch in (a) showing GB dimples, (c) intergranular fracture during the second stage of crack growth as the first through-thickness branch along GB, (d) the second through-thickness branch.	126
Figure 5.13 Fractography of final ligament fracture where crack deviation occurred, (a) grain boundary ductile intergranular fracture, (b) dimples on the grain boundary.	127

Figure 5.14 Morphology of fracture surface, (a) micrograph by stereo-optical microscope, (b) micrograph of the transition of the lead crack growth from crystallographic fracture (fatigue failure) to non-crystallographic fracture (overloading failure) by SEM.	128
Figure 5.15 Micrographs of dark regions where many branches (white arrow pointed) gathered, (a) Morphology of fracture surface, (b) SEM of a small dark region (as rectangle in (a)), regarded as the beginning of the second stage of the lead crack growth, (c) high magnification of (b), (d) schematic representation of three ways of the lead crack re-propagation, (e) SEM of large dark region next to the one in (b), located as the elliptical shape of (a).	130
Figure 5.16 Interaction of the two individual branches.	131
Figure 5.17 Growth behavior of branched crack.	132
Figure 5.18 The stress and elastic strain energy fields changing along the thickness of fracture surface of the plate at lead crack front, (a) stress component along the loading direction, σ_{yy} , (b) energy density.	134
Figure 5.19 The effect of the depth of branch and the lead crack length on the driving force for fatigue crack propagation, ΔK , (a) ΔK vs. lead crack length, (b) branch depth vs. lead crack length, (c) ΔK vs. branch depth.	137
Figure 5.20 The comparison of the fatigue crack growth rate from the experiments and the predicted path with finite element simulations.	138

Chapter 1 Introduction

1.1 Background

The majority of failures of metallic structures and components can be attributed to a common engineering and material problem: fatigue [1]. During 1837-1854, many serious railway accidents happened due to fatigue, which led to extensive and systematic investigations of fatigue failure of steels [2-6]. Wohler characterized the fatigue behavior by stress amplitude-life (S-N) curves, based on a variety of fatigue tests [5]. H. Gerber developed the methods for fatigue life calculations for different mean levels of cyclic stresses [7]. People found that the underlying microstructure crystallization weakened the materials until eventual failure by fatigue [8] and the slip bands developed during fatigue deformation and led to the fatigue crack formation under cyclic loading through optical examinations [9]. Basquin showed a linear relationship between the stress and the number of fatigue cycles of metals by a log-log plot (the S-N curve) [10]. Coffin-Manson equation was proposed for the relationship between the number of load reversals to fatigue failure and the plastic strain amplitude, which widely used for strain-based fatigue or low-cycle fatigue [11, 12]. Low-cycle fatigue (LCF) demonstrates that the material sustains considerable plastic deformation under a cyclic load that typical is higher than the yield strength, which can induce permanent fatigue damage in every single load cycle to make fatigue life greatly low.

Meanwhile, the quantitative models for fatigue failure have been developed from the stress analyses of Inglis [13] and the energy theory of Griffith [14]. With linear elastic fracture mechanics (LEFM), the fatigue crack growth was characterized by Paris' law that related the increment of fatigue crack growth per stress cycle, da/dN , to the range of the stress intensity factor, ΔK [15], under constant cyclic loading.

In the past several decades, a thorough understanding of cyclic deformation mechanisms in metals and commercial alloys has clearly been established with the invention of electron microscopes. It has been recognized that the microscopic flaws along persistent slip bands (PSBs) were the crack initiation sites of fatigue failure. Initiation of the fatigue crack is the first stage of the total fatigue life, consisting of over 90% of the total fatigue life when the material is subjected to a low-amplitude cyclic stress/strain (so-called high-cycle fatigue (HCF)).

Aluminum alloys are extensively used in engineering applications, including automobile engine blocks and wheels, fan hubs and airframes etc., due to their excellent weight-to-strength ratio, ability for shape forming, reasonable damage tolerance and corrosion resistance. All the components of aluminum alloys are usually in a service condition of dynamic loading, particularly, in high cycle

fatigue condition. Therefore, the quantitative analysis of fatigue crack initiation behaviors for aluminum alloys is desirable and significant for academic interests and industrial needs. Besides, with increasing demand for thick plate (≥ 5 in) of high strength aluminum alloys in aircraft structural applications, the fatigue crack growth with branching (delamination) becomes an eye-catching problem and its mechanism is urgently needed to be revealed. The current study is mainly focused on the fatigue crack initiation behaviors at porosities in cast aluminum alloys and the fatigue crack growth with branching in 7000 series high strength aluminum alloys using 3-D microstructure-based models.

In this chapter, the relevant introductory information pertaining to fatigue crack initiation and fatigue crack growth with branching in alloys will be addressed. It includes a brief review of mechanisms of fatigue crack initiation and crack propagation with branching, an overview for studying the effects of porosity, a summary for fatigue properties and fatigue weak-links, an overview of the effects of microstructural and mechanical factors on crack branching. The motivation of this study will be presented in the final section.

1.2 Mechanisms for Fatigue Damage

1.2.1 Fatigue damage and crack initiation

Fatigue damage can accumulate from localized plastic deformation under dynamic loading at a relative low stress level in a material. Fatigue crack initiation and crack growth essentially were resulted from the plastic deformation due to the local dislocation activities by cyclic slip under cyclic loading. Under cyclic loading, plastic deformation preferably occurs first on the surface of the material because of the less constraint on plasticity by missing neighboring grains on one side [16, 17]. The cyclic plastic strain is concentrated along the persistent slip bands (PSBs) with intrusions and extrusions (as shown in Figure 1.1). Cyclic slip occurs in a favorable surface grain depending on the size, shape, crystallographic orientation of the grain. A slip step (intrusion) which in fact is an invisible microcrack can be created by a single cycle, followed by crack extension to a small length in the subsequent cycles in a microscopic scale.

Intrusions and extrusions were observed during fatigue process by Forsyth [18, 19]. He reported that thin ribbons of the metal ($0.1 \mu\text{m}$ thick and $10 \mu\text{m}$ long) ‘extruded’ on the surface of PSBs to act a microcrack initiation site in Al-Cu alloy. Cheng and Laird revealed that the fatigue microcrack preferably initiated at PSBs with the highest slip offset and strain localization [20]. The slip movement in PSBs and a certain irreversibility of plastic deformation were observed in experiments [21, 22]. In 1976, Antonopoulos et al. described the dislocation dipoles of vacancy type were

significant for the formation of fatigue cracks [22, 23]. Tanaka and Mura proposed a dislocation dipole model by considering two adjacent layers (PSBs) of dislocation pile-ups with opposite signs to explain the ‘ratcheting’ of plastic deformation [24].

The microstructural heterogeneities, including second phase particles, inclusions and porosities, were found easily to be favorable crack initiation sites due to stress concentration caused plastic strain accumulation around them in materials [25], especially, in high strength alloys [26-30]. Grosskrentz, Laird and Duquette found that the possible sites of crack initiation varied with the applied stresses and microstructures of materials [31, 32]. It has been reported that fatigue crack nucleation occurs preferably from Fe-bearing particles in high strength aluminum alloys, e.g. 2000 and 7000 series aluminum alloys [33-37]. For cast aluminum alloys, casting defects, e.g. porosities, particles and inclusions, were highly prone to form fatigue cracks, in particularly, porosities were the most detrimental defects for fatigue properties [30, 38-42].

1.2.2 Fatigue crack propagation and crack deflection/branching

Fatigue crack is initiated first from a PSB or inhomogeneity with crystallographic fracture mode in the early stage of the crack growth (stage I/regime A, Figure 1.2) in a single grain [43]. The crack growth rate can decrease when the crack tip approaches the grain boundaries that are barriers to slip. More than one slip system may be activated since it will become increasingly difficult to accommodate the constraint on slip displacements when the crack is growing into neighboring grains [16]. All the slips are along most favorably oriented slip planes. This so-called near-threshold (ΔK_{th}) growth shows non-continuum mechanisms and is highly sensitive to microstructure [44]. Microcracks subsequently grows and passes through a substantial number of grains to form a short crack. A short crack can be defined as a crack with a length as follows: micro-scale with the order of grain size; the scale of local plasticity; or physical short with 0.5 mm long [45, 46]. A coherent crack front will be formed and can be a continuous line with an approximate semi-elliptical shape once the crack passes sufficient number of grains [16].

When the stress intensity factor range (ΔK) reaches the threshold value (ΔK_{th}), the crack growth enters the long crack growth regime, namely, the stage II (regime B in Figure 1.2) model of crack growth. At this stage, the crack path is approximately perpendicular to the loading direction and less sensitive to the microstructures in the material. The phenomenon of fatigue crack growth in this regime can be described using Paris law [44, 47], see Figure 1.2, from the application of linear elastic fracture mechanics (LEFM), which were confirmed that the fatigue crack growth increment per cycle da/dN is principally a function of the stress intensity factor range ΔK through a power law relationship

$$\frac{da}{dN} = C(\Delta K)^m \quad (1.1)$$

where C and m are scaling constants that varies with material microstructure, environment, temperature and loading condition. ΔK can be calculated by $K_{max} - K_{min}$, which are the maximum and minimum values of the stress intensity factor during a fatigue cycle, respectively. $K_{max} = Y\sigma_{max}\sqrt{\pi a}$ and $K_{min} = Y\sigma_{min}\sqrt{\pi a}$ for a center-cracked plate containing a crack of length $2a$ at a far-field tensile stress, where σ_{max} and σ_{min} are the maximum and minimum nominal stress, respectively, and Y is the geometry factor.

However, fatigue cracks can deflect macroscopically vertically from its nominal mode I path under cyclic and monotonic loading since the existence of microstructural inhomogeneities such as grain boundaries and interfaces, applied amplitude loading in the form of over-loads and crystallographic separation [46]. The mixed-mode fracture solutions and multiaxial fatigue theory are useful for understanding the mechanically induced crack deflection since there is a triaxial stress field around the crack tip, even if the far-field loading is purely mode I. Under cyclic loading conditions, crack closure is caused by the rough fracture surface created by crack deflections upon unloading, which can further reduce the near-tip driving force (ΔK) to an effective driving force (ΔK_{eff}) for fatigue crack growth [17, 48]. An apparent retardation of the fatigue crack growth can be led in materials by some processes, including premature closure of crack faces at far-fields cyclic loads and periodic deflection in the path of the crack because of microstructural impediments to fracture or varies in local stress state and mode mixity, etc. [46].

In high strength aluminum alloys for use in aerospace applications, e.g. Al-Li alloys and 7050 Al alloys, crack branching (also called ‘delamination’) is an intergranular form of secondary cracking along highly elongated grain boundaries as shown in Figure 1.3 [49, 50]. These high anisotropic alloys are usually thicker than 5 in. and typically produced in plate form after rolling. Their grain structure is “pancake” or lamellar type.

1.3 Effects of Porosity on Fatigue Crack Initiation

1.3.1 History of studying porosity effects

Couper et.al observed that fatigue failure initiated at casting pores, though classical crack initiation from PSBs was also seen but less severe than from pores and never caused failure in casting aluminum alloys [30]. The most significant observation was that almost all pores were found close to or at the sample surface were obviously the site of crack initiation (Figure 1.4). It also showed that the fatigue life can be quantitatively predicted from the size of casting defects and claimed that

reducing the flow size can increase the life until the initiation from PSBs became possible [30], when the pore size was below $\sim 15 \mu\text{m}$.

Wang and Apelian [42] reported that the aluminum alloys containing cast defects could lower their fatigue lives by more than one order of magnitude than their defect-free counter-parts, and that gas porosities were the most detrimental ones to fatigue properties among all the possible cast defects. They measured the pore size on the fracture surface to determine the influence of pore size on the fatigue life of A356 cast aluminum alloys and found that reducing pore size was always beneficial to fatigue life. For A356, the critical pore size was $\sim 25 \mu\text{m}$. Ammar et al. [38] also demonstrated that the fatigue damage was predominantly originated from porosities in their tested samples; 92% of all tested specimens fractured due to surface porosity being a crack initiation site. It can be seen that the pore associated with the crack initiation site always located close to or at the sample surface, which was consistent with Couper's observations. Therefore, fatigue crack initiation occurs preferably at those pores that are just buried below the surface [25, 30, 38, 40, 41, 51, 52], mainly due to the severe stress/strain concentration at these pores.

Generally, the fatigue life increases as the size of the pores is reduced [30, 38, 42, 51], since coarser pores close to the surface present higher stress concentration [40]. It was concluded that only those pores large and near to surface were found to be responsible to crack initiation in cast aluminum alloys [40]. However, some previous experimental results showed that fatigue cracks were not necessarily initiated from the larger pores on the surface [41]. Smaller pores, e.g., around $10 \mu\text{m}$ in diameter, on the surface or below surface could still cause crack initiation [41], even leading to final failure. For example, a pore with $15 \mu\text{m}$ wide and $30 \mu\text{m}$ long in cast aluminum alloy caused final failure in Figure 1.4 [30]; a pore with $10 \mu\text{m}$ in diameter at the surface or below surface led to crack initiation or final failure in nickel-based superalloys in Figure 1.5 [25].

Multi-site crack nucleation often occurs predominantly at pores in cast Al alloys or second phase particles in high strength wrought Al alloys, even though the majority of the fatigue cracks would not propagate later in the fatigue process [36, 37, 41]. Although the larger a pore or particle, the higher the stress concentration it can generate, i.e., the easier crack initiation occurs at the pore/particle, no direct correlation between the size distribution of pores/particles and the fatigue crack nucleation behaviors can be found in cast Al alloys [41] and Al-Cu alloys [53] respectively. An experimental method has recently been developed to characterize the density and strength distribution of crack initiation sites (i.e., fatigue weak-links) in these alloys [37, 41, 54, 55]. The strength of the fatigue weak-links was found to be a Weibull function of the applied cyclic stress. There were more fatigue cracks initiated in higher applied stress levels as shown in Figure 1.6 [37].

There is still a need to understand the mechanism for multi-site crack initiation and quantitatively identify the fatigue weak-links from all the pores in surface, in order to quantify the effects of pores or particles on the fatigue crack initiation behaviors in the Al alloys, especially for high cycle fatigue applications.

1.3.2 Previous finite element models for crack initiation from pores

Several finite element models were conducted for pores in cast aluminum alloys to analyze the effects of pore size, pore position, pore shape and clustering on stress/strain concentration, crack initiation and fatigue life [40, 56-58]. K. Gall et.al quantified the driving force for fatigue crack formation from inclusions and voids in a cast A356 aluminum alloy at monotonic and cyclic loads using finite element methods [56]. The simulated results showed that an awkward shaped star inhomogeneity did not generate maximum plastic shear strain significantly different than the round idealized shape for a void/pore, a cracked inclusion of a deboned inclusion, which means the shape of inclusions, or voids had a relatively small effect on the driving force for fatigue crack formation [56]. This was consistent with the semi-empirical projected \sqrt{area} approach of Murakami et.al [59]. The size of inhomogeneity had significant influence on the driving force for fatigue crack formation since driving forces increased with increasing the size of inclusion or void [56]. In the elastic finite element model of Yi et.al, a large pore close to the surface generated a higher tensile stress as shown in Figure 1.7 [40]. A probabilistic model was also developed to establish a correlation of the casting porosity and the resultant scatter in fatigue life by using a prediction equation of fatigue-crack-propagation life [60] and Monte-Carlo simulation [61] in A356 cast aluminum alloys. Fan et.al conducted 2D cyclic finite element simulations on inclusions and voids (pores) embedded in an elasto-plastic matrix material for A356 aluminum alloys to quantify the influence of the particle and pore size, spacing, aspect ratio and clustering on fatigue crack initiation [58]. They demonstrated that plastic shear strain range increased when the distance between a pore and a free surface decreased [58]. In order to make a full quantitative analysis of crack initiation at pores, three dimensional finite element modeling was recently used to quantify the stress/strain fields around a micro pore (i.e., 30 μm in size) as a function of position in depth from the surface under monotonic loading in A713 cast Al alloys [62]. The stress concentration factor reached peak value when the pore was just buried below the surface.

Fan et.al also developed a method to predict the fatigue crack incubation life at pores for cast aluminum alloys [58] and the details will be described as follows. In 1982, Tanaka and Mura extended their dislocation dipole model to fatigue crack initiations at inclusions and notches [63]. Within PSBs, accumulation of dislocation dipole density enhances the internal tensile stress with

fatigue cycling. In their dipole pile-up model, it becomes energetically favorable to nucleate a microcrack at one slip band when the accumulation of dislocation dipole density and strain energy density within the slip bands reaches a critical value with the load cycle. A microcrack can nucleate within the slip bands by releasing the strain energy stored in the PSB [64]. The critical number of loading cycles could be estimated since the elastic strain energy enhanced by accumulating dislocations should equal to the energy released via the formation of the crack within PSBs. Based on the accumulation of a certain critical amount of fatigue damage, Venkataraman and Mura in 1990 proposed a minimum energy theory for fatigue crack initiation for pointing out that the fatigue crack is preferably nucleated on the free surface [65, 66]. Kato et al. evaluated the net sum of plastic strains γ_p in a slip domain accumulated after n cycles of loading by using applied plastic strain amplitude [67]. In 1991, Mura et al. proposed the generalized Coffin-Manson law for fatigue crack nucleation for associating the cumulative plastic strain with the crack nucleation cycle number [66].

Based on above theory and extensive work, Fan proposed a local form of the Coffin-Manson law to evaluate the incubation of a fatigue crack using the local maximum cyclic plastic shear strain range in Al alloys. In reality, maximum cyclic plastic shear strain range is appropriate to be the driving force for fatigue crack nucleation based on experiments under multiaxial loading conditions [68-71]. So the maximum range of cyclic plastic shear strain $\Delta\gamma_{max}^{p*}$ was regarded as driving force for fatigue crack formation, which was consistent with the minimum energy theory and observations that fatigue cracks frequently initiated from near the free surface [58]. The modified Coffin-Manson law is expressed as Eq. (1.2) and Eq. (1.3)

$$C_{inc} N_{inc}^{\alpha} = \beta \quad (1.2)$$

$$\beta = \Delta\gamma_{max}^{p*} / 2 \quad (1.3)$$

where β is the nonlocal amplitude of maximum plastic shear strain the micro plastic zone around the defects as shown in Eq. [1.3] in aluminum alloys; $\Delta\gamma_{max}^{p*}$ is a local average value of the range of maximum plastic shear strain which can be obtained from the stress/strain curve of the fatigue experiments [72]. α is the Coffin-Manson fatigue ductility exponent which can be identified by experiments [58, 73] $C_{inc} = C_n + z(C_m - C_n)$ where C_m and C_n are low cycle fatigue (LCF) and high cycle fatigue (LCF) strain coefficient at micronotch respectively; z is a variable related to the plastic zone size; Incubation of the fatigue crack N_{inc} is defined as the number of cycles required to nucleate a crack at a pore or particle and then to grow a short distance from the pore or particle when the fatigue damage evolution is under the effect of micronotch root plasticity.

However, in their work, the method used is still 2D in nature as the maximum shear strain amplitude was only averaged over a square area on the free surface when the length of the square equivalent to the quarter diameter of the pore as shown in Figure 1.8. Besides, all the studies only emphasized large pores (100 μm - 200 μm) for crack initiation in cast aluminum alloys, but in A713 cast aluminum alloys, it has been found that fatigue cracks were not necessarily initiated from the coarser pores on the surface by Zhang et al. [41]. According to experimental observations, the crack was initiated from the small pores at surface rather than from larger pores [41]. Therefore, it is still desirable to investigate the size effect of pores on fatigue crack initiation and the minimum critical pore size below which fatigue cracks are not initiated at the pores. Both of them will be studied in this work.

1.4 Fatigue Properties and Fatigue Weak-link Density

The S-N curve approach, so-called ‘total-life’ approach is used for characterization of total fatigue life to failure in terms of the cyclic stress range for classical fatigue design. The number of stress cycles for inducing fatigue failure in smooth-surfaced and initially uncracked specimen is estimated at cyclic stress load, which incorporates the number of cycles to initiate a dominate crack and to propagate this flaw until final failure occurs. In this method, the effects of mean stress, stress concentrations, environments, multiaxial loads and variable stress amplitude on the prediction of total fatigue life can be investigated. However, inevitable large scatter exists in the measured S-N data due to the inherent microstructural inhomogeneities in engineering components.

Another approach so-called ‘defect-tolerant’ based on a basic premise that all engineering components are inherently flawed is used for fatigue design. The pre-existing flaws and cracks are generally examined from nondestructive detection techniques. The initial crack size is estimated if no cracks are detected in a material. Based on the empirical crack growth laws in linear elastic fracture mechanics (LEFM), the fatigue life is defined as the number of cycles or time to propagate the dominate crack from the initial size to some critical dimension related to the fracture toughness of the material. This approach is intrinsically conservative because it only takes the largest flaw into account for prediction of fatigue life, has been widely used in fatigue-critical applications, such as aerospace and nuclear industries.

Weibull proposed a concept of weak-link to describe the scatter of the strength in brittle materials [74]. It was extended to fatigue strength by Freudental through the statistical distribution of the defects in material [75]. Weibull distribution is used to predict the fatigue life [76] and notch size effect in high cycle fatigue [77], to estimate the fatigue variability in cast aluminum alloys [77] and the fatigue strength of metallic structural components [78].

Zhai [54] has recently developed an experimental technique for quantitative characterization of the microstructural inhomogeneities where fatigue crack nucleation occurs in an Al-Li alloy, by measuring the number of fatigue cracks observed on the sample surface at different stress levels. The crack population found on surface appears to be a Weibull function of the applied cyclic stress, which could yield the density and strength distribution of the fatigue weak-links [79]. This method has subsequently been used to study the fatigue crack initiation behaviors and their anisotropy in AA 7075 alloy plates [37] and Al-Zn cast alloys [41]. The Weibull distribution function has previously been used to predict the fatigue limits in Ti alloys [80, 81], and describe the size distribution of surface cracks generated in steel [82]. In Al-Li alloy plates [79] and AA7075 T651 alloy plates [37, 83], the fatigue properties were highly anisotropic, due to the pancake-shaped grain structure and strong texture in these plates, with the poorest being in the S direction and the best in the L direction, as the fatigue weak-links density was highest when loading along the S direction and was lowest along L direction. It was proposed that the strength distribution of fatigue weak-links was more appropriate to be used to evaluate the multi-site fatigue crack nucleation rather than pore size distribution in an A713 cast aluminum alloy [41]. A further study indicated that, using crack nucleation rate instead of crack population on the sample surface to quantify the relation between fatigue weak-links density and the applied stress could minimize the influence of variation in pore density from one sample to another on the crack population measured in the A713 alloy [55]. A three parameter Weibull distribution function was found to be the most appropriate among all the sigmoidal functions to fit the curve of fatigue weak-links density vs. the applied maximum cyclic stress in high strength wrought and cast alloys [83]. These findings have verified that the experimental method is an effective technique to evaluate the quality of an engineering alloy in terms of its fatigue weak-link density and strength.

The level of reliability or probability of fatigue failure can be derived by analyzing the uncertainties in the use of the stress-life approach [84-88]. These uncertainties arise from microstructural variability from following sources: (1) one specimen or batch to another and experimental errors; (2) the variability in stress amplitudes during cyclic loading with vibrations and lack of knowing the exact distribution of the stress range; (3) environments; (4) modeling and predictions for fatigue processes. Weibull [46, 89] proposed the concept of a probability of failure, P , at a given failure strength, in order to addressing the issue that large scatter in fatigue data arise from considerable microstructural variability in materials.

1.5 Microstructural and Mechanical Effects on Fatigue Crack Branching

1.5.1 Microstructural effects

The phenomenon of fatigue crack branching/delamination in precipitation hardened alloys, e.g. Al-Zn-Mg-Cu alloys, were recognized in these days. Early references to the phenomenon of microstructural studies [90-93] associated with grain boundary ductile fracture (GBDF) have been concluded with respect to the three main ideas. They were (1) microvoid growth at large grain boundary precipitates, (2) strain localization in the soft, and sometimes solute-free, grain boundary precipitate free zones (PFZs) and (3) the influence of matrix precipitate shear providing inhomogeneous “planar” slip may lead to large stress concentrations to the grain boundary at the end of slip bands [94]. The published evidence strongly suggests that the first process have an overwhelming important role though the last two ideas have been supported in many cases [93]. Fatigue cracks have been reported to deflect from nominal mode I under monotonic and cyclic loading due to strongly texture and grain boundary failure in aluminum alloy plates. In the L-T and T-L type orientation, the crack deflection was linked to the strongly texture alloys containing a high volume fraction of shearable precipitates [95]. In L-S type orientation, many factors leading to fatigue crack deflection were related to microstructures such as ageing precipitates along grain boundaries, soft grain boundary precipitate free zones (PFZs), matrix precipitate, environmental interactions, impurity segregation [96]. It has been observed that strain concentration during plastic flow occurs within PFZs in Al-Zn-Mg materials [93]. Zhai et al. [97, 98] proposed a three dimensional crystallographic model to describe the grain boundary resistance (R) for varied crack growth rate and crack deflection in Al-Li alloys and Al-Cu alloys. The twist angle and tilt angle between the favored slip plane in a grain for a fatigue crack normally propagation and the favored slip plane in a neighbor grain have been involved into this model. The twist angle represents major resistance for crack propagates from one grain to another. The tilt angle also can reduce the driving force of crack tip. Crack plane will twist or tilt when the crack passes across a grain boundary since the fatigue crack prefers to propagate along the slip plane with the minimum twist angle and relatively small tilt angle whilst the orientation of each grain is varied. The crack twist effect on crack growth rate and crack deflection due to grain boundary resistance has been verified [99, 100]. Recently, an investigation of delamination fracture by electron back-scattered diffraction (EBSD) in Al-Li alloy 2009 which has similar grain structure and fracture mode with Al-Zn-Mg-Cu alloys, demonstrated that the delamination was frequently occurred between variants of the brass texture component [101].

1.5.2 Mixed-mode fracture solutions

The other effects such as overloads and multi-axial stresses were investigated since a fatigue crack deviated from its nominal Mode I plane induces mixed-mode near-tip conditions even if the far-field applied stress is purely Mode I [46]. The mixed-mode fracture mechanics and multiaxial fatigue

theory are useful for explaining crack deflection. The state of stress at the root of a notch (or the root of the crack tip) is triaxial, different from the state of stress in main body. A theory has been proposed that the direction of crack growth in a combined stress field is determined by the critical value of strain energy density factor which represents the strength of the elastic energy field in the vicinity of the crack tip within a core region by Sih [102]. This theory based on an assumption that crack initiation occurs when the interior minimum strain energy density factor reaches the critical value [102]. The result has been reported by Shih that fatigue crack deviation from the nominal mode I growth plane also causes an increase in the size of the plastic zone ahead of the crack tip [103]. Suresh and Shih have published a summery to determine the stress conditions at the tip of a kinked (or forked) crack, deflection angle and the deflected crack length by using available elastic stress intensity factor solutions in 1986. They also discussed that the combined effects of crack tip plasticity and crack branching can promote beneficial crack growth resistance and fracture toughness [104]. Sinclair and Joyce presented a similar study for AA7050-T7651 and Al-Cu-Li alloy plate which indicated that crack paths have been controlled by the combination of crack loading mixity (mode I and mode II)and maximum strain energy released rates [49, 105].

Brown and Miller has proposed a critical plane approach of multiaxial fatigue life evaluation based on a physical interpretation of the mechanisms of fatigue crack growth [106]. Because experimental observations indicate that cracks nucleate and grow on specific planes, which are either maximum shear planes or maximum tensile stress planes. By modifying the critical plane approach, a Fatemi-Socie model has been established which can predict the multiaxial fatigue life and orientation of the crack growth. They developed a shear-based multiaxial fatigue parameter as Eq. (1.4)

$$FP = \frac{\Delta\gamma}{2} (1 + K \frac{\sigma_{nmax}}{S_y}) \quad (1.4)$$

where σ_{nmax} is the maximum normal stress on the critical plane, K is the material constant, S_y is the yield strength and the $\frac{\Delta\gamma}{2}$ is the shear strain amplitude. In the model, the maximum shear strain amplitude and the maximum normal stress acting on the maximum shear strain amplitude plane are the parameters governing fatigue damage [68]. It should be noticed that the Fatemi-Socie model is only suitable for many metals and alloys where the majority of fatigue life is spent in crack nucleation and small crack growth along the maximum shear planes.

For some materials, the critical plane of crack nucleation and growth is along the maximum tensile stress/strain plane. The Smith-Watson-Topper (SWT) parameter can be used in this situation as the fatigue damage model and the governing parameters are the maximum principal strain amplitude

and the maximum normal stress on the maximum principal strain amplitude plane [107]. The SWT parameter can be expressed as,

$$FP = \sigma_{nmax} \frac{\Delta\varepsilon}{2} \quad (1.5)$$

where σ_{nmax} and $\Delta\varepsilon$ are the maximum normal stress and strain range respectively on the maximum normal strain amplitude plane.

The Fatemi-Socie model and the Smith-Watson-Topper parameter criteria are useful for materials exhibiting shear cracking and normal cracking while some materials display mixed cracking behavior. A combined model of shear and normal components has been developed for mix cracking behavior by Jiang, Chu [108, 109]

$$FP = \sigma_{nmax}\Delta\varepsilon + \Omega\Delta\gamma\Delta\tau \quad (1.6)$$

where $\Delta\gamma$ and $\Delta\tau$ are the shear strain range and normal stress range respectively on the critical plane which is defined as the material plane that experiences a maximum FP. Ω is a material constant and varies from 0 to a large value. Glinka et al. discussed a similar parameter in their work. A new criterion which incorporates the critical plane approach in multiaxial fatigue, plastic [110, 111] strain energy and well-documented loading sequence effect has been proposed by Jiang [112].

1.5.3 Previous finite element models

Finite element methods have recently been used for quantitatively analyzing the crack branching in alloys. The process of crack branching can significantly reduce the stress intensity factor (SIF) and the rate of crack propagation by using 2D finite element calculations [113]. In order to predict the path of a branched crack and calculate the associated Models I and II SIF for developing more accurate analytical solutions, a 2-D finite element program named Quebra2D was used [114]. However, the limitation of this numerical method must be pointed out that was the FE calculations assumed linear-elastic conditions while actual branches can cause local plastic deformation, and lack of microstructural features in their model. A bilayer model of a soft (PFZ) and a hard damaging zone (precipitates within grain) has been developed to elucidate the influence of the microstructural parameters on grain boundary intergranular failure in aluminum alloys, and the results showed that the stress triaxial, the void spacing and the PFZ thickness were the main parameters [115]. A numerical strategy was developed to account for fatigue fracture anisotropy for the prediction of crack branching and crack turning in advanced aluminum alloys by implementing a modified mixed-mode fatigue criteria into a 2-D FE shell structure model [116]. A comparison of the predictions with the actual crack paths, showed that the numerical method was only valid for branching angles with

0~45 degrees. In present work, a 3-D finite element method which took into account a branch at the lead crack tip perpendicular to the lead crack was developed for the quantitative analysis of the influences of branching on crack growth behavior, by assuming conditions of elasto-plastic and large displacement.

1.6 Motivation of the study

The recent research work that motivates the present project includes:

- A thorough understanding of the 3D effects of pores on fatigue crack initiation in Al alloys;
- Development of an experimental method to characterize fatigue weak-link density and strength distribution.

As discussed early in this report, fatigue cracks are preferably initiated from pores or particles just buried beneath the surface in alloys, and they are not necessarily nucleated from coarse pores or particles. Therefore, in this work, the effects of position in depth of microscopically scale pores on fatigue crack initiation are being quantitatively studied using three dimensional elasto-plastic finite element modeling. The incubation life of a fatigue crack initiated from a surface pore will be estimated using a modified Manson-Coffin law which assumed that the primary driving force for fatigue crack initiation is the local average maximum plastic shear strain range. In this research, high strength aluminum alloys, such as A713 cast aluminum alloys, will be used for study of fatigue crack initiation. The maximum plastic shear strain used in the Manson-Coffin equation is likely to be along the primary slip plane, close to 45 degree with the load direction, around a pore. A microstructure-based model, namely, a pore-sensitive model that can take an account of the 3D effects of pores on crack initiation could then be developed to quantify fatigue weak-link density and strength distribution in an A713 cast aluminum alloy. The fatigue weak-link densities and strength distributions in this alloy was measured experimentally and was be used to calibrate and verify this theoretical model to be developed in this work. Based on the quantitative pore-sensitive model, probabilistic analysis was used to quantify the stochastic behaviors of the multi-site fatigue crack initiation and the reliability of fatigue crack initiation at each applied cyclic stress by predicting the fatigue crack incubation life in an A713 cast Al alloy.

Because of the increasing demand for use of thicker Al alloy plates (>5 in) in airframe applications, the manufacturers are in a great need to understand the effects of the out-of-plane stress on fatigue crack growth behaviors. For example, it has been recognized that fatigue crack branching could occur from the mode-I path (i.e., the path perpendicular to the load axis) in the rolling plane normal (S direction) to the rolling/loading direction (L direction) in AA7050-T7651 aluminum alloy thick

plates. Quantitative understanding this phenomenon is critical for the optimum design of the airframes where these plates are used. Although attempts have previously been made to quantify the crack deflection/branching using the mixed-mode load fracture theory, the microstructural effects on the crack branching have not been incorporated in the quantitative simulation of the phenomenon. In this work, a detailed fractographic and microstructural study, using stereo optical and scanning electron microscopy has been accomplished to characterize the behavior and mechanisms of fatigue crack growth with branching in thick commercial 7050-T7651 aluminum plate in the L-S orientation. A 3-D finite element model which took into account a non-through/through thickness branch in the lead crack tip was consequently developed to simulate the influence of branching on the crack growth behavior. The experimentally measured growth rate in the alloys was be used to validate this numerical model.

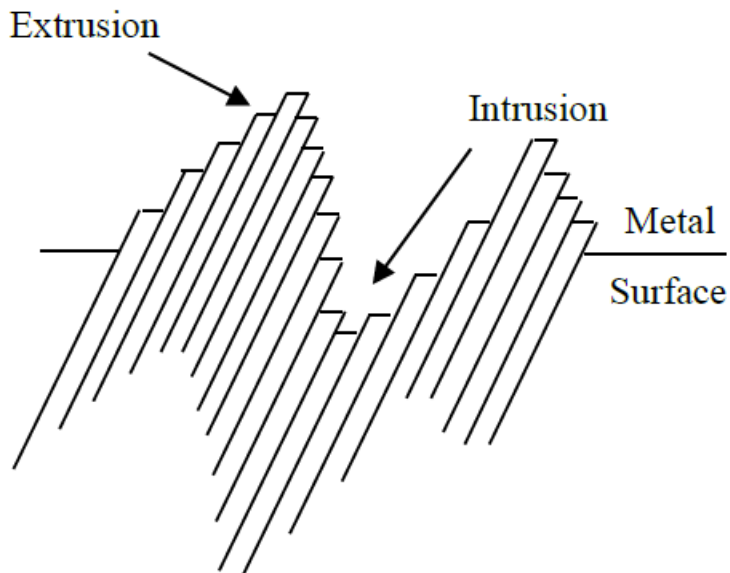


Figure 1.1 Sketch diagram showing the geometry of slip at the materials surface according to Forsyth [24]

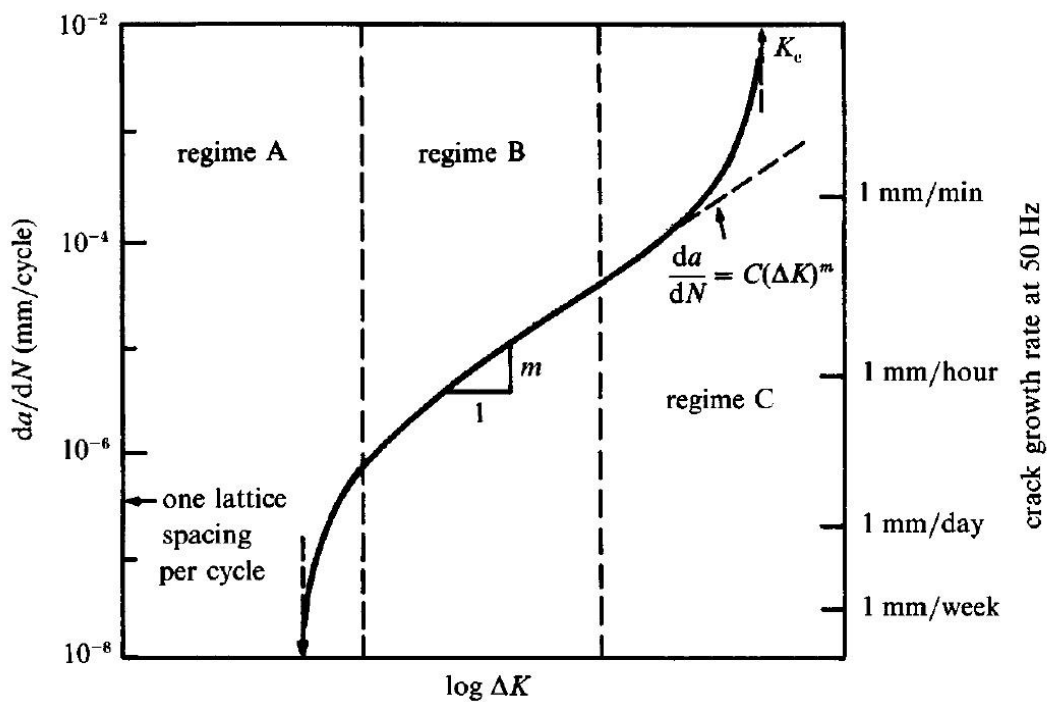


Figure 1.2 Schematic illustration of the different regimes of stable fatigue crack propagation.

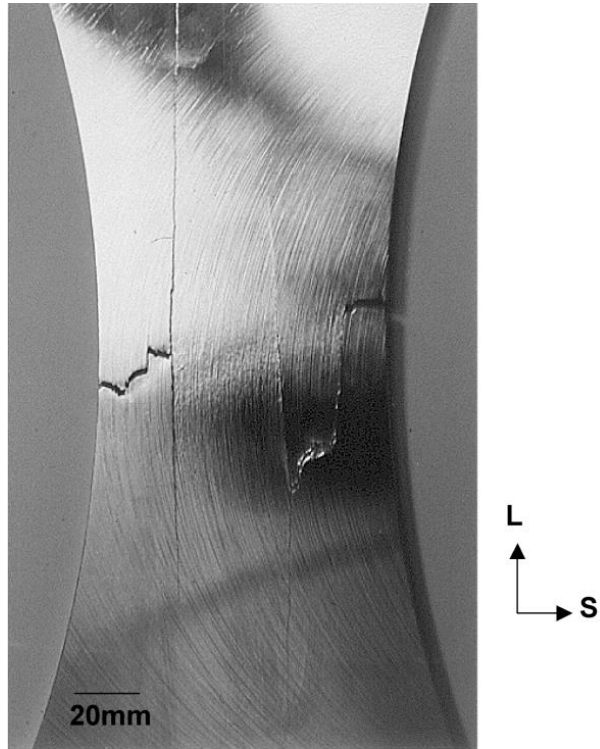


Figure 1.3 Macroscopic crack deflection in thick AA7050 plate for L-S orientation smooth specimen fatigue tests.

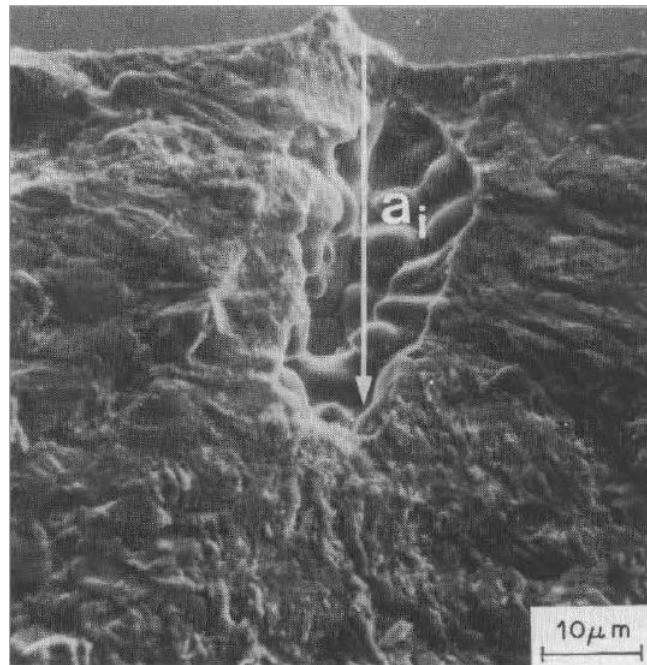


Figure 1.4 Fracture surface after failure crack growth from a pore with an initial size of a_i .

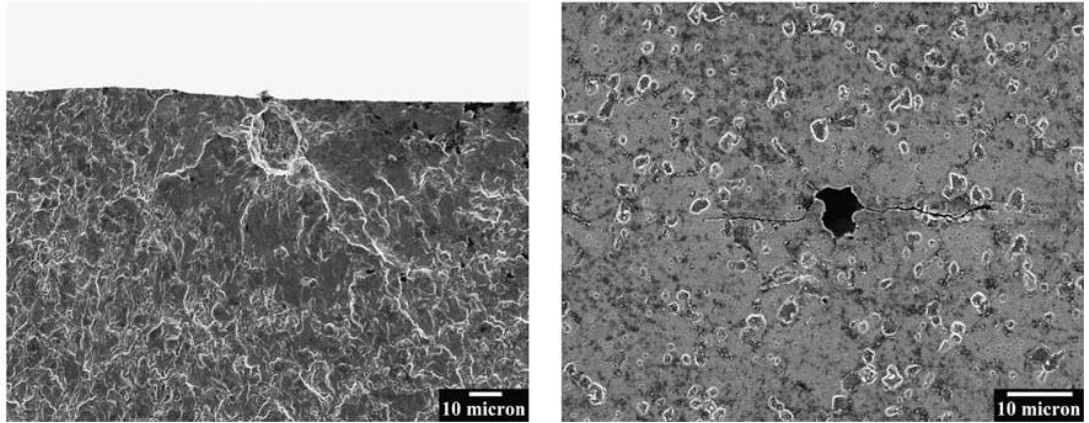


Figure 1.5 Crack initiation sites near to and at the surface in nickel-based superalloys.

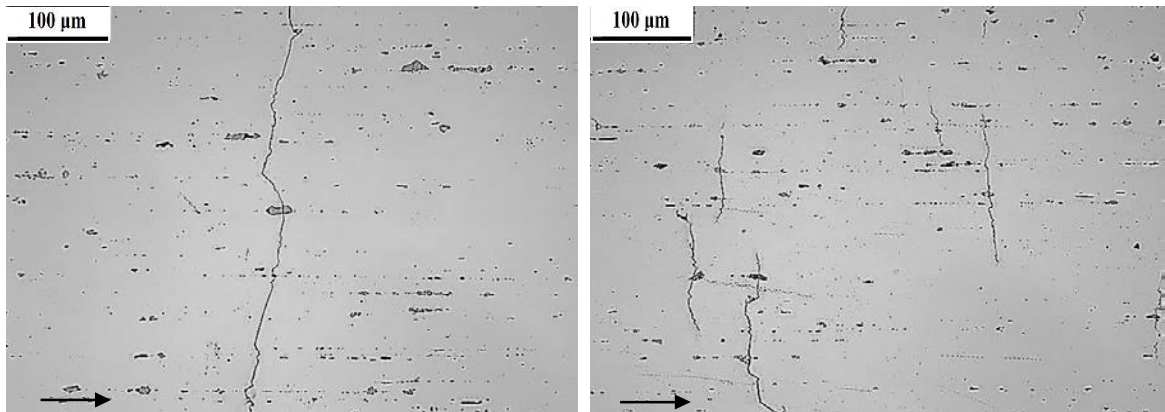


Figure 1.6 (a) Single fatigue crack initiation at a low stress level of $70\%\sigma_y$; and (b) multiple crack nucleation at a higher stress level, the maximum cyclic stress of $100\%\sigma_y$, in L-S samples in AA7075-T7651 Al alloy [37].

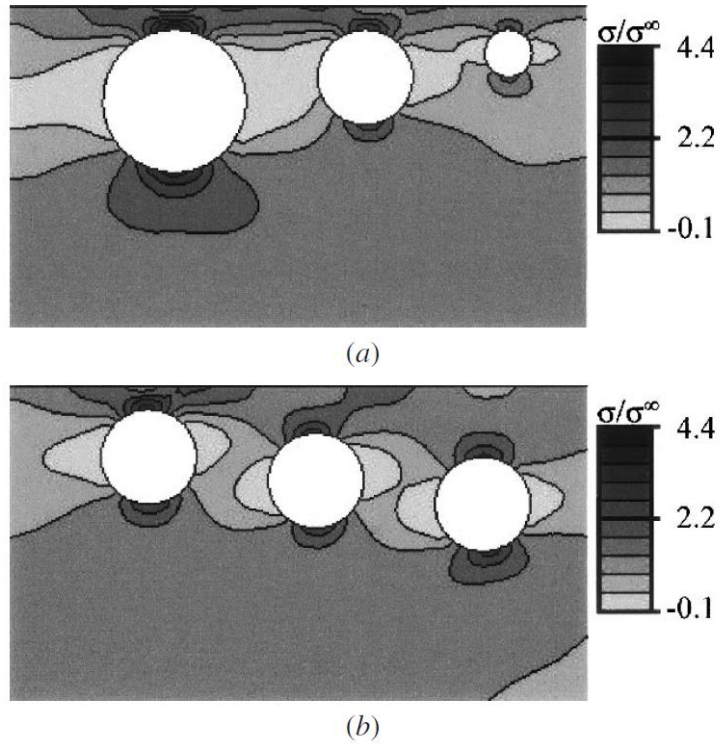
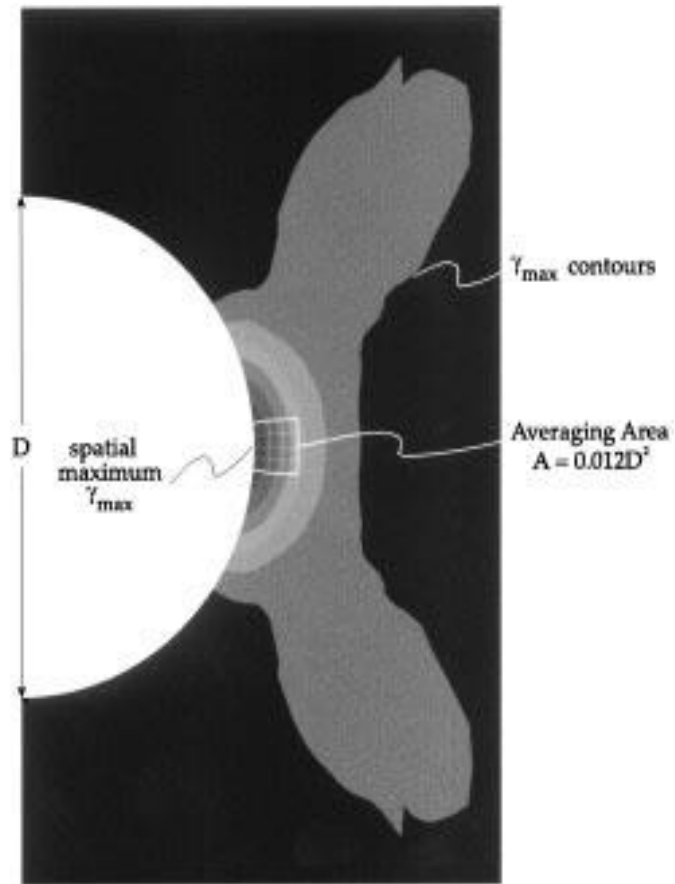


Figure 1.7 Finite element analysis results showing the pore size and location effect on the stress concentration factors, from left to right, (a) 4.4, 3.4, and 2.4 respectively, from largest pore to smallest pore; and (b) 3.9, 3.1 and 3.0, respectively, from closest pore to farthest pore to the free surface.



$$\gamma_{\max}^{\text{ave}} = \frac{1}{A} \int_A \gamma_{\max} dA$$

Figure 1.8 Schematic demonstrating the determination of the driving force for fatigue crack nucleation by averaging the maximum plastic shear strain in a surface domain.

Chapter 2 Experimental Details

In order to study the multi-site fatigue crack nucleation behaviors in A317 cast aluminum alloys and fatigue crack branching behaviors in AA7050-T7651 high strength aluminum thick plates, a series of tests and characterizations were carried out. The traditional tensile test and four-point bend fatigue tests were conducted to measure the mechanical properties and fatigue properties of A713 to investigate the fatigue crack nucleation behavior at porosities by previous researcher in author's research group. The pin-loaded fatigue tests were carried out in AA7050-T7651 aluminum alloys by Alcoa Tech. Center. Combined with optical microscope (OM), stereo optical microscope, scanning electron microscope (SEM), electron backscattered diffraction (EBSD), focused ion beam (FIB), and transmission electron microscope (TEM), the 3-D effects of microstructures on the multiple crack nucleation and the fatigue crack branching were presented. Some experimentally measured results have been used to verify the microstructural-based models for fatigue crack nucleation and fatigue crack branching in A713 and AA7050-T7651 aluminum alloys.

2.1 Tensile Test and Fatigue Test

According to ASTM [117] standard, the dog bone shaped tensile specimens were prepared with a gage length of 25.4 mm and width of 6.35 mm (Figure 2.1). The specimens were cut from a commercial sand cast A713 cast alloy, used for fan hub application, and from a 7050-T7651 plate in the L-S orientation of parent thickness 139.7 mm (5.5 in). Tensile tests were performed on a MTS-810 (A713) and an Instron 8800 (7050-T7651) servo-hydraulic testing machine (Figure 2.2) at room temperature in air, which have been completed earlier by Zhang [41] and Yan Jin, respectively. Tensile properties were taken from the average of two standard testing. The stress levels for the fatigue tests were determined depend on their tensile properties and the yield strength.

Four-point bend fatigue tests were conducted on of a series of A713 cast aluminum alloys using the self-aligning four-point rig (Figure 2.3) [118] at a stress ratio $R=0.1$, frequency of 20 Hz, and room temperature, in a sinusoidal waveform and ambient air. The dimensions and geometry of four-point bend samples as shown in Figure 2.4. According to a finite element analysis, a uniform surface tensile stress in the sample of 4.6 mm thick could be produced using a testing geometry of the loading span of 6 mm and supporting span of 30 mm. The run-out point in the four-point bend fatigue tests set as 5,500,000 cycles, and the tests were stopped automatically when the critical maximum sample deflection was reached, in order to protect the specimen surface for post study of the crack population with optical microscopy. The maximum cyclic stress (relatively to yield strength) used in these tests ranged from the fatigue limit to the ultimate tensile strength. Two samples at each stress level were

tested in the S-N curve measurement, and the crack population found in each sample was measured in optical microscopy.

2.2 Microstructure Characterization

2.2.1 Scanning Electron Microscope (SEM)

Scanning electron microscope (SEM) is a type of electron microscope to produce high-resolution images of a sample surface by using a focused electron beam. A high-energy electron beam is thermionically emitted from an electron gun, collimated by electromagnetic condenser lenses, focused by the objective lens, and scanned across the surface of the sample by electromagnetic deflection coils [119, 120]. When the accelerated incident electrons bombard on the sample surface, several signals can be ejected from specimen atoms, including secondary electrons (SE), backscattered electrons (BSE), diffracted backscattered electrons (signal used to determine crystal structure and orientation by EBSD system), Auger electrons, X-rays, etc. The low energy (<50 eV) SEs that originate within a few nanometers from the sample surface are very sensitive to the surface topography, which are the most common used signals. The electrons are detected by a scintillator-photomultiplier device and the consequent signal is transformed into a 2-D intensity distribution that can be viewed and saved as a digital image. The BSEs are reflected out of the sample interaction volume by the elastic scattering/reflection of the incident electron beam with the atomic nuclei in the sample surface. The heavier atom (with a greater atomic number Z) can produce an elastic collision with the higher probability due to larger cross-sectional area of the nuclei. Therefore, the image in BSE mode are used to perform the different chemical compositions of the scanned surface. In the present work, SE mode was used for the topography observation on SEMs Hitachi S-4300.

2.2.2 Focused Ion Beam (FIB)

The Focused ion beam (FIB) instrument resembles a SEM, but FIB uses a focused ion beam instead of an electron beam in SEM. By adjusting the beam current and accelerating voltage, a FIB can be used to produce high-spatial-resolution images, precisely deposit and micro-machine the sample surface at a micro scale. The most commercially available FIB system is the liquid-metal ion type source (LMIS) [121] and the Ga-based blunt needle sources (Figure 2.5) due to the low melting temperature, low volatility, and low vapor pressure [122]. In a Ga LMIS, Ga is extracted by field emission and flows from a reservoir to an extremely small needle tip. A huge negative potential between the needle and an extraction electrode generates an electric field of magnitude 1010 V/m at the needle tip, which causes ionization and field emission of the Ga atoms. For the typical emission currents used in FIB microscopes (~2 mA), a cusp shaped tip of the Taylor cone is ~5 nm in radius.

Once the Ga⁺ ions are extracted from the ion source, they immediately travel through a series of lens, including condenser lens and an objective lens, as shown in Figure 2.6. When the Ga⁺ ions bombard on the sample surface, the kinetic energy of the ions is transferred to other signals by interacting with the sample atoms. Seeing Figure 2.6, the ion-sample interaction generates ion reflection and backscattering, electron emission, electromagnetic radiation, atomic sputtering, ion emission and sample damage [123, 124]. Among these signals, the ion-induced secondary electrons (ISEs) are collected by the detector in FIB system for imaging. FIB also can be used for ion beam sputtering, allowing precise milling of a material down to a submicron or a nano scale.

When an accelerated Ga⁺ ion impinges the sample surface and sputters a small amount of material, which ejects a sputtered ion or neutral atom. The depth of the effect zone of ion bombardment is determined by the accelerating voltage [123, 125]. Halogen gases, including Cl₂, I₂, and XeF₂ can form a volatile compound with the sputtered material to accelerate the sputtering process.

In this research work, the FIB was used to reveal the 3-D geometry and dimensions of a micro-pore in an A713 cast aluminum alloy surface that caused fatigue crack initiation by cross-sectioning the pore as a fatigue crack nucleation site in a failure sample after fatigue test. A dual-beam SEM/FIB system, FEI Quanta 200-3D, was used to carry out the experiments above by Pei Cai.

2.3 Numerical Modeling Software

The majority of the present research work has been analyzed in numerical calculations and simulations using commercial finite element modeling (FEM) software (ABAQUS) and Matlab software. The microstructural elasto-plastic finite element analysis for cyclic loading conditions can help to clarify the fatigue properties of the microstructure-sensitive materials and to develop a microstructure-based fatigue models for quantitatively understanding the microstructure-property relations and fatigue crack branching behaviors. The programs were developed using Matlab for establishment of a 3-D pore-sensitive model to quantifying the fatigue multi-site nucleation behaviors in aluminum alloys. Both numerical techniques have been used in stochastic modeling for prediction of the reliability of fatigue crack initiation.

The finite element analysis (FEA) originally is a numerical technique for approximating the solutions for solving solid mechanics problems. It has been used for solving engineering problems and mathematical physics. The problems involving complicated geometries, loadings, and material properties are generally not possible to obtain analytical mathematical solutions. Relying on numerical methods, the finite element formulation of the problem results in a system of simultaneous algebraic equations for solutions, rather than differential equations. By dividing a body into an

equivalent system of smaller units interconnected at nodes and boundaries and surfaces is called discretization. In the finite element method, the solution for the entire body can be obtained by formulating the equations for each finite element and then combine them [126] .

In present work, the finite element method has been used to calculate the stress/strain fields in the critical plane for crack formation at a micro pore for A713 cast aluminum alloy and the stress/strain fields around a branch for 7050-T7651 aluminum alloy. More details related to the FE modeling and simulations will be presented in Chapter 3 and Chapter 5.

Matlab provide efficient matrix manipulations for fulfillment of the simulations and calculations for stochastic modeling for prediction of the reliability of the fatigue crack initiation in A713 cast aluminum alloy based on the FEA results. More details will be described in Chapter 4.

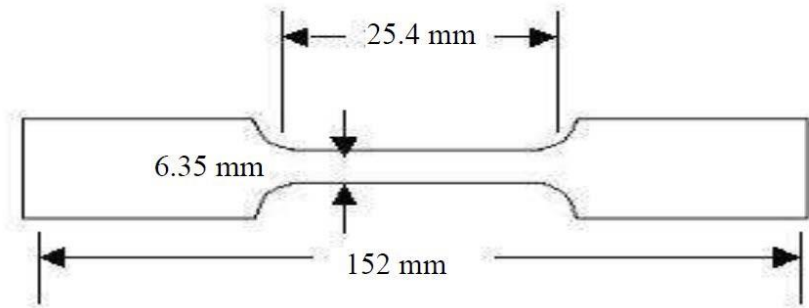


Figure 2.1 The geometry of the dog bone shaped tensile test specimen of A713 cast aluminum alloys and AA7050 aluminum alloys.



Figure 2.2 The Instron 8800 servo-hydraulic test machine used for the tensile testing.



Figure 2.3 The actual four-point bend fatigue test rig during fatigue testing.

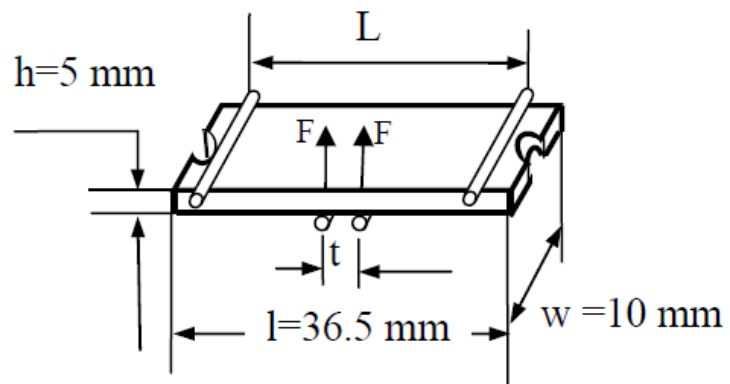


Figure 2.4 The drawing of loading condition and position of supporting and loading rollers on four-point bend samples.

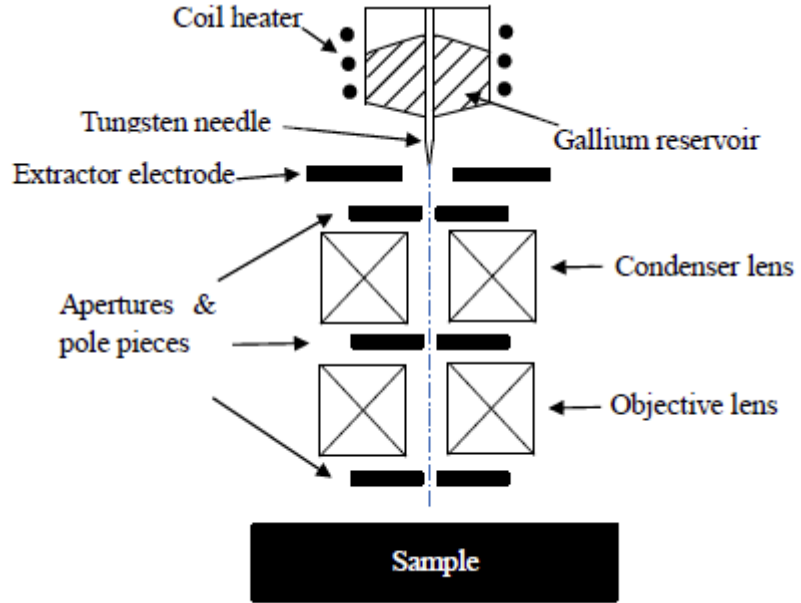


Figure 2.5 Schematic diagram of the LMIS and lens system of an FIB.

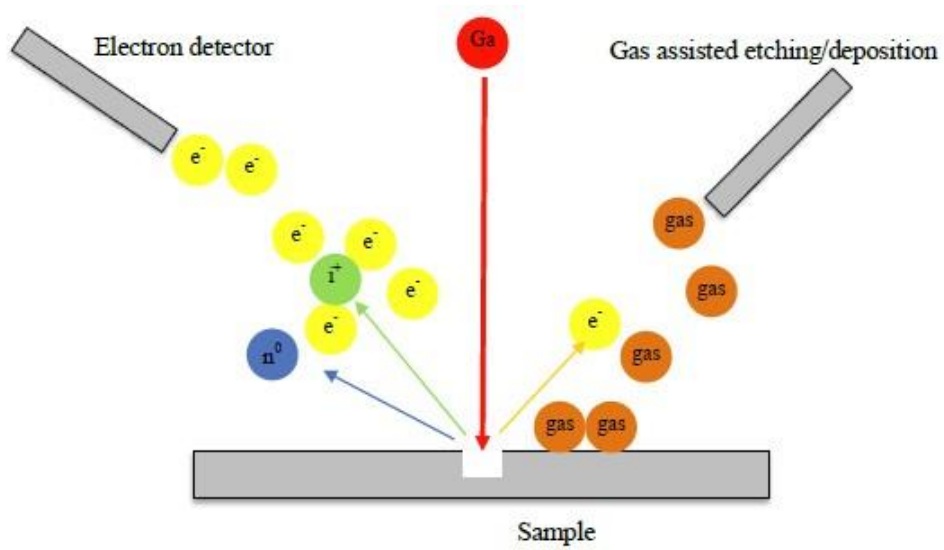


Figure 2.6 Main interaction of Ga^+ with sample material in an FIB.

Chapter 3 Quantification of the Pore Effects on Fatigue Crack Initiation in an A713 Cast Al Alloy using a 3-D FEA Method

3.1 Introduction

Cast aluminum alloys are attractive for use in lightweight and low costs engineering structure applications, such as automotive engines, wheels, and gear boxes, and fan hubs, etc. It is desirable to fully understand the fatigue properties of the cast Al alloys, since, in these applications, the aluminum structures are commonly under dynamic loading in service conditions. It has been well recognized that fatigue cracks are preferably initiated at cast defects inevitably existing in the cast Al alloys, such as gas or shrinkage porosities, coarse particles and inclusions, etc. [25, 30, 38, 42, 51, 52, 57]. Wang and Apelian [42] reported that the aluminum alloys containing cast defects could lower their fatigue lives by more than one order of magnitude than their defect-free counter-parts, and that gas porosities were the most detrimental ones to fatigue properties among all the possible cast defects. Ammar et al. [38] also demonstrated that the fatigue damage was predominantly originated from porosities in their tested samples. Fatigue crack initiation occurs preferably at those pores that are just buried below the surface [25, 30, 38, 40, 41, 51, 52], mainly due to the severe stress/strain concentration at these pores. The maximum range of cyclic plastic shear strain can be regarded as a driving force for fatigue crack formation at a pore [56, 58]. This is also consistent with a theory based on a criterion of minimum strain energy accumulation within multiple slip bands proposed by Venkataraman and co-workers [65, 66]. In their dipole pile-up model, it becomes energetically favorable to nucleate a microcrack at one slip band when the accumulation of dislocation dipole density and strain energy density within the slip bands reaches a critical value with the load cycle. Generally, the fatigue life increases as the size of the pores is reduced [30, 38, 42, 51], since coarser pores close to the surface present higher stress concentration [40]. For the pores of 100 μm ~ 200 μm in diameter, finite element analysis was conducted to demonstrate that the stress-strain concentration [57] and the plastic shear strain range [58] varied with the pore depth from free surface in A356 Al alloys. They reached their peak values when the pore was just buried below the surface. Couper et al. [30] mentioned that further reduction in pore size below ~15 μm would not increase the fatigue life, and Wang et al. [42] suggested a critical minimum pore size of ~25 μm below which fatigue cracks could hardly be initiated at the pores in A356-T6 cast aluminum alloys. However, some previous experimental results showed that fatigue cracks were not necessarily initiated from the larger pores on the surface [41]. Smaller pores, e.g., around 10 μm in diameter, on the surface or below surface could still cause crack initiation [41] even leading to final failure [25, 30]. In order to make a full quantitative analysis of crack initiation at pores, three dimensional finite element modeling was recently used to quantify the stress/strain fields around a micro pore (i.e., 30

μm in size) as a function of position in depth from the surface under monotonic loading in A713 cast Al alloys [62]. It is still desirable to investigate the size effect of pores on fatigue crack initiation and the minimum critical pore size below which fatigue cracks are not initiated at the pores.

In the present work, the relationship of the fatigue crack incubation life with the pore position and size, was analyzed by a 3-D finite element analysis in an A713 cast Al alloy, which can be used to understand the mechanism for multi-site crack initiation and quantitatively identify the fatigue weak-links from all the pores in surface, in order to quantify the effects of pores or particles on the fatigue crack initiation behaviors in the Al alloys, especially for high cycle fatigue applications. This chapter will introduce the FEA simulations in details and the quantification of multi-site initiation will be described in Chapter 4.

3.2 FEA Modeling for Crack Initiation

3.2.1 Experimental observations of the 3-D effects of pores on crack initiation

As shown in Figure 3.1(a), it has been recently observed that fatigue cracks are not necessarily initiated at larger pores but often at relatively smaller pores in surface in A713 cast Al alloys, as marked by arrows in Figure 3.1(a) [41]. This is likely to be attributed to the crack initiating pores mostly being those just buried below the surface, as the case shown in Figure 3.1(b) where the fatigue crack was initiated from a pore just buried below the surface in the A713 Al alloy [41]. They therefore do not appear to be large in size on the surface. In this work, to further verify this 3-D effect of pores on crack initiation, a series of cross-sections by FIB was made through the pore at which a fatigue crack was initiated on the surface of the alloy, as shown in Figure 3.2. Figure 3.2(a) illustrates that the fatigue crack was initiated from a small ($\sim 11.5 \mu\text{m}$ in length) irregular pore on surface in the A713 cast Al alloy, and the depth of the pore at four different locations of the cross-sections varied from $2 \mu\text{m}$ to $10.5 \mu\text{m}$ (Figures 3.2(b-e)). The pore was indeed just buried beneath the surface.

3.2.2 3-D elasto-plastic finite element modeling

To further understand the depth effect of pores on fatigue crack initiation, a three dimensional finite element model was developed to analyze the stress/strain concentration around a micro-pore as a function of pore position in depth from the surface under cyclic loading in A713 cast Al alloys. The commercial finite element analysis (FEA) software ABAQUS 6.11 was used in present work.

For simplicity, the shape of pores was assumed to be spherical in this model, since it could be very time consuming to model irregular shape pores and the effects of pore shape could be neglected in cast Al alloy [53, 56]. A pore of $15 \mu\text{m}$ in diameter at various positions in depth in surface was

considered in this work, since Couper et al. claimed that $\sim 15 \mu\text{m}$ was the minimum critical pore size for initiating a fatigue crack in cast Al alloys [41] and the sizes of most pores were around $\sim 15 \mu\text{m}$ in diameter, according to the pore size distribution measurement in the A713 cast Al alloy [30].

The material used in the FEA model was assumed to be an elasto-plastic isotropic solid with a Young's modulus of 61 GPa, a Poisson's ratio of 0.3 and the yield strength (σ_y) of 171.9 MPa, as experimentally measured in an A713 cast Al alloy. The constitutive behavior of the material was determined by the cyclic stress-strain curve which was modeled with a nonlinear isotropic hardening law. The experimentally measured tensile stress-strain curve of the alloy (Figure 3.3(a)) was used as constitutive behavior of the material in the model. The maximum cyclic stresses of 50%, 55%, 60%, 65%, 70%, 75%, 80%, 85%, 90%, 95%, 100%, and 110% σ_y were applied to the material, respectively, as a sinusoidal wave with a R ratio ($R = \sigma_{\min} / \sigma_{\max}$) of 0.1 (Figure 3.3(b)). The stress-strain behavior of 50 cycles at a maximum cyclic stress of 50% σ_y was simulated in the material using the model, and the simulated hysteresis stress vs. strain loop of the first 5 cycles is shown in Figure 3.3. The results were taken from the region surrounding a micro-pore where the local plastic deformation occurred in the first several cycles, even though the applied stress was only 50% σ_y . Figure 3.3 shows that the stress-strain response of the material is stabilized quickly in the first few cycles. Therefore, only the first several cycles were used for stress and strain analysis in the present work.

As shown in Figure 3.4 (a), a spherical micro-pore of $15 \mu\text{m}$ in diameter was located in the center of a cube of $150 \mu\text{m}^3$, and a symmetrical quarter model (Figure 3.4(a)) was used in FEA simulation. As shown in Figure 3.4(a), cyclic loading was along X axis, and the global mesh of the whole material and the refined mesh around the pore were used in the FEA modeling. The refined mesh surrounding the pore allowed more accurate calculation of stress and strain fields around the pore. Figure 3.4 (b) is a schematic diagram showing the pore position in the matrix: D was the distance between the pore origin and the free surface of matrix, and r was the pore radius. D was positive if the pore center was below the surface, otherwise, D was negative. The D/r ratio was used to represent the pore location in Z direction in the present work: $D/r = 1$ when the pore was just buried below the surface, $D/r = -1$, when the pore was just out of the surface, and $D/r = 0$, when the surface intercepts across the center of the pore. The pore positions in the range of 0 to 2 in D/r were considered in the present work, since the effects of pore positions on the stress concentration around the pore were relatively small, if $D/r < 0$ or $D/r > 2$ [62].

The distributions of stress and strain fields around the pore were subsequently calculated, and the stress and strain concentration factors ($K_{t,\sigma}$ and $K_{t,\varepsilon}$) could then be presented by means of the

nominal far-field stress, σ_{nss} , and strain, ε_{nss} , normalized by the maximum principal stress, σ_{max} , and strain, ε_{max} , namely, $K_{t,\sigma} = \sigma_{max}/\sigma_{nss}$, $K_{t,\varepsilon} = \varepsilon_{max}/\varepsilon_{nss}$, respectively. $K_{t,\sigma}$ and $K_{t,\varepsilon}$ were identical, when only elastic deformation occurs in the alloy. $K_{t,\varepsilon}$ was greater than $K_{t,\sigma}$ once the local plastic deformation occurred around the pore since the increase of stress was much smaller than the increase of strain after material yielded. Therefore, it was necessary to incorporate both the local plastic strain and elastic stress in calculation of the concentration factor, since the local stress could be sufficiently high to exceed the yield strength, and the effective plastic concentration factor, K_t , which was the geometric mean value of $K_{t,\sigma}$ and $K_{t,\varepsilon}$ ($K_t = \sqrt{K_{t,\sigma}K_{t,\varepsilon}}$), was used to represent the stress/strain concentration around the pore in this work.

3.2.3 Methodology for incubation life prediction

The Manson-Coffin law is traditionally used to predict the total fatigue life of a material under a strain controlled fatigue experiment. It relates the number of strain reversals to fatigue failure to the applied plastic strain amplitude. It has been recognized that the plastic strain accumulated around the crack nucleation site can be used to evaluate the fatigue crack initiation. Tanaka and Muraes previously postulated that fatigue crack initiation at inclusions took place when the strain energy accumulated to a certain critical value due to the accumulation of dislocation dipoles round the inclusions [63]. Kato et al. evaluated the net sum of plastic strains in a slip domain accumulated after a certain number of cycles at an applied plastic strain amplitude [67]. Venkataraman et al. proposed a generalized Coffin-Manson law to estimate the crack nucleation life associated with the cumulative plastic strain [65, 66]. When the cross-section of the material is scaled down to a microscopic range, the Coffin-Manson law could be used to estimate the fatigue crack incubation life [56, 58]. Gall, Fan and co-workers used the local maximum cyclic plastic shear strain range, $\Delta\gamma_{max}^p$, averaged over a distance proportional to the pore size on surface with a 2-D finite element model, in the microscopic-scale Coffin-Manson equation to estimate the crack incubation life at a surface pore in cast Al alloys [56, 58]. In the present work, $\Delta\gamma_{max}^p$ was calculated by averaging the shear strain amplitude over a cross-section that was equivalent to the micro-crack plane using a 3-D finite element analysis method. The modified microscopic-scale Coffin-Manson equation used in this work is expressed as [58]

$$CN_{inc}^{\alpha} = \frac{\Delta\gamma_{max}^{p*}}{2} \quad (3.1)$$

where N_{inc} is the incubation life of a fatigue crack at a micro-pore, and C and α are materials constants which were determined from experimental S-N data [58]. For an A713 cast Al alloy $\alpha = -0.426$, and $C = 0.12$.

The modified Coffin-Manson equation was employed in the present work to estimate the incubation life of a fatigue crack nucleated at a surface pore. Figure 3.5 shows the procedure to calculate $\Delta\gamma_{max}^{p*}$. Figure 3.5(a) shows the contours of the calculated maximum plastic shear strain γ_{max}^p around a surface pore. The “+” sign means clockwise, and “-” means anti-clockwise of the the shear strain, and dark blue is the maximum absolute value of the shear strain in Figure 3.5(a). The area used for averaging $\Delta\gamma_{max}^{p*}$ was the area LMN on the critical plane close to 45 degree with the loading direction, as shown in Figure 3.5(b). MN was part of the intercept line between the free surface and the critical plane, and its length was 1.5 μm . This was reasonable, since it was previously investigated that the average initial crack size should be from 0.2 to a few microns for the fatigue crack formation, based on continuum analysis [56]. NL was the tangent line with the pore after point N was determined. The area LMN varied with pore position. γ_{max}^p in region LMN could be extracted from the contours of γ_{max}^p on the critical plane at various pore positions and the applied cyclic stresses. $\Delta\gamma_{max}^{p*}$ was calculated by averaging γ_{max}^p over the area LMN .

3.3 Results and Discussion

3.3.1 The stress and strain distributions around a surface pore

Figure 3.7 shows the distribution of the Von Mises stress (Figure 3.7(a)), σ_{mises} , and the maximum plastic shear strain (Figure 3.7(b), γ_{max}^p , around one half of a spherical pore in the free surface, at a maximum cyclic stress of $70\%\sigma_y$ and $D/r = 0$, assuming the alloy was elasto-plastic. The maximum σ_{mises} contour around the pore occurred on the plane normal to the loading direction, i.e., the plane containing the equatorial plane of the pore in the load direction, while the maximum of γ_{max}^p contour appeared at the edge of the pore on the plane through the pore central point and close to 45 degree with the loading direction. As shown in Figure 3.7(a), the maximum Mises stress is 177.8 MPa. Plastic deformation could occur around the pore because of the stress concentration, though the applied stress was below the yield strength. Figure 3.7(b) shows the plastic shear strain contours around the pore at the maximum applied cyclic stress of $70\%\sigma_y$. The highest γ_{max}^p around the pore was generated in the region near the specimen surface, which might explain why fatigue cracks were preferably initiated near the free surface in cast alloys.

3.3.2 Effects of pore position on stress/strain concentration

Figure 3.8 shows K_t as a function of pore depth in the free surface at the stress level of $100\%\sigma_y$. It can be seen in Figure 3.8 that the effective plastic concentration factor around a pore as a function of pore depth under a maximum cyclic stress of $100\%\sigma_y$. The K_t curve at $100\%\sigma_y$ showed an

extreme value of K_t at $D/r = 1$ (i.e., when the pore was just buried beneath the free surface). The peak value of K_t was 44 at $100\%\sigma_y$. K_t appeared to be approximately axial symmetrical on both sides of the pore position $D/r = 1$. It dropped quickly from its peak when the pore moved away from the position of $D/r = 1$, and was subsided to almost a constant value of 2, when $D/r \geq 2$ or $D/r \approx 0$.

3.3.3 Effects of pore position on driving force

As shown in Figure 3.9, the maximum shear strain amplitude, $\Delta\gamma_{max}^{p*}$, i.e., the driving force for fatigue crack formation at a pore, is plotted against the pore position in depth in the surface region at the applied maximum cyclic stresses of $100\%\sigma_y$. $\Delta\gamma_{max}^{p*}$ was increased sharply with the pore approaching to the position of $D/r = 1$. Unlike the plots of stress/strain concentration vs. depth, the curve in Figure 3.9 show unsymmetrical around $D/r = 1$, indicating that a higher $\Delta\gamma_{max}^{p*}$ generally occurred when a pore became open on the surface than completely buried beneath the surface at the same absolute distance from $D/r = 1$. This was reasonable since strain concentration could be more profound when the pore was open on the surface, since the free surface was less constrained than the interior.

3.3.4 Effects of pore depth on crack incubation life

Higher $\Delta\gamma_{max}^{p*}$, in general, could lead to early fatigue crack nucleation, i.e., shorter incubation life (N_{inc} by Eq. 3.2). As shown in Figure 3.10, the crack incubation life, N_{inc} , is lowered when a pore is located closer to $D/r = 1$ since a much higher strain concentration is generated at this position. By fitting the curve in Figure 3.10, N_{inc} could be estimated as a function of pore depth in the surface (D/r) by,

$$\begin{cases} N_{inc} = (a_1 \times \frac{D}{r} + a_2)^{a_3}, & \frac{D}{r} \leq 1 \\ N_{inc} = (b_1 \times \frac{D}{r} + b_2)^{a_3}, & \frac{D}{r} > 1 \end{cases} \quad (3.2)$$

Where $a_1, a_2, a_3, b_1, b_2, b_3$ are constants at a specific applied cyclic stress.

3.3.5 Effects of applied stress level

Figure 3.11(a) shows K_t as a function of pore depth in the free surface at two different stress levels, $70\%\sigma_y$ and $100\%\sigma_y$, respectively. It can be seen in Figure 3.11(a) that the effective plastic concentration factor around a pore as a function of pore depth under a maximum cyclic stress of $100\%\sigma_y$ is generally higher than that at $70\%\sigma_y$, indicating that the stress/strain concentration around the pore was increased with increase in the applied cyclic stress. As discussed later in the paper, there

was a critical range of the pore in depth within which a fatigue crack could be initiated. It was wider at a higher applied cyclic stress than a relatively low applied cyclic stress. The K_t curves at both 100% σ_y and 70% σ_y showed an extreme value of K_t at $D/r = 1$ (i.e., when the pore was just buried beneath the free surface). The peak value of K_t was 22 at 70% σ_y and 44 at 100% σ_y .

As shown in Figure 3.11(b), the maximum shear strain amplitude, $\Delta\gamma_{max}^{p*}$, i.e., the driving force for fatigue crack formation at a pore, is plotted against the pore position in depth in the surface region at the applied maximum cyclic stresses, 70% σ_y and 100% σ_y , respectively. $\Delta\gamma_{max}^{p*}$ was much higher at 100% σ_y than 70% σ_y in general, which could lead to early fatigue crack nucleation, i.e., shorter incubation life (N_{inc} by Eq. 3.2). As shown in Figure 3.11(c), the crack incubation life, N_{inc} , is decreased with increase in the applied stress, since a higher strain concentration is generated at the higher stress. These constants $a_1, a_2, a_3, b_1, b_2, b_3$ in Eq. 3.2 vary with the applied cyclic stress, as shown in Table 3.2. The effects of pore depth on the crack incubation life at various stress levels could subsequently be calculated using Eq. 3.2, which could substantially reduce the computation burden in quantification of N_{inc} at the pores at different depth positions in the surface of the alloy, knowing the applied stress.

3.3.6 Effects of applied strain level

Three applied cyclic strain amplitudes, 0.2%, 0.4% and 0.6% have been subjected to a same elasto-plastic isotropic solid in the FEA model described in section 3.2, for studying the effects of applied strain level on stress/strain concentration, driving force and incubation life. The maximum cyclic strain of 0.2%, 0.4% and 0.6% were applied to the material, respectively, as a sinusoidal wave with a R ratio ($R = \sigma_{min} / \sigma_{max}$) of 0.1 (Figure 3.12). Figure 3.13 shows K_t as a function of pore depth in the free surface at three different strain levels, 0.2%, 0.4% and 0.6%, respectively. It can be seen in Figure 3.13 that the effective plastic concentration factor around a pore as a function of pore depth under a maximum cyclic strain of 0.6% is generally higher than that at 0.4% and 0.2%, indicating that the stress/strain concentration around the pore was increased with increase in the applied cyclic strain. A critical range of the pore in depth within which a fatigue crack could be initiated was wider at a higher applied cyclic strain than a relatively low applied cyclic strain. The K_t curves at all applied strains of 0.2%, 0.4% and 0.6% showed an extreme value of K_t at $D/r = 1$ (i.e., when the pore was just buried beneath the free surface). The peak value of K_t was 98 at 0.6% strain, 38 at 0.4% and 8 at 0.2%. K_t appeared to be approximately axial symmetrical on both sides of the pore position $D/r = 1$. It dropped quickly from its peak when the pore moved away from the position of $D/r = 1$, and was subsided to almost a constant value, but vary with various applied strain, when $D/r \geq 2$ or $D/r \approx 0$, i.e., 6 for 0.6% strain, 4 for 0.4% strain and 2 for 0.2%. This results indicated that in

low-cycle fatigue, a small pore (15 μm) could be detrimental at large applied strain ($>0.4\%$), though its position is not close to the surface.

As shown in Figures 3.13((a)-(c)), the maximum shear strain amplitude, $\Delta\gamma_{max}^{p*}$, i.e., the driving force for fatigue crack formation at a pore, is plotted against the pore position in depth in the surface region at three different strain levels, 0.2%, 0.4% and 0.6%, respectively. $\Delta\gamma_{max}^{p*}$ was increased sharply with the pore approaching to the position of $D/r = 1$. Unlike the plots of stress/strain concentration vs. depth, all curves in Figures 3.13((a)-(c)) show unsymmetrical around $D/r = 1$, indicating that a higher $\Delta\gamma_{max}^{p*}$ generally occurred when a pore became open on the surface than completely buried beneath the surface at the same absolute distance from $D/r = 1$. This was reasonable since strain concentration could be more profound when the pore was open on the surface, since the free surface was less constrained than the interior. $\Delta\gamma_{max}^{p*}$ was much higher at a maximum cyclic strain of 0.6% than at 0.4% and 0.2%, in general, which could lead to early fatigue crack nucleation, i.e., shorter incubation life (N_{inc} by Eq. 3.2). As shown in Figure 3.13((d)-(e)), the crack incubation life, N_{inc} , is lowered when a pore is located closer to $D/r = 1$, and it is decreased with increase in the applied strain, since a higher strain concentration is generated at the higher applied strain. By fitting these curves in Figure 3.13((d)-(e)), N_{inc} could be estimated as a function of pore depth in the surface (D/r) by Eq. 3.2. $a_1, a_2, a_3, b_1, b_2, b_3$ are constants, but vary with the applied cyclic strain, as shown in Table 3.3.

3.3.7 The size effect of pores on crack initiation

To analyze the pore size effects on crack initiation, the above-mentioned 3-D finite element analysis was carried out around a pore of 5 μm , 15 μm , 50 μm , 100 μm , 150 μm and 200 μm in diameter, respectively, at $D/r = 1$ and $100\%\sigma_y$. Figure 3.15 shows the regions (LMN) for quantification of $\Delta\gamma_{max}^{p*}$ around a smaller (pore A) and a larger (pore B) pores which are both just buried beneath the free surface (i.e., $D/r = 1$). The intercept point between the pores and the surface is M in Figure 3.15. In this work, as shown in Figure 3.15, area LMN was used to determine the size of the initial crack associated with a pore in the surface. The length of MN was fixed, 1.5 μm , on surface, as a surface crack of 1.5 μm could usually be regarded as a short crack. Therefore, $\Delta\gamma_{max}^{p*}$ used in Eq. 3.1 was subsequently calculated by averaging the maximum shear strain amplitude over LMN . The so-calculated $\Delta\gamma_{max}^{p*}$ was dependent on the pore size, i.e., the larger a pore, the higher $\Delta\gamma_{max}^{p*}$ was. As a result, the larger the pore, the shorter the crack incubation life was from the pore, according to Eq. 3.1. Previously, $\Delta\gamma_{max}^{p*}$ was calculated only by averaging the maximum shear strain amplitude along the surface over a distance of 1/10 pore diameter [56], as shown in Figure 3.15. MN' and MN'' are

the surface distances used previously for averaging $\Delta\gamma_{max}^{p*}$ for pores A and B. Since the distance used for averaging the maximum shear strain amplitude proportionally varied with the pore size, this method could not take into account the pore size effect on crack incubation life, in addition to the fact that $\Delta\gamma_{max}^{p*}$ was the average value along a line on the surface. Since the initial crack is 3-dimensional in nature, $\Delta\gamma_{max}^{p*}$ should be the average value over the fractured area of the initial crack, in order to estimate the crack incubation life using Eq. 3.1.

Figure 3.16(a) shows $\Delta\gamma_{max}^{p*}$ (i.e., the driving force for crack initiation) as a function of pore size at $D/r = 1$ and applied stress of $100\%\sigma_y$. $\Delta\gamma_{max}^{p*}$ was ascended sharply from 0 to 0.02 with increase in pore size from 0 to $\sim 100 \mu\text{m}$ in diameter, followed by almost a plateau, e.g. the increment of the driving force was only 0.002 with the increase of pore size from $100 \mu\text{m}$ to $200 \mu\text{m}$. It demonstrated that reducing pore size from $\sim 100 \mu\text{m}$ to 0 would be more effective than from $200 \mu\text{m}$ to $100 \mu\text{m}$ in enhancing the fatigue life, as shown in Figure 3.16(b). The crack incubation life as a function of pore size was remarkably decreased with increase in pore size from $5 \mu\text{m}$ to $100 \mu\text{m}$ and almost saturated when the pore size $> 100 \mu\text{m}$, e.g., the crack incubation life at the pore size of $100 \mu\text{m}$ was 3.23389 by log10, as compared to 3.19004 by log10 at the pore size of $200 \mu\text{m}$ (Figure 3.16(b)).

3.3.8 The minimum critical pore size for initiation

To determine the minimum critical size of a pore at which a fatigue crack could be formed in this alloy, the above-mentioned incubation lives of pores at $D/r = 1$ at $100\%\sigma_y$ were used. The incubation life of the fatigue crack at a pore was minimum when the pore was just buried beneath the free surface, namely, $D/r = 1$, comparing to other pore positions. The fatigue life, 289,355 cycles, of this alloy at $100\%\sigma_y$ stress level was previously measured by experiments [55]. Assuming that the crack incubation took about 98% of the total life, namely, 5.3522 by log10, as shown in the dotted line in Figure 3.17, the minimum critical pore size for fatigue crack nucleation in A713 cast Al alloy at $100\%\sigma_y$ was determined to be $\sim 11 \mu\text{m}$ in diameter, which was roughly consistent with the FIB experimental result that a $\sim 11.5 \mu\text{m}$ in length surface pore could cause fatigue crack initiation (Figure 3.2). This also was reasonably consistent with the previous experimental conclusion that the smallest pore size causing fatigue crack initiation was $\sim 15 \mu\text{m}$ [30].

3.4 Conclusions

- 1) A 3-D FEA method was used to quantitatively analyze the relationship of pore position in depth with stress/strain concentration, driving force for fatigue crack nucleation and fatigue crack incubation life, respectively, at various applied cyclic stresses for a pore of $15 \mu\text{m}$ in diameter.

- 2) FEA results demonstrated that both stress/strain concentration and driving force as a function of pore depth in the free surface were increased with increase in the applied cyclic stress and strain. Higher applied stress and strain led to shorter crack incubation life, and the incubation life was lowered when a pore was located closer to the surface.
- 3) The minimum critical pore size for fatigue crack initiation in the surface was determined to be about 11 μm in diameter by FEA simulation and matching to the experimentally measured fatigue life at the cyclic maximum stress of 100% yield stress in the A713 Al alloy.

Table 3.1 Composition (wt. %) and mechanical properties of A713 cast aluminum alloy

Chemical composition				Mechanical properties	
Cu	Mg	Zn	Al	Yield strength	Elongation
0.72	0.36	7.5	Balance	171.9 MPa	1.28%

Table 3.2 Parameters used in Eq. 3.2 for different applied stresses

Applied stress	a_1	a_2	a_3	b_1	b_2	b_3
70% σ_y	-6.73E+07	6.78E+07	0.13668	5.40E+09	-5.45E+09	0.11816
100% σ_y	-213901	214571.7	0.18394	5.24E+07	-5.29E+07	0.13815

Table 3.3 Parameters used in Eq. 3.2 for different applied strains

Applied strain	a_1	a_2	a_3	b_1	b_2	b_3
0.2%	-62.5843	73.57935	-7.0634	2642.693	-2614.16	0.47057
0.4%	-2.41034	-3.89541	9.78517	2294.06	-2260.08	0.34253
0.6%	-2.99389	-1.13298	6.75532	6730.062	-6526.53	0.24961

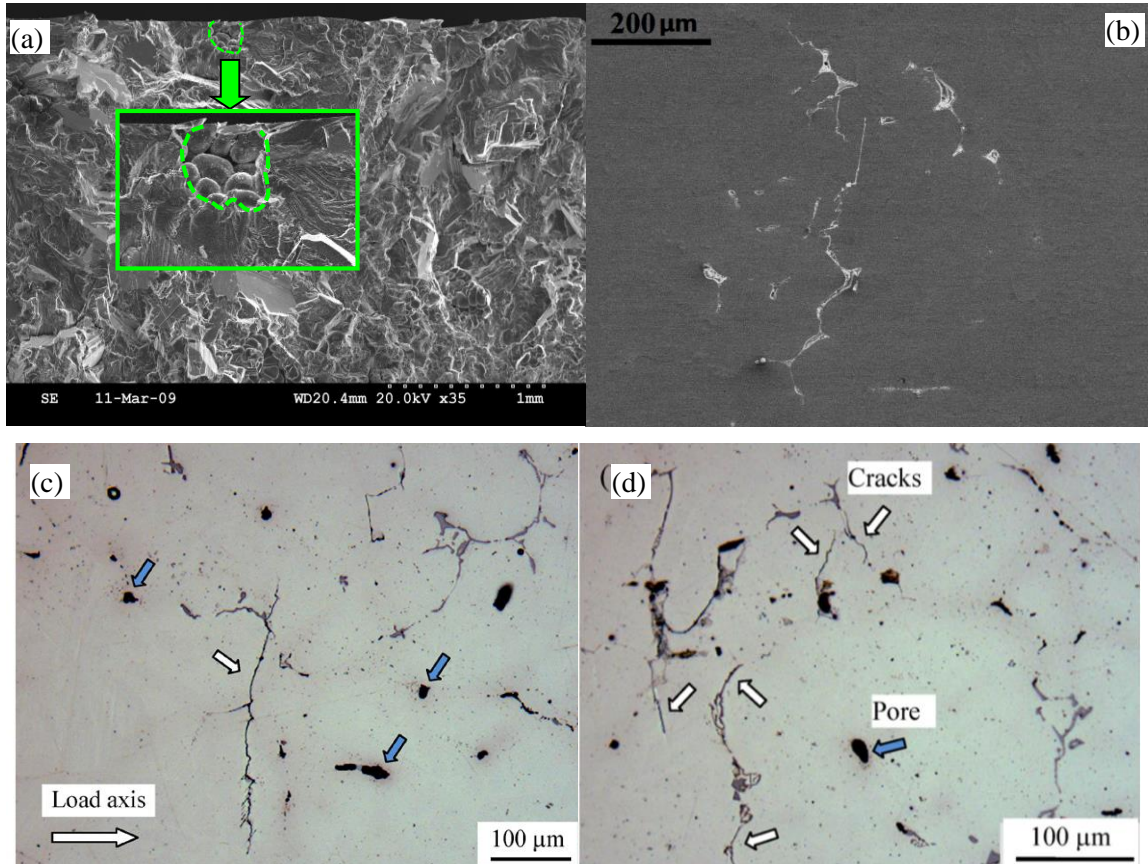


Figure 3.1 (a) SEM micrograph of a typical fracture surface where the crack initiating pore is just buried below the surface in the A713 cast Al alloy [41]; (b) multiple fatigue crack initiation at pores on the sample surface [127]; (c)(d) optical micrographs showing fatigue cracks initiated from locations rather than one of the large pores in surface [41].

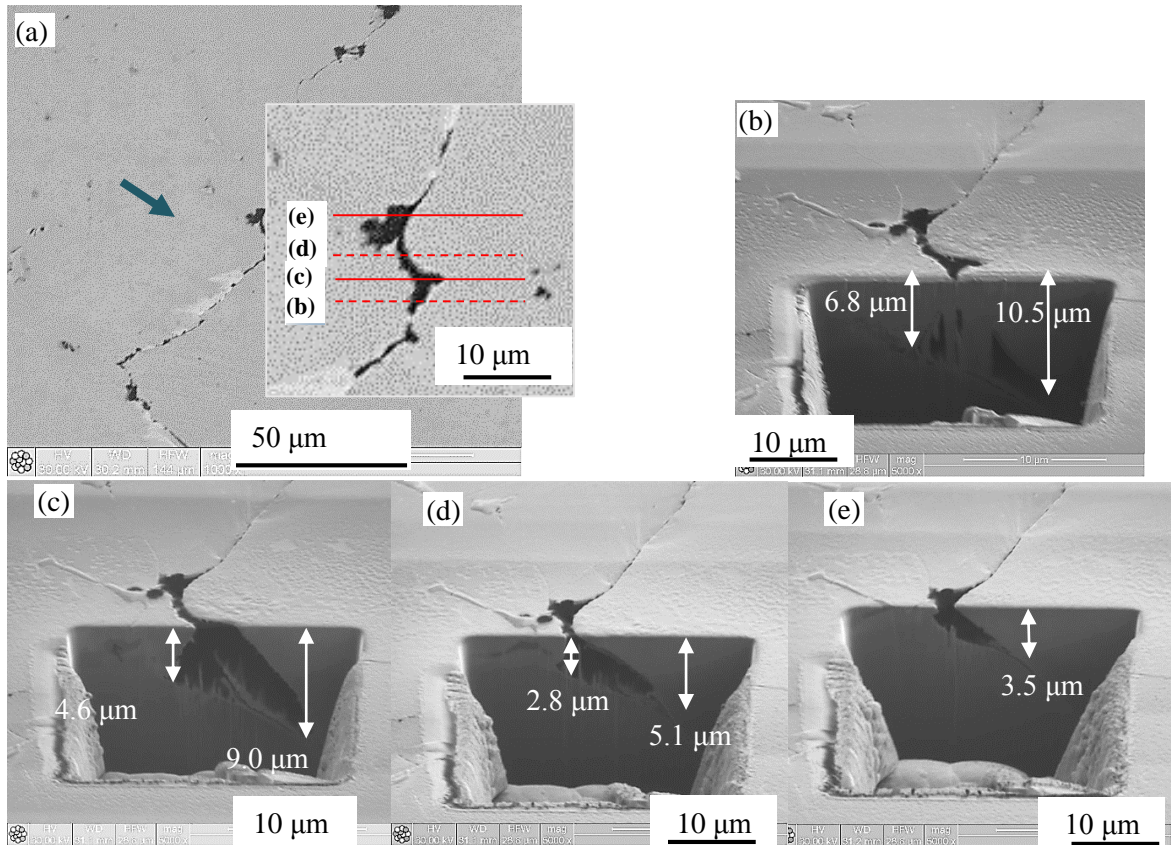


Figure 3.2 (a) Optical micrograph of a long fatigue crack initiated from a narrow irregular-shaped pore ($\sim 11.5 \mu\text{m}$ in length) on the free surface in the A713 cast Al alloy, and lines b, c, d and e are the locations of the micro cross-sections by FIB in (b)-(e), respectively; (b)-(e) SEM micrographs of the cross-sections showing the shapes of the pore in depth, from $2 \mu\text{m}$ to $10.5 \mu\text{m}$.

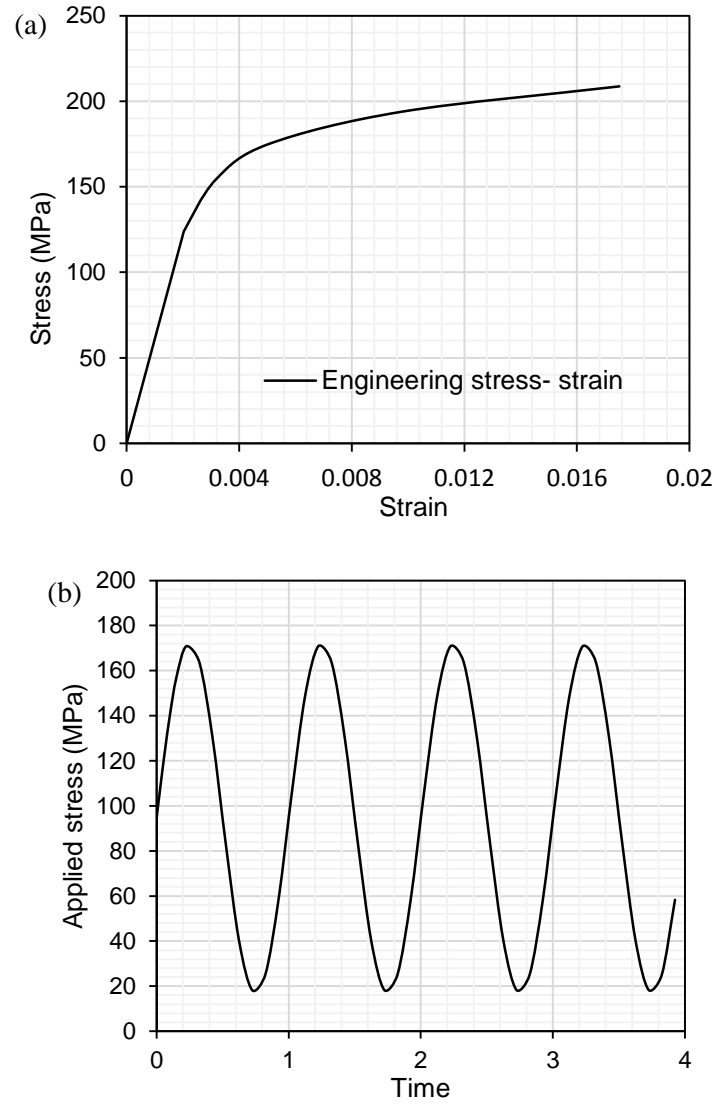


Figure 3.3 The constitutive behavior and applied stress curve for the FEA modeling (a) tensile stress-strain curve measured in a cast 713 Al-Zn alloy, (b) the sinusoidal wave of applied cyclic stress (100% σ_y) curve (at $R = 0.1$) shows cyclically stable behavior after the first load cycle.

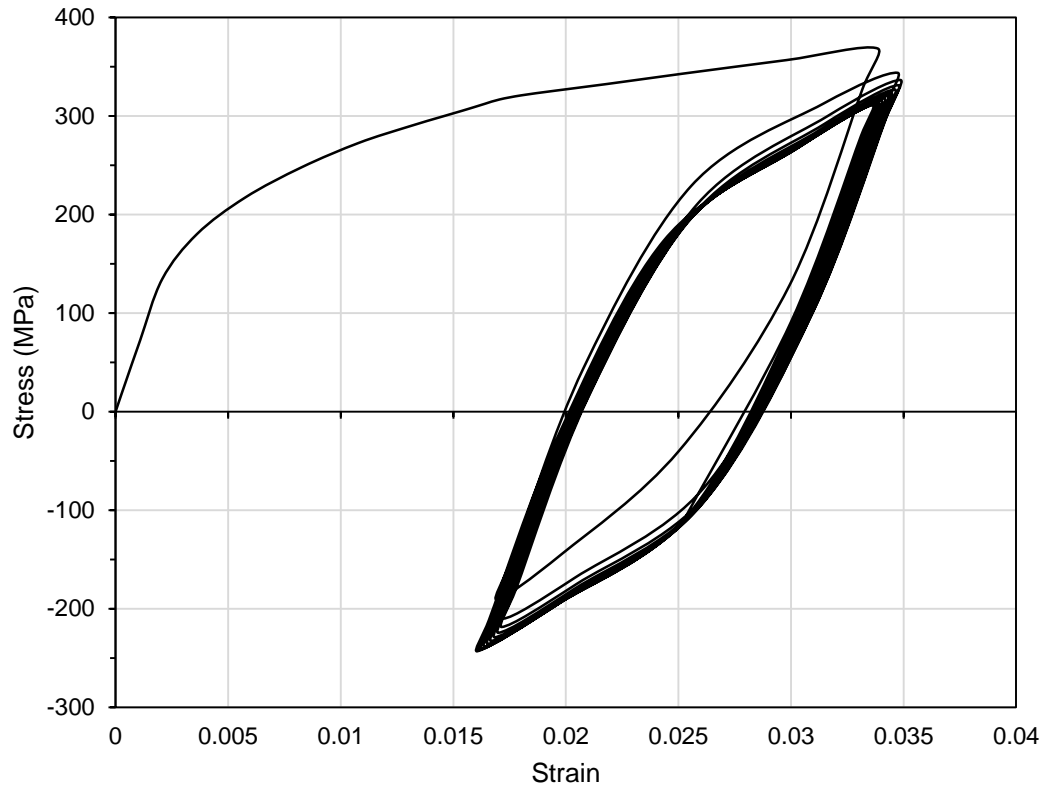
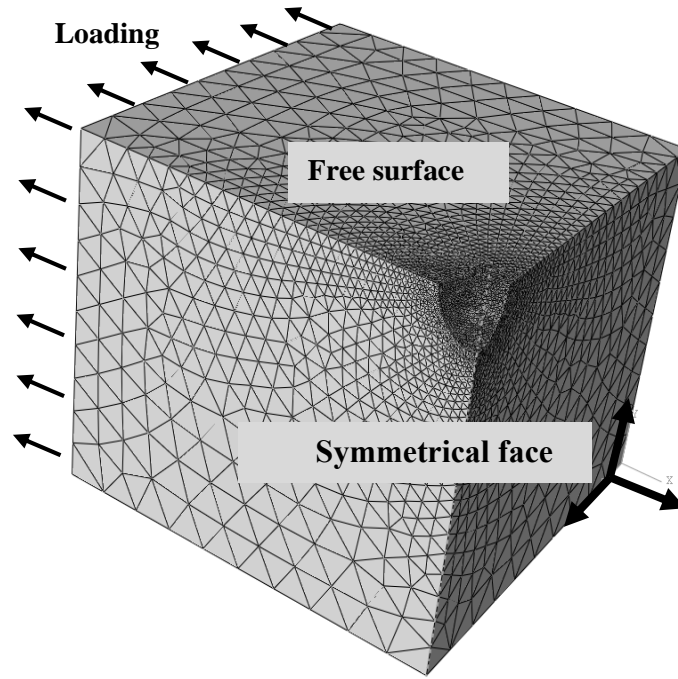


Figure 3.4 The hysteresis loops of stress-strain curve of the first 5 cycles from FEA simulation results, from the region surrounding the micro pore when the applied maximum cyclic stress is $50\%\sigma_y$. The hysteresis loop is saturated to a steady state quickly after only 3 cycles.

(a)



(b)

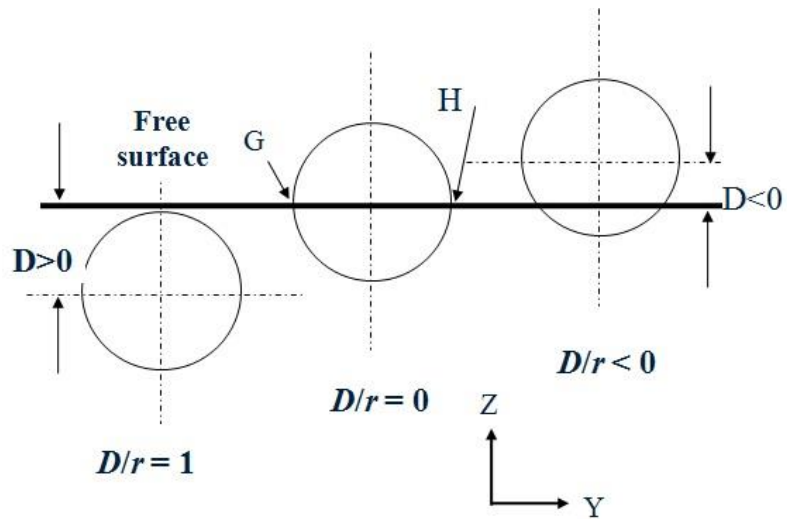


Figure 3.5 FEA Modeling: (a) a symmetrical quarter model with a half of surface pore, and global mesh, (b) typical pore locations in depth in surface.

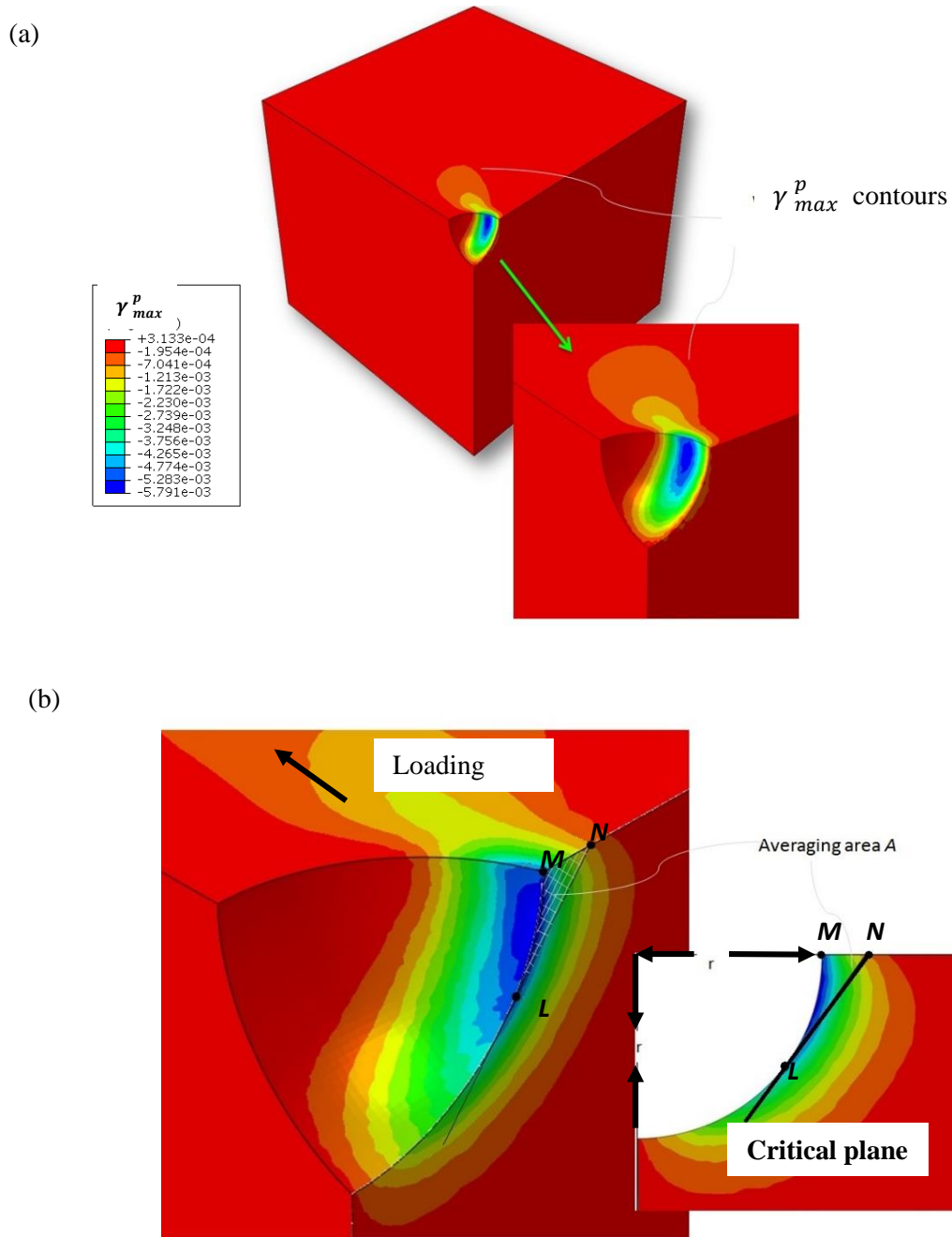


Figure 3.6 Calculation of the average value of maximum shear strain range, γ_{max}^{p*} : (a) the contours of maximum plastic shear strain, γ_{max}^p , (for shear stress/strain: “+” means clockwise, “-“ means anti-clockwise. Dark blue is the maximum absolute value in this result); (b) area MNL used to calculate the average value of γ_{max}^{p*} on the critical plane.

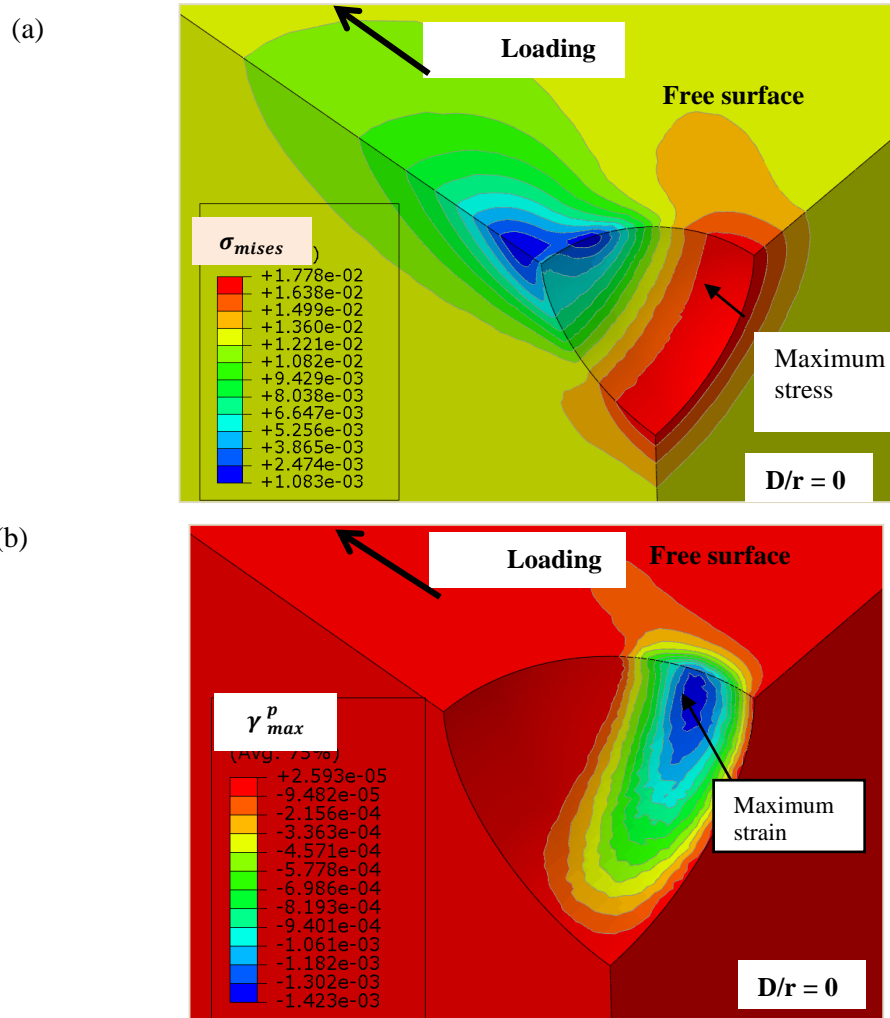


Figure 3.7 The stress/strain fields calculated using an FEA method around a spherical pore at a maximum cyclic stress of $70\%\sigma_y$ and $D/r=0$. (a) The contours of Mises stress around the pore and the maximum value marked by an arrow, the stress in 10^4 MPa; (b) The contours of maximum shear strain around the pore and the maximum value (dark blue) marked by an arrow (“+” and “-“ shear stress/strains associated with strains in clockwise and anti-clockwise directions, respectively).

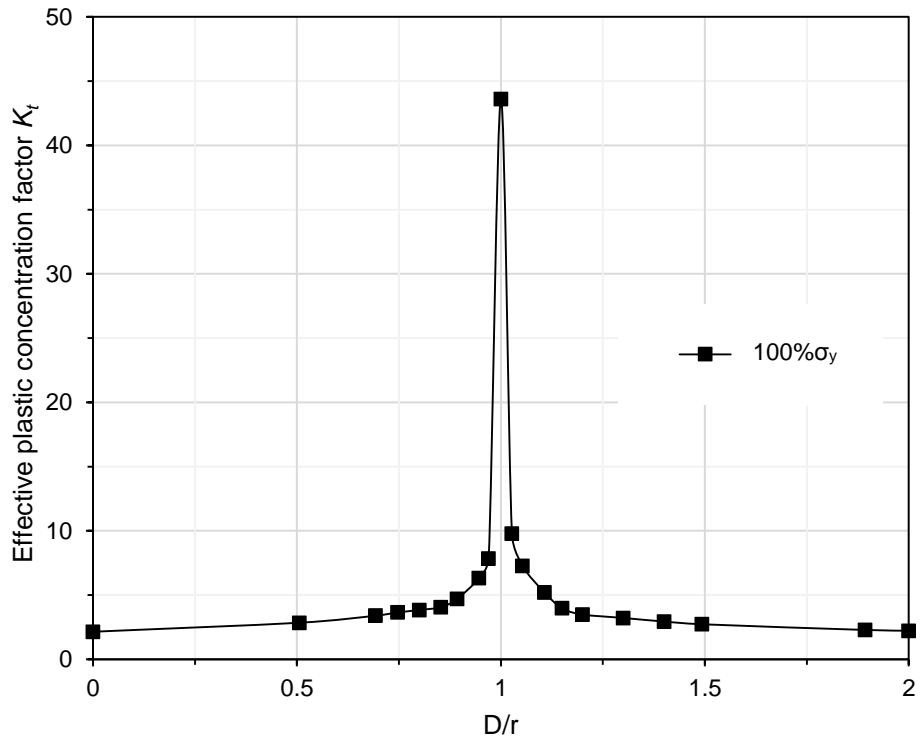


Figure 3.8 The effects of pore depth on stress/strain concentration (K_t), K_t vs. pore depth.

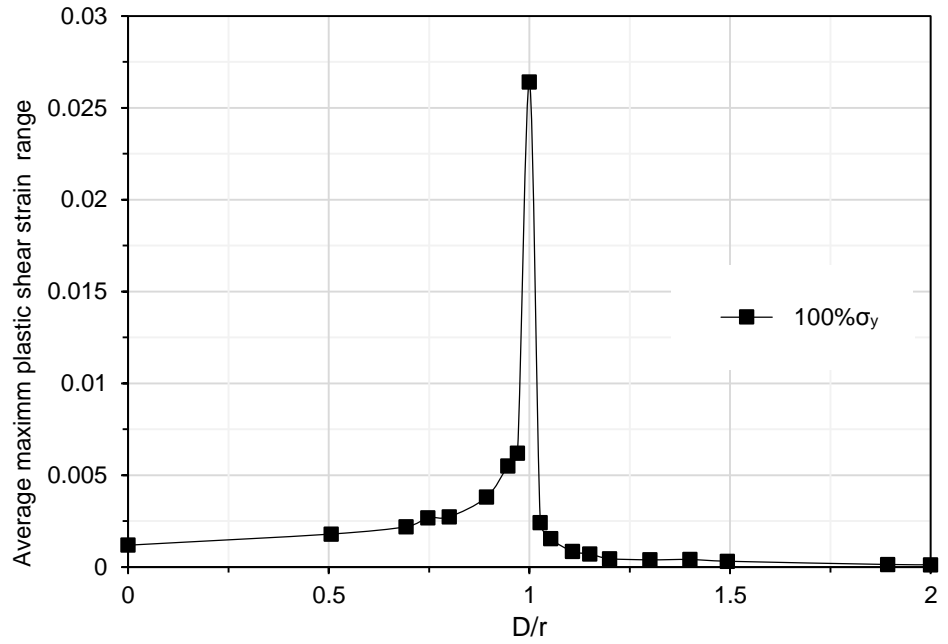


Figure 3.9 The effects of pore depth maximum shear strain amplitude ($\Delta\gamma_{max}^{p*}$), $\Delta\gamma_{max}^{p*}$ vs. pore depth.

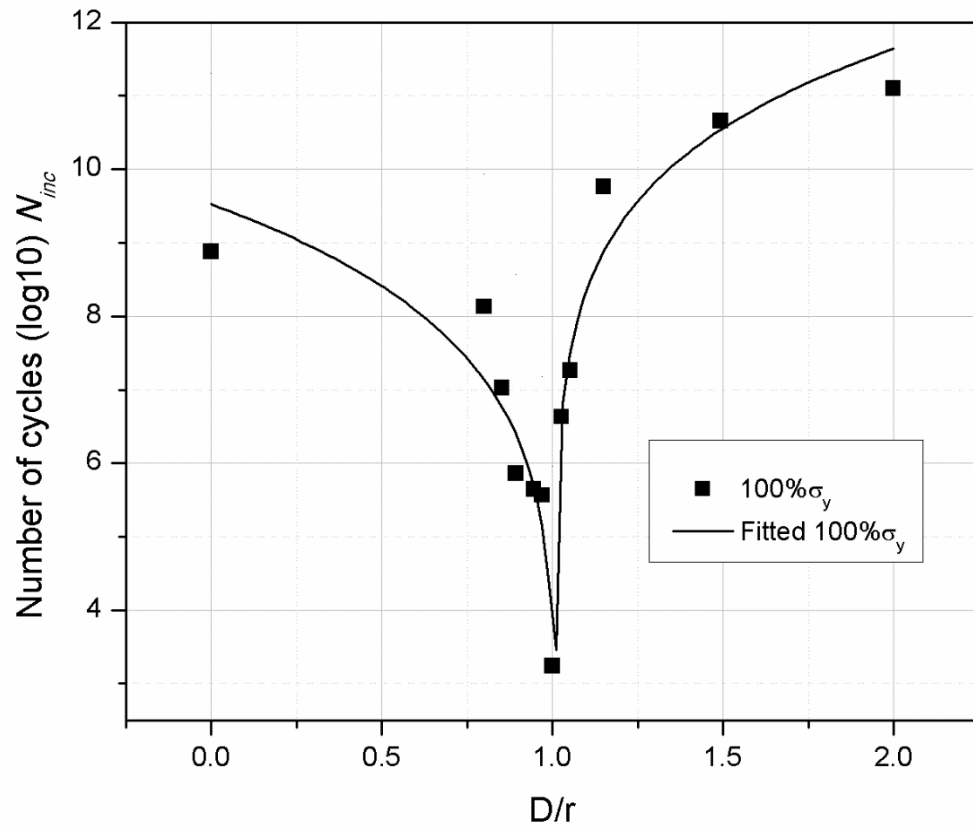
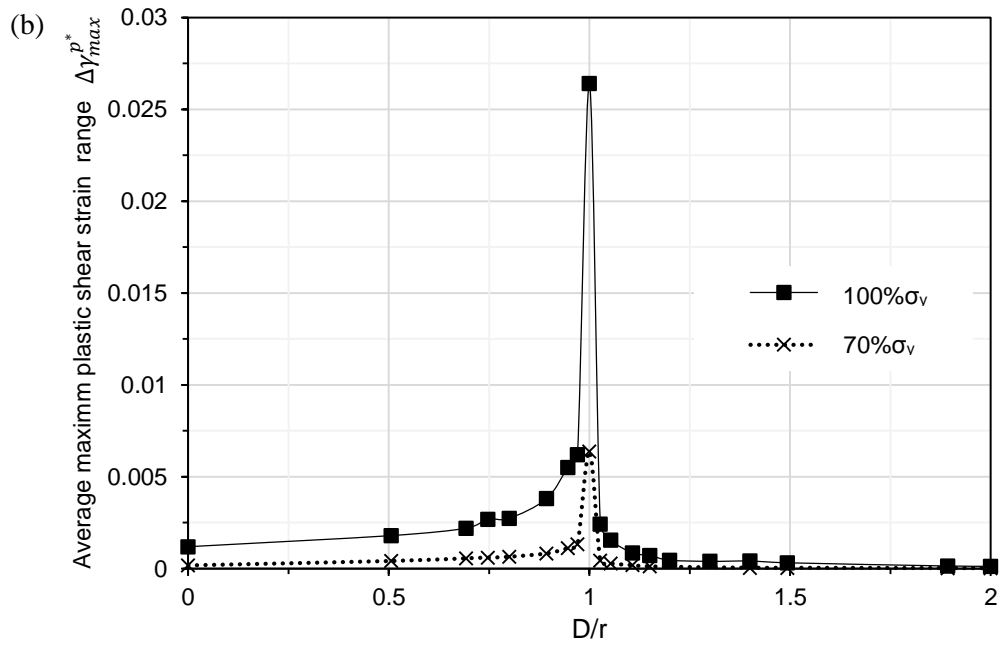
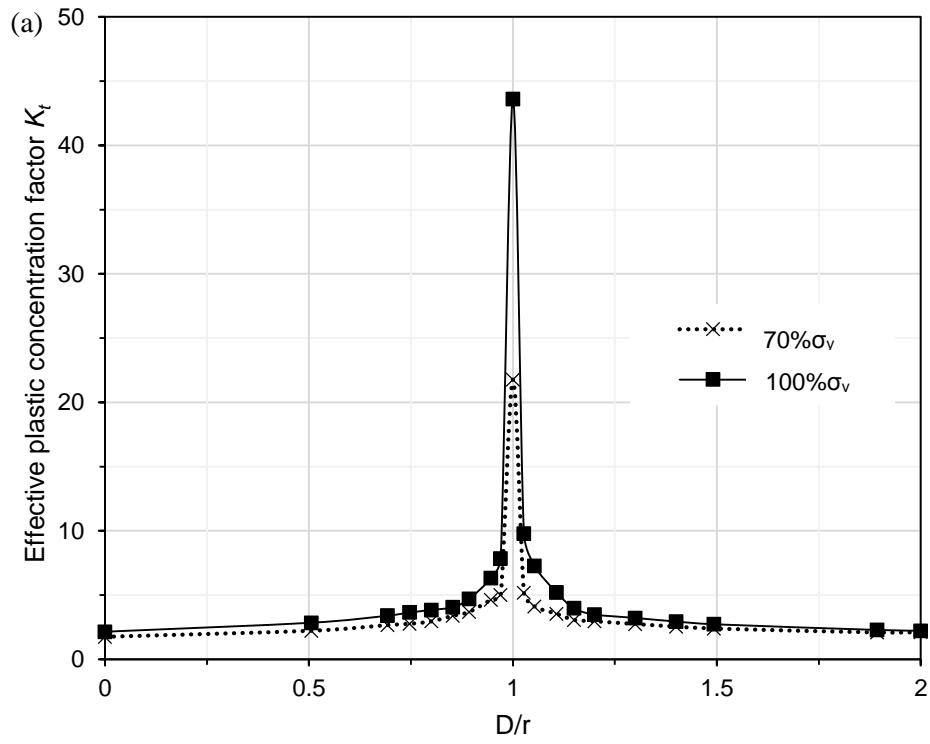


Figure 3.10 The effects of pore depth on crack incubation life (N_{inc}), N_{inc} vs. pore depth.



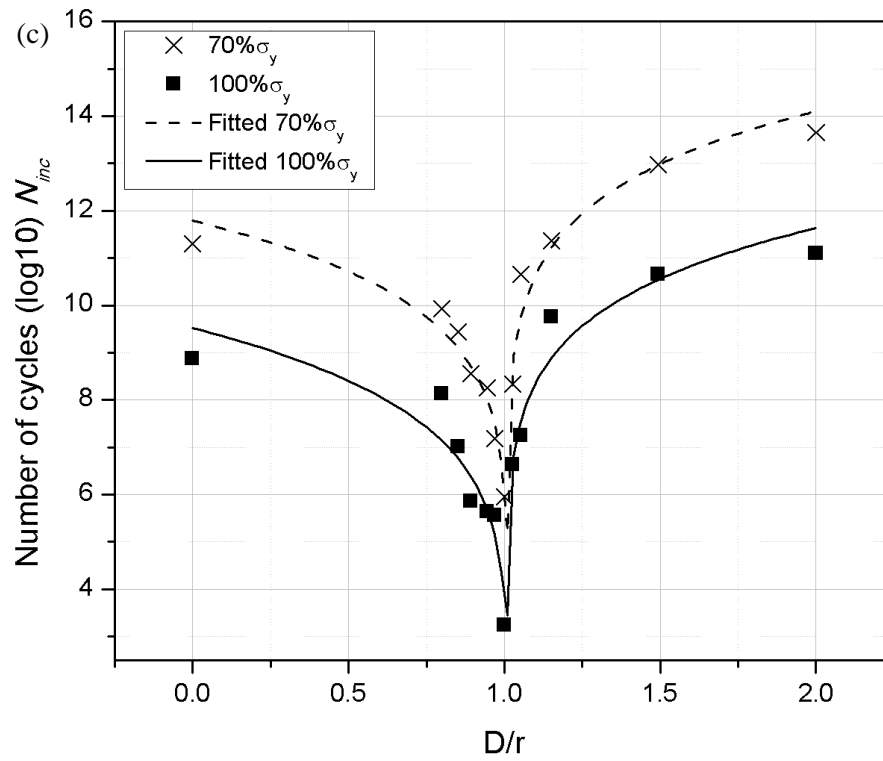


Figure 3.11 The effects of pore depth on stress/strain concentration (K_t), maximum shear strain amplitude ($\Delta\gamma_{max}^{p*}$) and crack incubation life (N_{inc}) at different applied stress, 70% σ_y and 100% σ_y :
 (a) K_t vs. pore depth; (b) $\Delta\gamma_{max}^{p*}$ vs. pore depth; and (c) N_{inc} vs. pore depth.

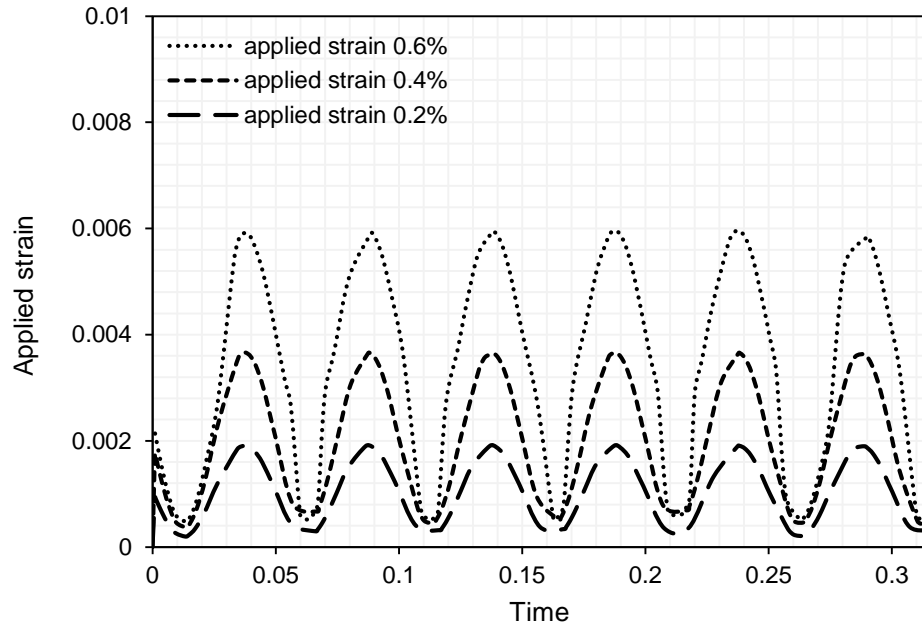


Figure 3.12 Applied cyclic strain of 0.2%, 0.4% and 0.6%.

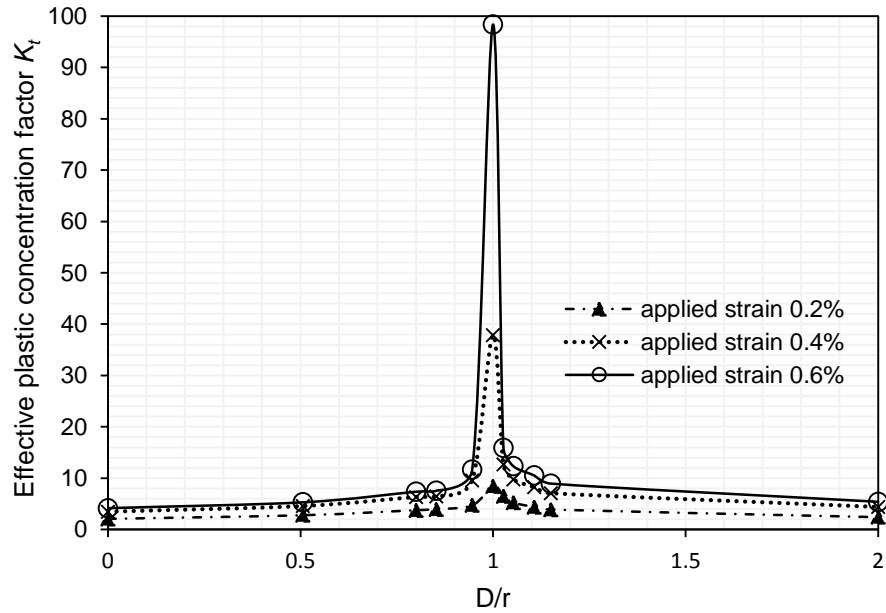


Figure 3.13 The effect of pore position on effective concentration factor K_t at applied strain of 0.2%, 0.4% and 0.6%.

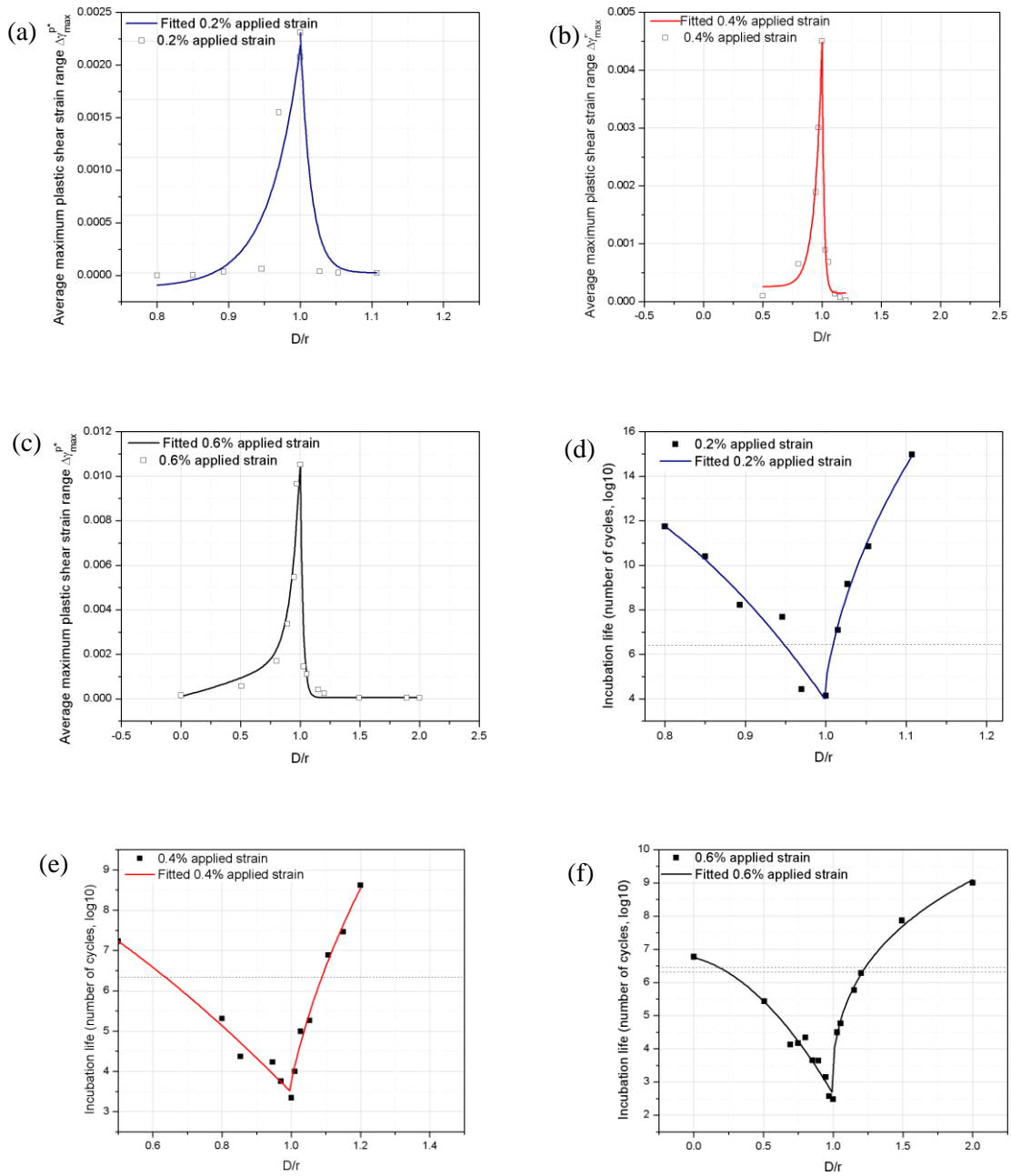


Figure 3.14 The effect of pore position on driving force and incubation life, at applied strain of 0.2%, 0.4% and 0.6%, (a) $\Delta\gamma_{max}^{p*}$ vs. pore depth at 0.2% applied strain; (b) $\Delta\gamma_{max}^{p*}$ vs. pore depth at 0.4% applied strain; (c) $\Delta\gamma_{max}^{p*}$ vs. pore depth at 0.6% applied strain; (d) N_{inc} vs. pore depth at 0.2% applied strain. (e) N_{inc} vs. pore depth at 0.4% applied strain. (f) N_{inc} vs. pore depth at 0.6% applied strain.

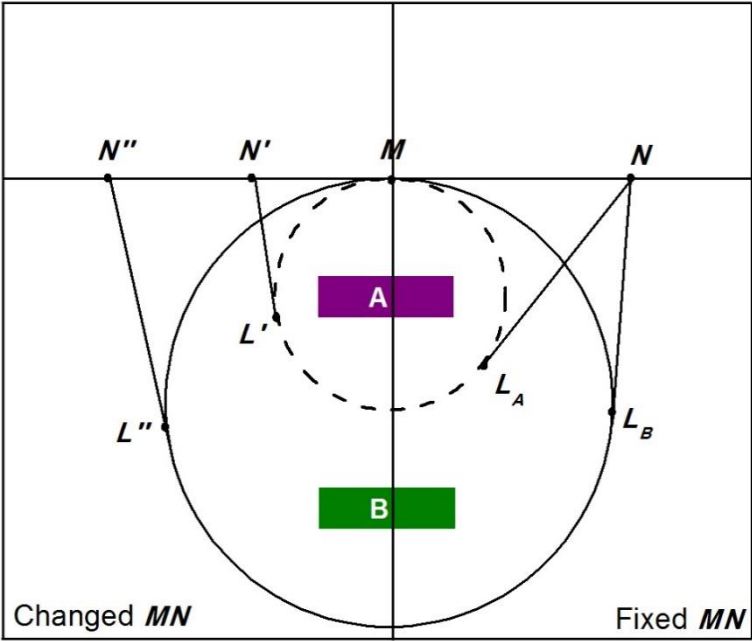
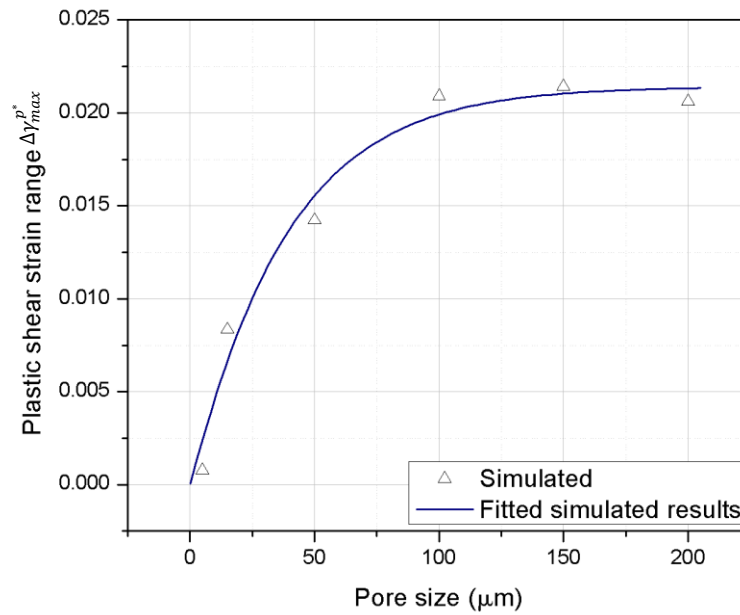


Figure 3.15 Schematic diagram showing the areas ($MN'L'$ and $MN''L''$) used to average the strain shear strain amplitude on the critical plane at a small and a large pore, respectively.

(a)



(b)

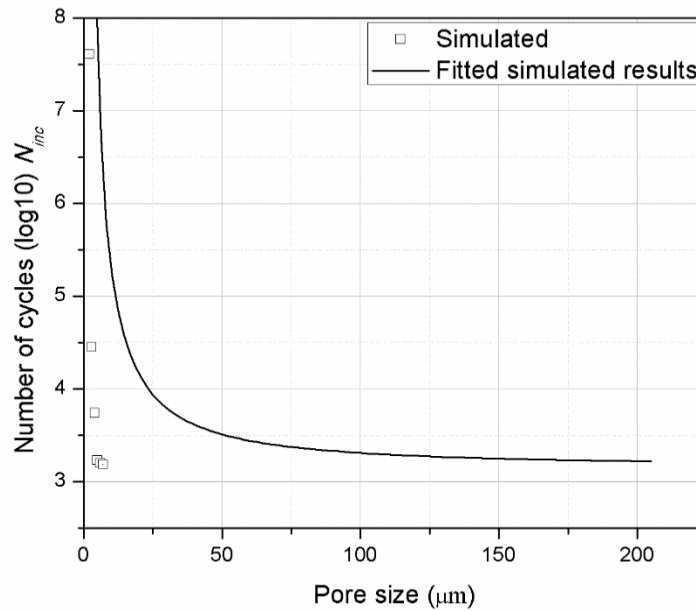


Figure 3.16 (a) The effects of pore size on $\Delta\gamma_{max}^{p*}$, the driving force for fatigue crack nucleated from the pore; (b) the effects of pore size on crack incubation life. $D/r = 1$, applied stress = $100\%\sigma_y$.

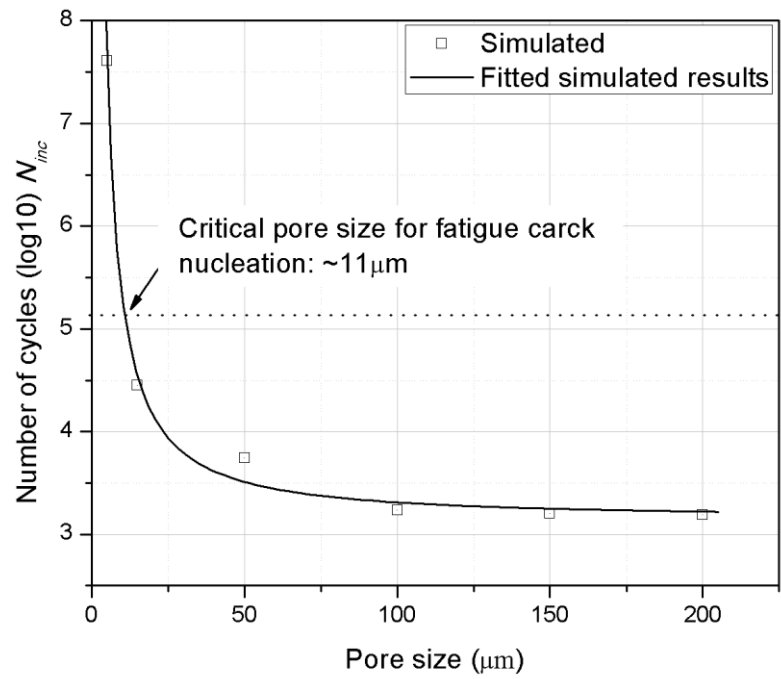


Figure 3.17 The determination of the minimum critical pore size for fatigue crack nucleation.

Chapter 4 A 3-D Pore-sensitive Numerical Model for Quantification of Multi-Site Fatigue Crack Nucleation Behavior

A quantitative model which took into account the 3-D effects of pores on the local stress/strain fields that described in previous chapter, was developed to quantify the fatigue weak-link density and strength distribution in an A713 Al alloy. In the model, a digital pore structure was first constructed using single-sized pores (15 μm in diameter) and multi-sized pores (15 μm , 50 μm and 100 μm in diameter) that had a total volume fraction same as that of the pores measured experimentally in the alloy. In the surface randomly selected by cross-sectioning through the simulated pore structure, the stress and strain fields around each pore in the surface were quantified using the 3-D finite element model under an applied cyclic stress, and the fatigue crack incubation life at the pore was estimated with a micro-scale Manson-Coffin equation. The quantified rate of fatigue crack initiation at these pores was found to be a Weibull function of the applied stress, which was consistent with the experimental result measured in the alloy. The density and strength distribution of fatigue weak-links could then be derived and used to evaluate the fatigue crack initiation properties of the alloy. The probabilistic analysis was used for quantify the stochastic behaviors of the multi-site fatigue crack initiation and the reliability of fatigue crack initiation at each applied cyclic stress in an A713 cast Al alloy, on the basis of the simulated fatigue crack incubation lives at pores which were estimated in the single-sized pore-sensitive model and a multi-sized pore-sensitive model.

4.1 Introduction

Cast aluminum alloys are widely used in engineering structure applications (automotive engines, gear boxes and fan hubs, etc.) because of their high strength-to-weight ratios, low costs and ability for shape forming. However, cast defects, such as gas of shrinkage porosities, coarse particles and inclusions, inevitably existing in the cast Al alloys, are detrimental to fatigue properties [30, 38, 40, 42, 52, 57]. It has been well reported that fatigue cracks are preferably initiated at cast defects in the cast Al alloys, particularly, at gas porosities, which could lead to the lower fatigue lives of aluminum alloys containing defects by more than one order of magnitudes compared to their defect-free parts [42]. In A356 Al alloys, fractographic study demonstrated that only large pores (>100 μm) close to the sample surface were found to be responsible for crack initiation [40], which has been supported by finite element analysis that was conducted for the pores of 100 μm ~200 μm in diameter to reveal that the stress/strain concentration reached their peak values when the pore was just buried below the surface [57]. However, some previous experimental observations showed that small pores, e.g., around 10 μm in diameter (Figure 3.1), in the surface or below surface could still cause crack initiation [41, 128]. Although the majority of these fatigue cracks would not propagate to long cracks,

nor result in final failure, it is sufficiently desirable to thoroughly and quantitatively characterize multi-site crack nucleation behaviors at pores in cast Al alloys.

It has been recognized that there is no direct correlation between the size distribution of pores/particles and the fatigue crack nucleation behaviors can be found in cast Al alloys and Al-Cu alloys respectively [41, 53], though the general findings show that the fatigue life increases as the size of the pores is reduced [30, 38, 42]. In order to quantitatively characterize the pores/particles where fatigue crack nucleation occurs in Al alloys, an experimental technique has recently been developed characterize the density and strength distribution of crack initiation sites in these alloys[37, 41, 54, 55]. A 3-D pore-sensitive model with only one-sized pores (15 μm in diameter) was consequently developed and validated by experimental results to quantify the fatigue weak-links density and strength distribution as a function of the applied cyclic stress in an A713 cast Al alloy, which took into account of the 3-D effects of porosities by 3-D finite element analysis [128]. Assuming that pores were all 15 μm in diameter, the rate of crack initiation from the pores in surface could be quantified to be a Weibull function of the applied cyclic stress, which was consistent with the experimentally measured results in the alloy [55, 128]. For minimizing the existing discrepancies between the experimental and simulated results using only single-sized pores in model [128], an improved 3-D pore-sensitive model containing multi-sized pores (15, 50 and 100 μm in diameter) with experimental size distribution has been established in present work. The establishment of the single-sized pore model and multi-sized pore model will be described in this chapter. The models can be used for probabilistic analysis for quantifying the reliability of fatigue crack initiation at each given applied cyclic stress in the A713 cast Al alloy on the basis of the simulated fatigue crack incubation life spectrums at pores which were estimated in the single-sized pore model and multi-sized pore-sensitive model. The technique could be significant for understanding the fatigue crack initiation behaviors in the Al alloys, especially for high cycle fatigue applications, since it is hardly to measure the fatigue crack initiation life by experiments.

In the experiments [41, 55] for quantifying the fatigue weak-link density and strength distribution, four-point bend fatigue tests were conducted on A713 cast Al alloys using a self-aligning four-point rig. The maximum cyclic stress (relatively to yield strength) used in these tests range from the fatigue limit to the ultimate tensile strength. Two samples at each stress level were conducted in the S-N curve measurement, and the crack population found in the same area in each sample after fatigue tests was measured and the rate of crack initiation rate was calculated divided by pore population [55]. The pore size distribution was then statistically quantified from optical micrographs that were taken before fatigue tests, as shown in Figure 4.1. It could be used for distributing multi-sized pores into the 3-D quantitative model.

4.23-D Pore-sensitive model for multi-site crack nucleation

4.2.1 3-D digital pore-containing microstructure

In this work, a 3-D pore-sensitive numerical model was developed to simulate the multi-site fatigue crack initiation behaviors, and for quantification of fatigue weak-links density and strength distribution. It could be validated by the experimental results. The stereology theory was applied in this model to determination of the 3-D volume fraction and size distribution of the spherical pores from the 2-D area fraction of the pore size measured experimentally in A713 cast Al alloys, to construct a 3-D digital pore structure.

4.2.2 Framework of the model

The basic process to quantify fatigue weak-links in the modeling is summarized as follows.

- (1) Experimental measurements of the area fraction of pores and pore size distribution by a metallographic method;
- (2) Conversion of the measured area number density of pores into its volume number density using the principle that the pores volume density \approx experimental area fraction of pores (stereology theory);
- (3) Construction of a 3-D digital pore structure by randomly distributing spherical pores in a cube of $1,000 \times 1,000 \times 1,000 \mu\text{m}^3$, see Figure 4.2(a);
- (4) Random selection of the sample surface by more than 2,000 times cross-sectioning through the digital pore structure, as shown in Figure 4.2(b);
- (5) Data collection from all sample surfaces (cross-sections): *i.e.* the size and position of each pore on the surface and around the surface within $[0, 2]$ of D/r ; the area fraction of pores on each surface;
- (6) Verification of the model stability by comparing the averaging area fraction of surfaces from simulations and the experimental area fraction;
- (7) Quantification of crack population and crack nucleation rate from surface pores;
- (8) Characterization of fatigue weak-links density and distribution;
- (9) Validation of the model by comparison between simulated results and experimental results.

4.2.3 Experimental verification for the stability of the model

Because of the overwhelming computing time required for each pore size used in the simulation of crack incubation life at pores, a 3-D digital microstructure with only single-sized pores of $15 \mu\text{m}$ in diameter was constructed at first, in order to verify this methodology for quantification of fatigue weak-links. The work on multi-sized pore simulation of fatigue weak-links will be introduced in later sections. The total area fraction of pores was measured experimentally to be 2.826% in the

A713 cast Al alloy. The number of pores in a 3-D cube of $10^9 \mu\text{m}^3$ (1 mm^3), was calculated to be 16,000, namely, the volume number density was $16 \times 10^{-6} \mu\text{m}^{-3}$ (Table 4.1), when the total area fraction of pores was 2.826%. These pores were randomly placed into the cube under the condition that two pores were not allowed to be in direct contact with each other. The total pore area fraction measured on the simulated digital surface which was a cross-section randomly selected through the cube was averaged over number of sampling (i.e., sample size). As shown in Figure 4.3, at a sample size of 50, the difference between the experimental and simulated pore area fraction on surface is around 5%, but it decreases sharply with increase in sample size, e.g. it is only 1% at a sample size of 500. The difference became only 0.5% when the sampling size was 2,000, indicating that the above digital pore structure became consistent with the experimental one in terms of the total pore area fraction when the sampling size $\geq 2,000$. In other words, the volume of the digital pore structure constructed in a single sampling needs to be $\geq 2 \times 10^{12} \mu\text{m}^3$ ($2,000 \text{ mm}^3$), in order to provide a consistent pore structure with a total area fraction of 2.826% on the cross-section randomly selected from the digital structure.

4.3 Determination of the fatigue crack from a pore

Although the strength distribution of fatigue weak-links in an A713 cast Al alloy was experimentally characterized previously, as reported in ref. [41], work still needs to be carried out to quantify the fatigue weak-links based on the pore structure of the alloy. To identify those pores that could lead to fatigue crack initiation in the surface of a 3-D digital microstructure, it was assumed that the crack incubation lives in the alloy at an applied cyclic stress had to be within 98% of the total life to failure at an applied cyclic stress, since the crack nucleation and early propagation could consume over 90% of the total life in an alloy [129, 130]. This was used to identify the detrimental pores at each applied cyclic stress level, through comparison between the experimentally measured fatigue life and the simulated incubation life at each stress. The relevant experimental data can be found in ref. [55]. In this work, the rate of crack initiation (i.e., percentage of the pores at which fatigue cracks are initiated) instead of the number of cracks (i.e., fatigue weak-link density) was computed at different applied cyclic stresses, in order to eliminate the influence of possible variation in pore density from one sample to another on fatigue crack density (Figure 4.4) in the A713 alloy.

Figure 4.5 shows that the simulated incubation life at 100% σ_y with the maximum cyclic stress of 171.9 MPa as a function of D/r. The critical crack incubation life, N_{inc} , 98% of the experimentally measured total life to failure, in an A713 sample at 100% σ_y , was 5.35220 in a log scale as the dash line in Figure 4.5. The window between points A and B in D/r was from 0.903569 to 1.025535, which was the corresponding critical range of the pore position (D/r ratio) for identifying those

detrimental pores that formed fatigue cracks with a life less than 5.35220 in a log scale at 100% σ_y applied cyclic stress. The critical range of D/r for the pore of 15 μm in diameter varied with the applied stress.

4.4 The technique for quantification of fatigue weak-links density and strength distribution

The total number (N) of fatigue cracks generated on the surface of a failed sample of the alloys studied, like A713 alloy [41], AA 8090 [54], 2026 [55] and 7075 [37] alloy, was a Weibull type function of the applied maximum stress, σ ,

$$N = N_0 \left(1 - \exp \left[-k \left(\frac{\sigma - \sigma_0}{\sigma_0} \right)^m \right] \right) \quad (4.1)$$

Where N_0 is the maximum possible number of cracks per mm^2 generated in the surface area of $10 \times 6 \text{ mm}^2$ at the stress level close to the ultimate tensile strength (σ_s), i.e. maximum possible weak-links density ($N_0 / (10 \times 6 \text{ mm}^2)$); k , constant; m , Weibull modulus; and σ_0 is fatigue limit. The parameters, k and m , can be determined by taking the logarithm twice of Eq. (4.1) and then fitting the crack population data in a plot of $\ln(-\ln(1 - \frac{N}{N_0}))$ vs. $\ln(\frac{\sigma}{\sigma_0} - 1)$, in a linear relationship,

$$\ln(-\ln(1 - \frac{N}{N_0})) = m \ln(\frac{\sigma}{\sigma_0} - 1) \quad (4.2)$$

m is the slope and $\ln k$ is the intercept values on the $\ln(-\ln(1 - \frac{N}{N_0}))$ axis when $\ln(\frac{\sigma}{\sigma_0} - 1)$ is zero. In order to obtain more reasonable values of the parameters (k and m), only the data points of crack population at higher stress levels were used for the curve fitting, as even a variation of 1 or 2 crack could lead to a measurement error over 50% at a stress level just above the fatigue limit due to very low total number of cracks (1 or 2) at the stress level. By taking the derivative of Eq. (4.1), the strength distribution of fatigue weak-links, n , can be expressed,

$$n = C N_0 \left(\frac{k m}{\sigma_0} \right) \left(\frac{\sigma - \sigma_0}{\sigma_0} \right)^{m-1} \exp \left[-k \left(\frac{\sigma - \sigma_0}{\sigma_0} \right)^m \right] \quad (4.3)$$

where

$$N_0 = \int_0^{+\infty} N d\sigma \quad (4.4)$$

n represents the number of cracks generated at a specific stress level σ . C is a scaling constant and N_0 is the weak-links density.

4.5 Multi-sized Pore Model

A 3-D multi-sized pore-sensitive quantitative model was improved from a 3-D single-sized model which was introduced in details in previous section. The model was developed to simulate the multi-site fatigue crack initiation behaviors, for quantification of fatigue weak-link density and strength distribution, and to estimate the reliability of fatigue crack initiation in an alloy. In this model, a 3-D digital pore structure was first constructed using multi-sized spherical pores with experimentally measured pore size distribution and with a volume fraction which was determined by the 2-D area fraction of the pores measured experimentally in A713 cast Al alloys. Using a same process with single-sized pore model as described in previous sections, multi-sized spherical pores were randomly distributed in a cube (Figure 4.2). Seeing the pore size distribution in Figure 4.1, it can be divided into three ranges of pore size: 0~30 μm , 30~70 μm and 70~100 μm , with fraction of 91.854%, 7.940% and 0.205%, respectively. It was reasonable to use the finite element results of the pore of 15 μm in diameter represents the pore size in 0~30 μm , 50 μm for 30~70 μm and 100 μm for 70~100 μm , respectively. Therefore, in the 3-D pore structure, the volume fraction of pore of 15 μm , 50 μm and 100 μm in diameter was 91.854%, 7.940% and 0.205%, respectively. The total volume fraction was approximately same with the total area fraction of pores which was measured experimentally to be 2.826% in the A713 cast Al alloy. The number of pores in a 3-D cube of 1 mm^3 ($10^9 \mu\text{m}^3$), was calculated to be 3283 for 15 μm , 276 for 50 μm and 8 for 100 μm in diameter, namely, the number density of 15 μm pore was 3283 mm^{-3} , 276 mm^{-3} for 50 μm pore and 8 mm^{-3} for 100 μm pore. These pores were randomly placed into the cube and two pores were not allowed to be in direct contact with each other. The model became stable when the sampling size $\geq 2,000$ by using a same examining method introduced in section 4.2. The size and position of each pore on the surface were collected from all sample surfaces which were randomly selected by 2,000 times cross-sectioning through the digital pore structure. The fatigue crack incubation lives from those pores on the surface were consequently calculated using the quantitative finite element results. Since the crack initiation and early propagation could consume over 90% of total life in an alloy [129, 130], it was assumed that the incubation lives has to be within 98% of total life at a stress level measured experimentally in A713 cast Al alloys to identify those pores that could lead to crack initiation in surface of the alloy. The crack population and crack nucleation rate (cracking rate, normalized by pore population) were subsequently computed in the multi-sized quantitative model.

4.6 Pore position distribution

After 2,000 times cross-sectioning through the digital pore structure, all the pore positions were collected with changing pore size, number density in single-sized pore model and multi-sized pore model. The results, in Figure 4.6, show that the probability for pore position during $D/r = [0, 2.5]$ keep constantly, no matter the pore size and number density is increasing, no matter in single-sized

pore model or in multi-sized pore model. It indicates that the probability is exactly same for a pore locates at any position. However, it can be reasonably speculated that pores with higher number density will have more pores located in critical positions to cause crack initiation, comparing to low number density.

4.7 Results and Discussion for Quantification of Fatigue Weak-links and Strength Distribution

The crack population (crack density, per mm²) and rates of crack initiation (per mm², namely, cracking rate) were quantified in the alloy with a pore area fraction (i.e., pore density) of 2.826%, respectively, using the single-sized pore-sensitive model and the multi-sized pore-sensitive model mentioned earlier in the chapter. The calculation of the crack population and the cracking rates was repeated 2,000 times, namely, running the model 2,000 times, using the same parameters and conditions the average result is plotted against the maximum cyclic stress normalized by the yield strength of the alloy.

4.7.1 The crack population vs stress

Figure 4.7 shows that the crack population was increased with increasing stress level in both single-sized pore model and multi-sized pore model. As described in previous section, the number density in the single-sized pore model was 16000 per mm³ with 15 μm pore, and the number density in the multi-sized pore model was 3,567 per mm³, including 3283 per mm³ for 15 μm pore, 276 per mm³ for 50 μm pore and 8 per mm³ for 100 μm pore, as Table 4.2 shown. This result shows that a pore with 15 μm in diameter can only initiate crack when the applied maximum cyclic stress is larger than 70% yield strength. Therefore, at the stress level larger than 70% yield strength, the crack population in single-sized model is larger than in multi-sized model due to higher number density of pores with 15 μm in diameter. In Figure 4.7, when the stress level was in a range of 50% to 70% yield strength, there was no crack initiated at pores with 15 μm in diameter in single-sized model, but cracks were still initiated in multi-sized pore model which were dominated by large pores, namely, 50 μm and 100 μm, though the number density of both large pores was relatively low.

4.7.2 The rate of crack initiation vs. Stress

In Figure 4.8, the cracking rate is increased with increase in the applied stress in all the pore-sensitive models. The single-sized pore model and multi-sized pore model (3-sized) have been described in previous sections. For the 2-sized pore model, the portion of 15 μm: 50 μm is 99:1 with area fraction of 2.826%. With only 1% large pores in the 2-sized pore model, the cracking rate has been increased obviously, indicating that large pores dominated the crack initiation.

4.7.3 Effects of number density and pore size on crack population and cracking rate

Figure 4.9 shows that the crack population is increased with increase of number density, due to that there were more pores located in the critical range of positions for crack initiation with higher number density. But there was no influence on the cracking rate in the alloy as Figure 4.10 shown, since higher number density not only cause more cracks, there were more pores on the surfaces as well. Figure 4.11 shows the similar results with Figure 4.7, indicating that with same area fraction of 2.826% the large pores with 50 μm in diameter can cause the crack initiation when the stress level was lower than 70% yield strength with relatively small number density. At stress levels of larger than 70% yield strength, there were more cracks in the model with small pores due to higher number density than in the model with large pores with low number density. Figure 4.12 shows that the cracking rate is increased with the increase in pore size with the same area fraction of 2.826%, though the number density was lower with larger pore size.

4.7.4 Fatigue weak-link density and strength distribution of fatigue weak-links

As shown in Figure 4.13, the initiation rate (R) of the fatigue cracks generated on the surface was a Weibull distribution function of the applied maximum stress, σ , consistent with the experimental results observed in this alloy and other high strength Al alloys such as A713 [41], AA8090 [54], and 7075 [37]. In the present work, the curves of the crack initiation rate vs stress from simulated data in single-sized model and multi-sized model, were fitted using a 3-parameters Weibull function,

$$R = R_0 \left(1 - \exp \left[-k \left(\frac{\sigma - \sigma_0}{\sigma_0} \right)^m \right] \right) \quad (4.4)$$

where R_0 is the maximum possible cracking rate at the maximum cyclic stress close to the ultimate tensile strength ($\sigma_s = 210 \text{ MPa}$, $122.2\% \sigma_y$) of the alloy, $R_0 = 0.048 \text{ mm}^{-2}$; k constant; m , Weibull modulus; and σ_0 fatigue limit, $66.9\% \sigma_y$ which was measured previously in experiments [41].

The parameters k and m can be determined by taking logarithm of Eq. (4.4) twice and then fitting a linear line in the plot of $\ln \left(-\ln \left(1 - \frac{R}{R_0} \right) \right)$ vs $\ln \left(\frac{\sigma}{\sigma_0} - 1 \right)$ [54],

$$\ln \left(-\ln \left(1 - \frac{R}{R_0} \right) \right) = m \ln \left(\frac{\sigma}{\sigma_0} - 1 \right) + \ln k \quad (4.5)$$

as shown in Figure 4.14. Both plots of R vs σ of the simulated results in single-sized and multi-sized model are shown in Figure 4.13, and the determined m and k are listed by linear fitting lines in Figure 4.14. Both curves fitted with the Weibull function were plotted in Figure 4.13.

The constants in Eq. 4.4 are listed in Table 4.3. The value of R_0 (the cracking rate at a stress level close to ultimate tensile strength, $\sigma_s = 210$ MPa, 122.2% σ_y) was estimated to be 0.048 mm⁻² when the cracking rate of experimental data was 0.045 mm⁻² at 110% σ_y . Although R_0 might be determined more accurately at a high stress level close to the ultimate tensile strength in fatigue tests, current results were still valid to quantify the relationship between the rate of crack initiation and the applied cyclic maximum stress in this alloy. As shown in Figure 4.13, the dash dot dot and dash lines are the Weibull fitting curves of simulated data in single-sized and multi-sized model, respectively. Both curves were apparent asymptotes at both ends of stress, *i.e.* at a low stress level below the fatigue limit, the cracking rate was asymptotic with respect to zero because that there should be no cracks initiated, namely, zero cracking rate, until the stress level was over the fatigue limit. At a high stress level close to the ultimate strength, the cracking rate was the maximum and was asymptotic towards a constant value of 0.048 mm⁻². In the middle region of these applied stress level, the cracking rate was sharply increased. The saturation of the cracking rate at highest stress level can be considered as the result of shielding effect. It can be seen that the cracking rate of in multi-sized pore model was higher than the results in single-sized pore model at each stress level, and the reason for this discrepancy as mentioned above was that the simulated results in single-sized pore model obtained by only using a single sized pores (15 μ m) in the model.

The strength distribution of fatigue weak-links can be derived by taking derivative of the Eq. 4.4, as described in [54],

$$R = CR_0 \left(\frac{k\sigma}{\sigma_0} \right) \left(\frac{\sigma - \sigma_0}{\sigma_0} \right)^{m-1} \exp \left[-k \left(\frac{\sigma - \sigma_0}{\sigma_0} \right)^m \right] \quad (4.6)$$

where R is the characteristic strength distribution of fatigue weak-links in materials, representing the value of the rate of crack initiation per mm² at a maximum cyclic stress σ , and the scaling constant C depends on the unit of σ used in Eq. 4.6 that can be determined by,

$$R_0 = \int_0^{+\infty} R d\sigma \quad (4.7)$$

where R_0 was defined as the weak-link density since the value of R was divided by the surface area. Both R_0 and R can be regarded as materials fatigue properties to evaluate the performance of an alloy by means of fatigue crack initiation behavior. In the A713 cast Al alloy, the fatigue weak-link distribution and the strength distribution of fatigue weak-links are directly related to those porosities that could lead to the formation of fatigue cracks at different cyclic stress levels, so that the strength distribution of the weak-links can be determined by measuring the rate of crack initiation per unit area at each cyclic stress level. For a material with better fatigue performance, R_0 should be as small

as possible, R as narrow as possible, and the stress of its peak as high as possible in its strength distribution, which means that the material has smaller weak-link density, narrower range of stress level for crack initiation and higher stress level corresponding to the maximum cracking rate, respectively. Therefore, development of the capability to quantify those fatigue properties is desirable for both materials design and manufacturing to enhance the fatigue properties of the materials.

Figure 4.15 is the strength distributions of fatigue weak-links for the simulated results in single-sized (dash line) and multi-sized (dash dot dot line) pore model. The peak for the simulated results in single-sized pore model was about $0.0011007 \text{ mm}^{-2}$ at $90\%\sigma_y$, while the peak for the results in the multi-sized pore model was $0.0013611 \text{ mm}^{-2}$ at $85\%\sigma_y$.

4.7.5 Validation of simulation by experiments

In the present work, the curves of the crack initiation rate *vs* stress from both experimental and simulated data, were fitted using a 3-parameters Weibull function as Eq. 4.4. All plots of R *vs* σ of the simulated and experimental results are shown in Figure 4.16, and the determined m and k are listed in Table 3. In the curve fitting of the R *vs* σ plot of the experimental data, the data at the higher stresses were mainly used (Figure 4.17), as the data points at the stress close to the fatigue limit, $70\%\sigma_y$, was not reliable since there was only 1 or 2 crack could be initiated at this stress. For example, a difference of one crack could cause a significant error in the measured crack population at the stress just above the fatigue limit [54]. Therefore, the data points in the slope region were used for curve fitting, and the curves fitted with the Weibull function were also plotted in Figure 4.16.

The constants in Eq. 4.4, obtained by curve fitting, are listed in Table 4.3. In Figure 4.16, it can be seen that the cracking rate of experimental data was higher than the simulated in single-sized pore model at each stress level, and the reason for this discrepancy as mentioned above was that this simulated results obtained by only using a single sized pores ($15 \mu\text{m}$) in the model. Multi-sized pore model can be used to improve the accuracy of the simulated

Figure 4.16 also shows the simulated rates of fatigue crack initiation in multi-sized pore model (3-sized pore model in this work) has good agreement with experimental results. The discrepancies between the simulated rates of fatigue crack initiation in single-sized pore model and experimental results have been minimized by using multi-sized pores in the 3-D pore-sensitive model. Figure 4.18 shows the simulated strength distributions of fatigue weak-link density which was derived from the Weibull fitting curve in Figure 4.16. The peak value of the experimental strength distribution in A713 Al alloy was $0.0013784 \text{ mm}^{-2}$ at $80\%\sigma_y$, $0.0013611 \text{ mm}^{-2}$ at $85\%\sigma_y$ in multi-sized pore model

and $0.0011007 \text{ mm}^{-2}$ at $90\% \sigma_y$ in single-sized pore model. The difference of the peak value has been reduced from 20% using only single-sized pores to 1.3% using multi-sized pores to quantify the fatigue weak-link strength distribution. It demonstrated that this multi-sized pore-sensitive quantitative model developed in this work was excellent capable to identify the fatigue weak-links, to quantify their density and strength distribution in a cast Al alloy. The weak-links density and strength distribution can be regarded as materials fatigue properties to evaluate the performance of an alloy by means of fatigue multi-sites crack initiation behaviors. Unlike stress vs. number of cycles to fatigue (S-N) curves, existing a large scatter due to the randomness of inherent microstructural inhomogeneities in an alloy, the technique for quantifying the fatigue weak-links can be directly used to quantitatively characterize the formation of fatigue cracks from the microstructural inhomogeneities (particles and porosities) at different cyclic stress levels. Therefore, this multi-sized pore-sensitive model could be an effective tool for both materials design and manufacturing to advance the fatigue properties of the materials.

4.8 Prediction of Crack Incubation Life

4.8.1 Distribution of incubation lives in single-sized model

At different cyclic stress levels, the distribution of incubation lives (N_{inc}) at a specific applied stress could also be obtained (Figure 4.19). Figure 4.19 shows the fatigue crack incubation life spectra at applied stresses of 75%, 80%, 85%, 90%, 95%, 100% and 110% σ_y , respectively. These crack incubation life distributions are also presented together with the experimentally measured S-N data of the alloy, as shown in Figure 4.20(a). In Figure 4.20(a), the solid horizontal line at each maximum cyclic stress represents the range of the crack incubation life from 0 to 100% of the cracks, the rectangle bar is the range of life from 25% to 75% of the cracks, the markers (-) are the minimum and maximum lives, respectively, the asterisk (*) are the 1% to 99% of the value, and the cube in the box is the mean value. At the highest stress, the number of cracks was largest and the minimum incubation life was lowest among all stress levels. The range of the crack incubation life distribution at high stress level with much more cracks, *e.g.* as many as $\sim 20,000$ cracks at $110\% \sigma_y$, $\sim 6,500$ cracks at $90\% \sigma_y$, was wider than those at low stress level with only few cracks, ~ 96 cracks at $75\% \sigma_y$. The distribution of incubation life was narrowed down to almost a single point at low stress level for the reason that there should be only one or two cracks initiated at this stress level in experiments. The scattering life spectrum at a higher stress indicated multi-site crack initiation behaviors.

The mean value and minimum value of incubation life spectrum at each stress were taken from Figure 4.20(a) and were depicted as Figure 4.20(b) shown. The minimum and mean value both were linearly increased with decreasing stress level, and the mean value was in the position between the

minimum value and total life until the stress level decreased to 75% σ_y with a same value for minimum and mean. Both the minimum and mean value of incubation life at different stress level are significant for describing the fatigue properties in this material, *e.g.* a crack with the incubation life of minimum value could be regarded as the most detrimental crack which may propagate to a main crack for most conservative and safest consideration, and considering the mean value as a criterion for fatigue crack initiation is a relative safe and general option.

Figure 4.20(c) shows the percentage of crack initiation life (minimum value and mean value) of total life (incubation life/total life, %) linearly decreased with the increase of stress level. As mentioned above, there was discrepancies existed between the experimentally measured results and simulated results in single-sized model, which can be minimized by the multi-sized model.

4.8.2 Distribution of incubation lives in multi-sized model

Figure 4.21 shows the calculated fatigue crack incubation lives at different stresses from pores in 2,000 sample surfaces with cross-sectioning 2,000 times the pore structure in the 3-D multi-sized pore-sensitive quantitative model. As Figure 4.21 shown, the fatigue crack population was increased with increase of the applied stress, *e.g.* ~6,000 cracks at 110% σ_y , and only small amount cracks at low stress level, ~40 cracks at 50% σ_y . Figure 4.22(a) shows the fatigue crack incubation life spectra at applied stresses of 50%, 60%, 70%, 80%, 90%, 100% and 110% σ_y , respectively. The crack incubation life distributions are also presented together with the experimentally measured S-N data of the alloy in Figure 4.22(a). In Figure 4.22(a), the markers represent same statistical values as described in the last section. At the highest stress, the number of cracks was largest and the minimum incubation life was lowest among all stress levels. The range of the crack incubation life distribution at high stress level with much more cracks was wider than those at low stress level with small amount cracks. The distribution of incubation life was narrowed down at low stress level for the reason that there should be only few cracks initiated at this stress level. The large scatter in life spectrum at higher applied stress indicated a multi-site crack initiation behaviors at higher stress level in this alloy, which was consistent with the experimental observations in AA7075 [37]. In Figure 4.21 and 4.22(a), it should be noted that there still cracks can be initiated from pores though the stress level was lower than the experimentally measured fatigue limit which was 66.9% σ_y , *i.e.*, 126 cracks at 60% σ_y and 39 cracks at 50% σ_y . It was reasonable because the experimental S-N data was not statistical stable result with only conducting two samples at each stress level while the quantitative model were conducted for 2,000 times.

The minimum value, mean value and maximum value of incubation life spectrum at each stress were taken from Figure 4.22(a) and were depicted as Figure 4.22(b) shown. The minimum, mean and

maximum value all were linearly increased with decreasing stress level. The linear fitted curve for the minimum value of the incubation life distribution (dash line in Figure 4.22(b)) can be regarded as the survival curve for crack initiation at each stress level, which demonstrated that the crack would never be initiated from the pore if the number of cyclic loading was below than the survival curve.

4.8.3 Percentage of fatigue initiation life

Figure 4.23 shows the percentage of crack initiation life (minimum, mean and maximum value) of total life (incubation life/total life, %) was linearly decreased with the increase of stress level in the multi-sized pore model. At an applied maximum stress just above the fatigue limit, it could be as much as 96% of the total fatigue life, compared to just as much as 69% at the maximum stress of $110\%\sigma_y$. This result was consistent with the findings that fatigue cracks could take over 95% of the total life to initiate at very high cycle fatigue and even over 99% in fatigue life beyond 5×10^7 cycles in high strength steels [131], while cracks would take shorter for initiation in low cycle fatigue. The percentage of the minimum value and the mean value of incubation life spectra both were relative low as shown in Figure 4.23 compared to the maximum value, i.e., for the minimum value, $\sim 2\%$ the total life at the stress of $70\%\sigma_y$ and $\sim 0.1\%$ at the stress level of $110\%\sigma_y$; for the mean value, $\sim 26\%$ at $0\%\sigma_y$ and $\sim 14\%$ at $110\%\sigma_y$. The results can be used to understand the mechanisms of the multi-site crack nucleation behaviors in Al alloys. A crack with the incubation life of minimum or mean value was one of those cracks that were initiated from pores very early but never propagate to long cracks, so that this crack was not relevant to the most detrimental crack that lead to final failure in the alloy. However, a crack with the incubation life of maximum value probably can be regarded as the most detrimental crack which may propagate to a main crack because it was the latest crack to be initiated with the longest incubation life. The cracks were not initiated at the same time, but initiated one by one. One new crack can be initiated from a micro-defect only because the last crack was arrested for some reasons, such as large grain boundary resistance with large crack plane deflection on grain boundary [132] and low driving force with very thin particle in Al-Cu alloy [133]. Therefore, the pore-sensitive model was valid to simulate the multi-site crack nucleation behaviors by predicting the crack incubation lives at detrimental pores in cast Al alloys while the incubation lives of fatigue cracks are hardly to be experimentally measured.

4.9 The Fatigue Reliability of Crack Initiation

Figure 4.24 and 4.25 gives the cumulative probabilities for fatigue crack incubation life at different applied cyclic stresses in 2,000 times simulations in the single-sized pore model and the multi-sized pore model, based on the data in Figure 4.17 and Figure 4.19, respectively. A two-parameter Weibull distribution was used to adequately represent the scatter in the fatigue incubation lives, that is:

$$P = 1 - \exp[-(\frac{N}{k})^m] \quad (4.8)$$

where N is the simulated fatigue incubation life; m is the Weibull modulus; k is the characteristic fatigue value; and P is the cumulative fatigue crack initiation probability (Figure 4.24 and Figure 4.25), estimated from the fatigue crack incubation life distribution in Figure 4.17 and Figure 4.19, by

$$P = \frac{i}{n+1} \quad (4.9)$$

where n is the total crack population at a certain stress level, and the fatigue incubation life N for each crack was calculated. The values of N were ordered from the smallest to the largest and the smallest one was ascribed as index value i of 1, the next higher value an index value of 2 and so forth. The highest life was then assigned an index of N_s , i.e. $n_{N(1)} < n_{N(2)} < \dots < n_{N(i)} < n_{N(i+1)} < \dots < n_{N(s)}$; and i is the number of cracks, for $1 \leq i \leq n$. $\ln\{\ln[1/(1 - P)]\}$ was calculated and plotted against $\ln N$ at each stress level. In the linear fitting plots of $\ln\{\ln[1/(1 - P)]\}$ vs. $\ln N$, as shown in Figure 4.26 for the single-sized pore model and Figure 4.27 for the multi-sized pore model, the slope was m and the intercept with the ordinate was $-mlnk$. All the m and k for single-sized pore model and the multi-sized pore model are listed in Table 4.4 and 4.5, respectively.

With the known m and k at each stress level, the fatigue initiation probability can be calculated by the two-parameter Weibull function, Eq. 4.8, as Figure 4.28 and Figure 4.29 shown. In both plots of fatigue initiation probability, the incubation life was increased with decrease of the stress level if the initiation probability, P (or probability of survival, $P_s = 1 - P$) was same. For the multi-sized pore model, when the initiation probability P was 0.1%, namely, 99.9% survival rate for crack initiation P_s , the incubation life at 110% yield strength was 9 cycles and 1,413 cycles at 50% yield strength. It demonstrated that a crack with 99.9% probability would not be initiated from a pore in 9 cycles at 110% σ_y , while a crack 99.9% probability would not be initiated in 1,413 cycles at 50% σ_y . After experiencing a specific number of cyclic loading, the probability of initiation was increased with the increase of stress level, on the contrary, the survival rate for initiation was decreased. For instance, in the multi-sized pore model, after 10,000 times cyclic lading, at highest stress level, the probability of initiation was highest and the survival rate for crack initiation was lowest, i.e., P was 29.4% and the P_s was only 71.6% at 110% σ_y ; at lowest stress level 50% σ_y , the P was lowest with only 1.23% but P_s was highest with 98.87%. The above-mentioned probabilistic analysis was used for quantify the reliability of fatigue crack initiation, which is significant for understanding the stochastic behaviors of fatigue crack nucleation and can consequently be used in the estimation of material properties which includes microstructural variability in the A713 cast Al alloy.

4.10 The Fatigue Reliability of Failure

The mean value of the fatigue incubation life in the multi-sized pore model in Figure 4.22 was plotted together with the experimentally measured total failure life against the stress level, as shown in Figure 4.30. It can be seen that those two curves are almost parallel to each other after taking logarithm. Therefore, an assumption can be made to calculate the fatigue reliability of failure, which is assuming that the crack propagation life equals the experimentally measured total life minus the mean value of the incubation life. The calculated propagation life varies with the applied stress level. Next step is to add the propagation lives to the incubation lives of all of cracks in the multi-sized pore model. A total fatigue life distribution can subsequently be obtained. The fatigue reliability of failure can be predicted using above-mentioned method. The cumulative probabilities for fatigue total life distribution at different maximum applied cyclic stress in the multi-sized model have been shown in Figure 4.31. The linear plots of $\ln\{\ln[1/(1 - P)]\}$ vs. $\ln N$ is shown in Figure 4.32 and the parameters are listed in table 4.6. The reliability of fatigue failure can be seen in Figure 4.33. This method for fatigue failure reliability will be more practical if the fatigue crack propagation life can be more accurate.

4.11 Conclusions

- 1) The quantitative 3-D pore-sensitive model developed in this work took into account the 3-D effects of pores on fatigue crack initiation, and was capable of quantification of fatigue weak-link density and strength distribution in A713 Al cast alloys. It was validated by the experimentally measured fatigue weak-link density and strength distribution in A713 Al alloys.
- 2) The model also demonstrated that the crack initiation rate at pores in surface was a Weibull function of the applied cyclic stress, which was consistent with the experimental results.
- 3) With increase in number density of pores, the crack population was increased, but crack initiation rate remained unchanged. The crack initiation rate was increased with increase of pore size (same area fraction of 2.826%) in the model, though the number density was lowered due to larger pore sizes.
- 4) The density and strength distribution of fatigue weak-links could be determined by fitting the curve of the crack initiation rate vs stress using a Weibull function. These results were simulated using both single- and multi-sized pores in the model, respectively, with the multi-sized pores giving rise to more consistent results with the experimentally measured ones. The difference in the peak value of the strength distribution of fatigue weak-links between

the simulated and the experimental results was reduced from 20% using the single-sized pores to 1.8% by multi-sized pores.

- 5) The model developed in this work was also used to simulate the stochastic behaviors of multi-site crack nucleation by predicting the crack incubation lives at detrimental pores in the A713 cast Al alloy.
- 6) The crack initiation life was increased with decrease in cyclic stress, e.g., at a maximum cyclic stress just above the fatigue limit (70% yield strength), it could be over 96% the total fatigue life, compared to 69% at 110% yield strength.
- 7) The larger scatter was predicted in incubation life spectra at higher applied stress.
- 8) The reliability of fatigue crack initiation was quantified using the model at each applied cyclic stress in an A713 cast Al alloy. The probability of fatigue crack initiation was characterized by a two-parameter Weibull function, i.e., with 10,000 cyclic loading, the survival probability for crack initiation was 72% at 110% yield strength, and was 99% at 50% yield strength.

Table 4.1 The porosities used in the single-sized model

Area fraction	Volume fraction	Volume number density (15 μm in diameter)
2.826%	2.826%	16000 per mm^3

Table 4.2 The porosities used in the multi-sized model

Area fraction	Volume fraction	Volume number density (per mm^3)	15 μm	50 μm	100 μm
2.826%	2.826%	3567	3283	276	8

Table 4.3 Parameters used in Eq. 4.4

	σ_0 ($\% \sigma_y$)	R_0	m	k
Experimental	66.9%	0.048	4.28577	1.54276
Simulated (Single-sized pore)	66.9%	0.048	3.19242	1.80728
Simulated (Multi-sized pore)	66.9%	0.048	4.67211	1.83955

Table 4.4 Two-parameter Weibull analysis on the fatigue incubation life in the single-sized pore model

Stress level (%)	k	m	Adj. R²
75	-	-	-
80	5.42524	36.61199	0.89297
85	5.211312	23.62419	0.9717
90	5.025541	17.10725	0.99157
95	4.799146	12.5309	0.91101
100	4.632991	9.58791	0.98947
110	7.98807	4.402363	0.97745

Table 4.5 Two-parameter Weibull analysis on the fatigue incubation life in the multi-sized pore model

Stress level (%)	k	m	Adj. R²
50	361786.3765	1.23614	0.98753
60	284342.3	1.15942	0.89822
70	301429	0.98908	0.88743
80	206415.5	0.88901	0.89833
90	112570.4	0.8502	0.94356
100	69151.82	0.8316	0.92365
110	36694	0.82558	0.93039

Table 4.6 Two-parameter Weibull analysis results on the fatigue total life in the multi-sized pore model

Stress level (%)	k	m	Adj. R²
50	188844.8	3.80708	0.95024
60	316178.2	4.0942	0.81827
70	514420.4	4.32259	0.85268
80	843201.9	4.81441	0.93201
90	1286842	4.33371	0.95305
100	2059442	7.88414	0.95132
110	3296560	18.18222	0.96792

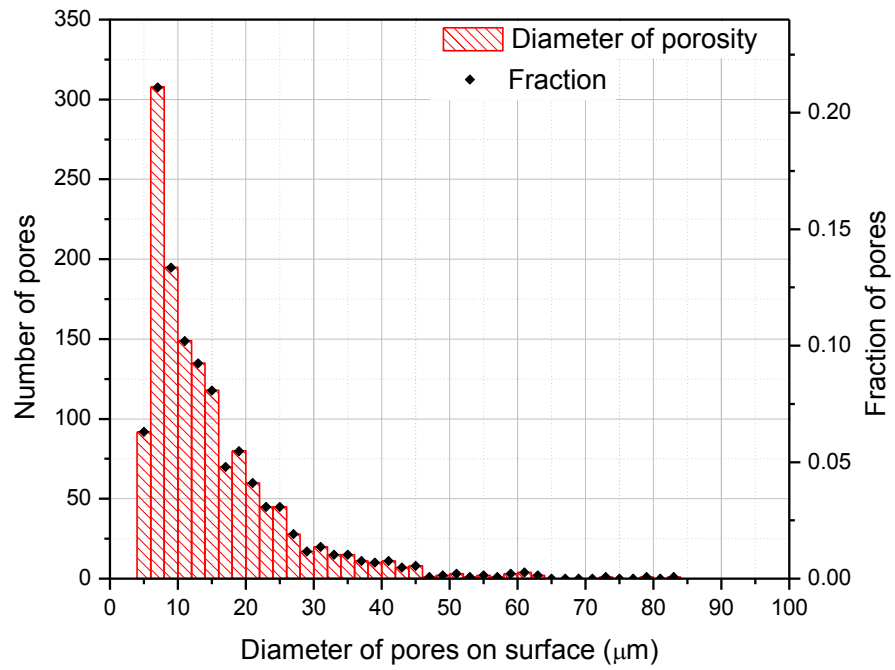
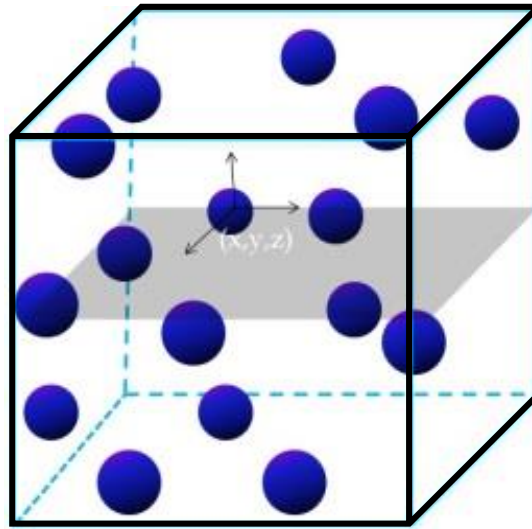


Figure 4.1 Experimentally measured pore size distribution in A713 cast Al alloys.

(a)



(b)

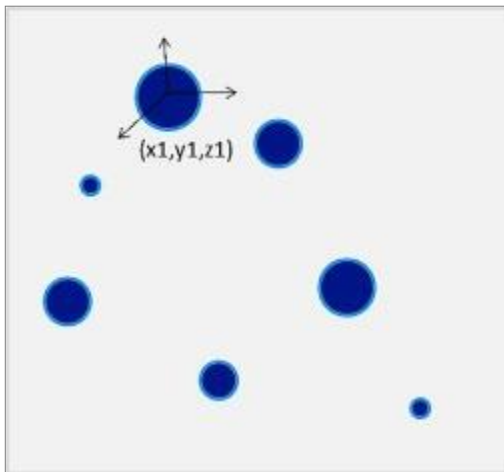


Figure 4.2 A 3-D pore-sensitive model. (a) the schematic of the reconstructed 3-D digital pore structure by randomly distributing spherical pores in a cube; (b) a simulated sample surface by randomly cross-sectioning the digital pore structure.

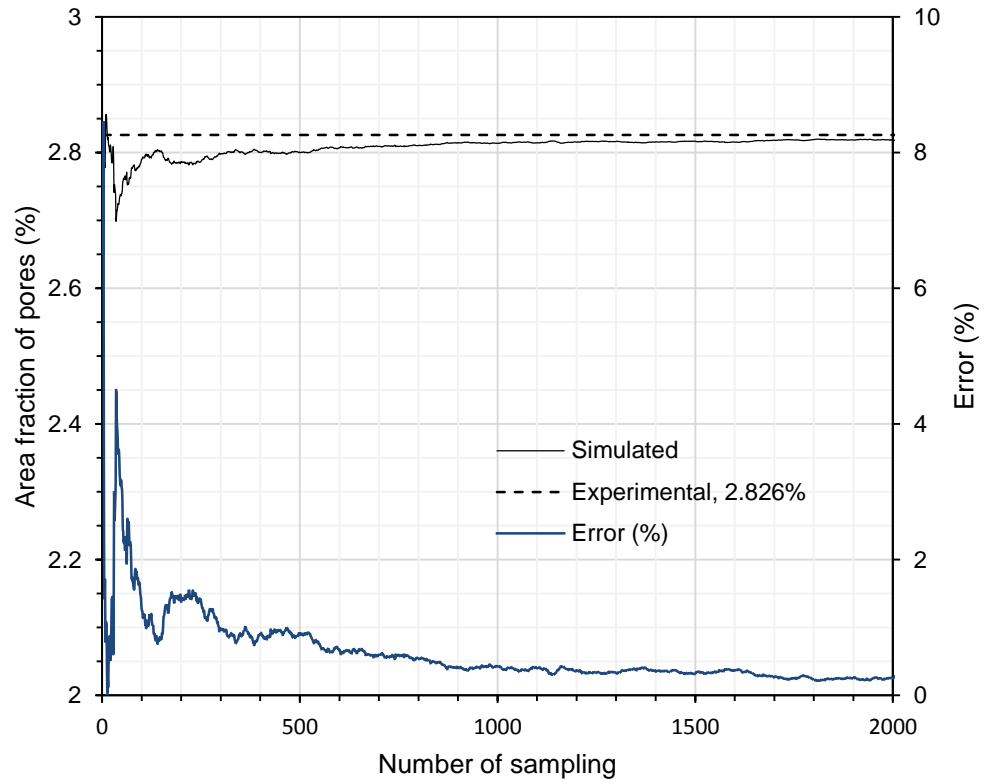


Figure 4.3 Verification of the statistical stability of the model by calculating the average area fraction of the pores on the simulated surface as a function of sampling number.

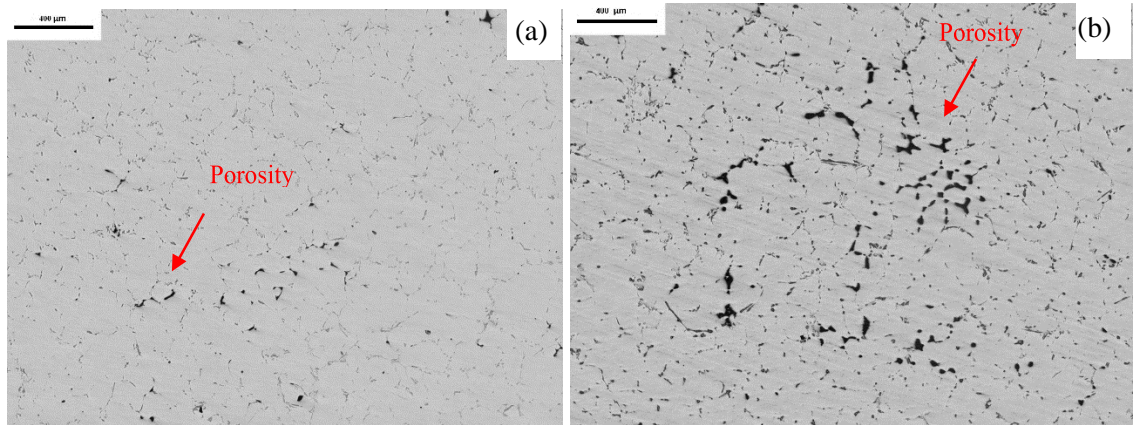


Figure 4.4 The porosity morphology in A713 cast Al alloys with (a) low pore density and (b) high pore density [55].

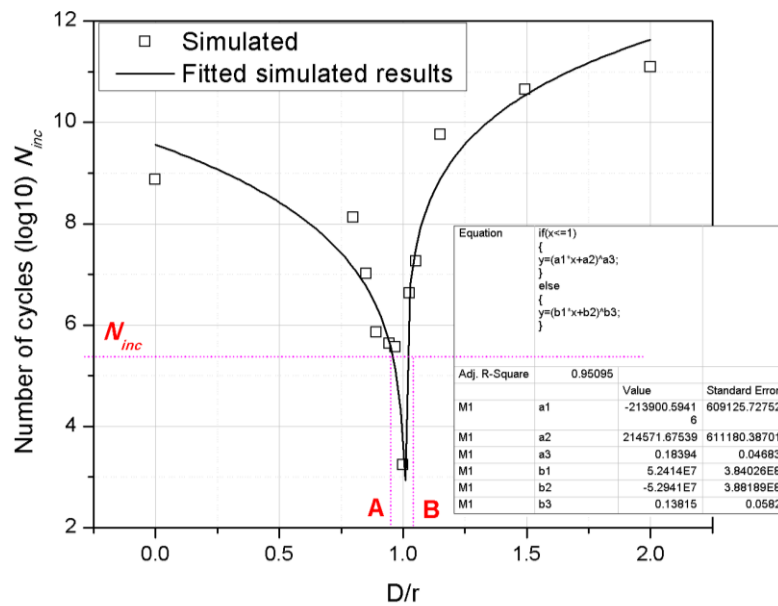


Figure 4.5 The range in pore depth between A and B used to determine crack incubation at pores in surface under the maximum cyclic stress of $100\%\sigma_y$.

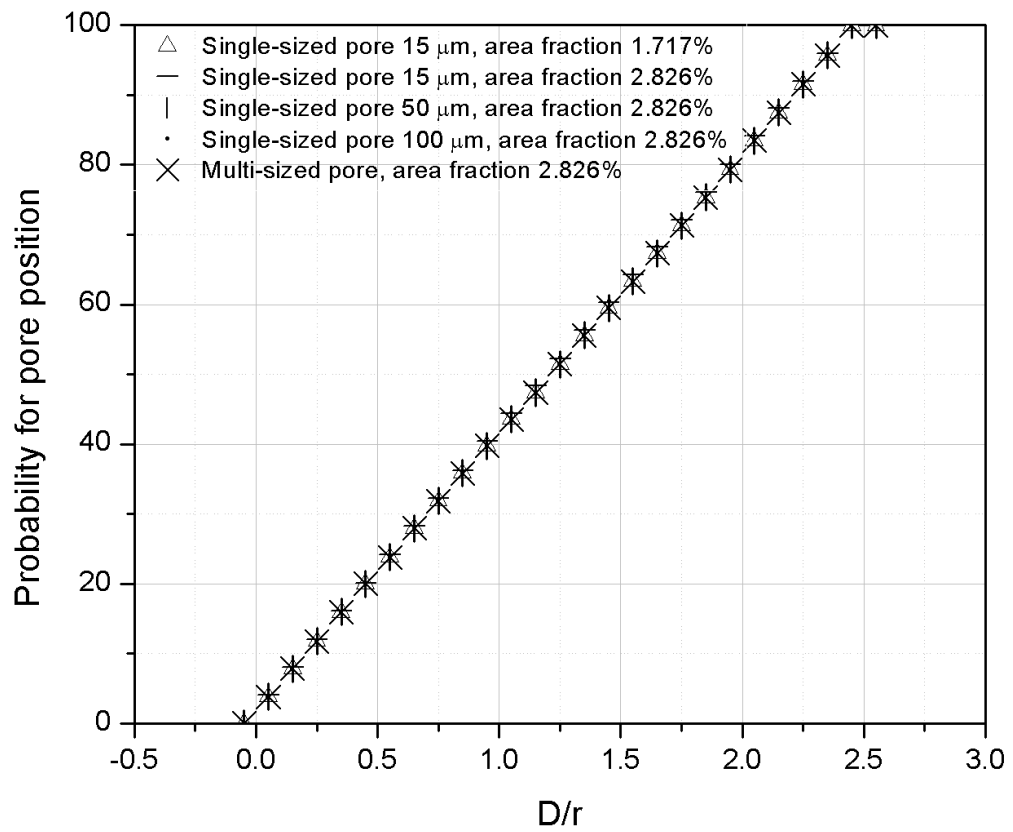


Figure 4.6 The probability for pore position distribution with number density and pore size in single-sized pore model and multi-sized pore model.

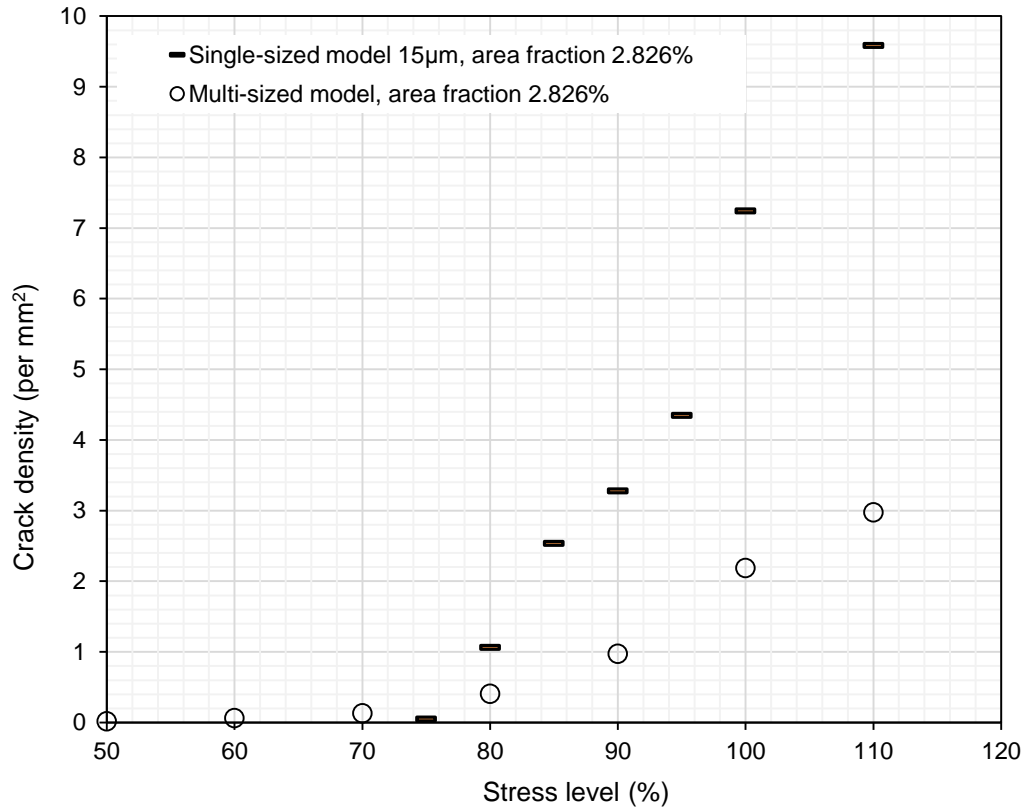


Figure 4.7 The crack density vs applied stress in single-sized pore model and multi-sized pore model.

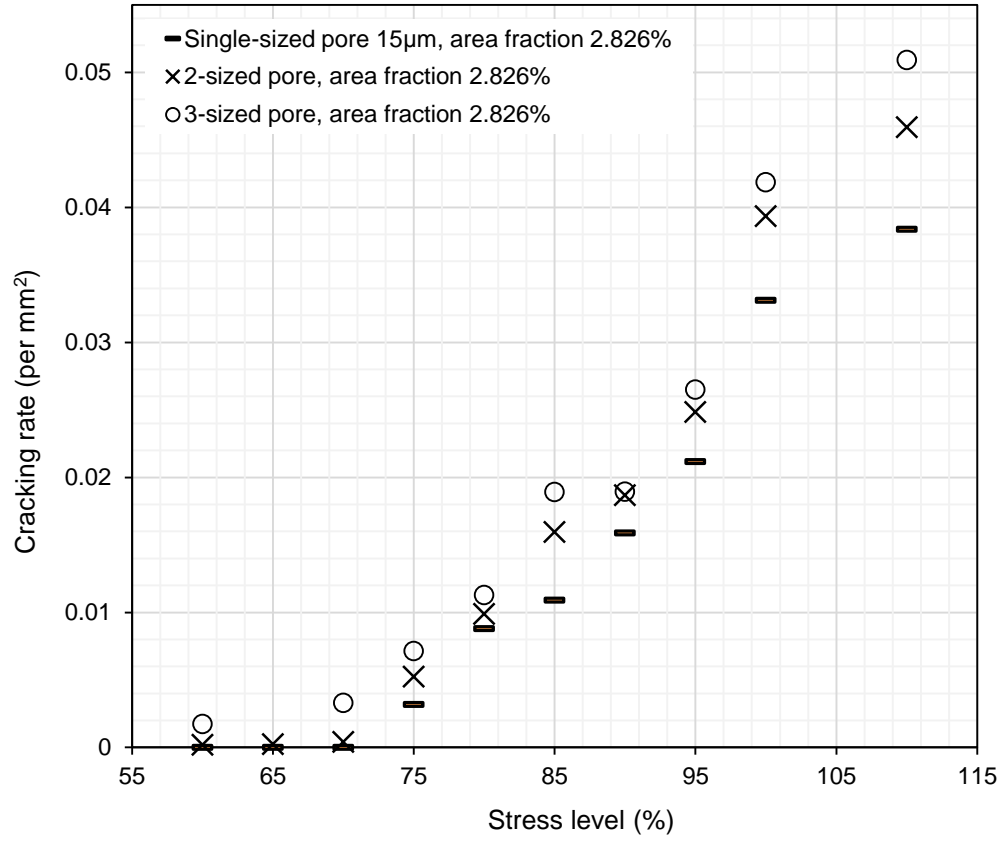


Figure 4.8 The rate of crack initiation vs applied stress in single-sized, 2-sized and 3-sized models.

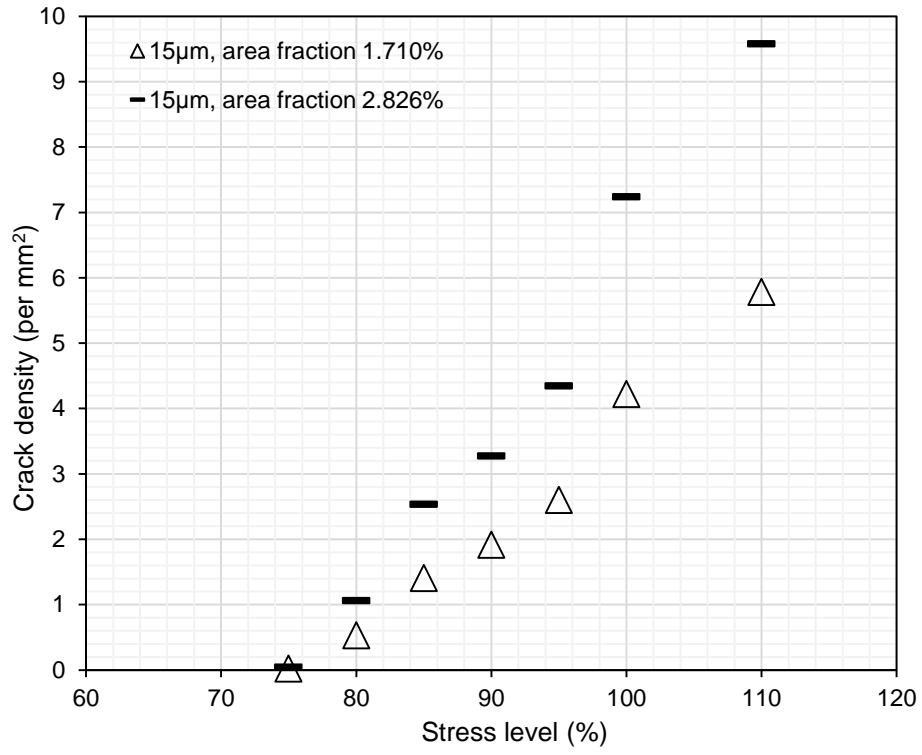


Figure 4.9 The effects of number density on the crack density.

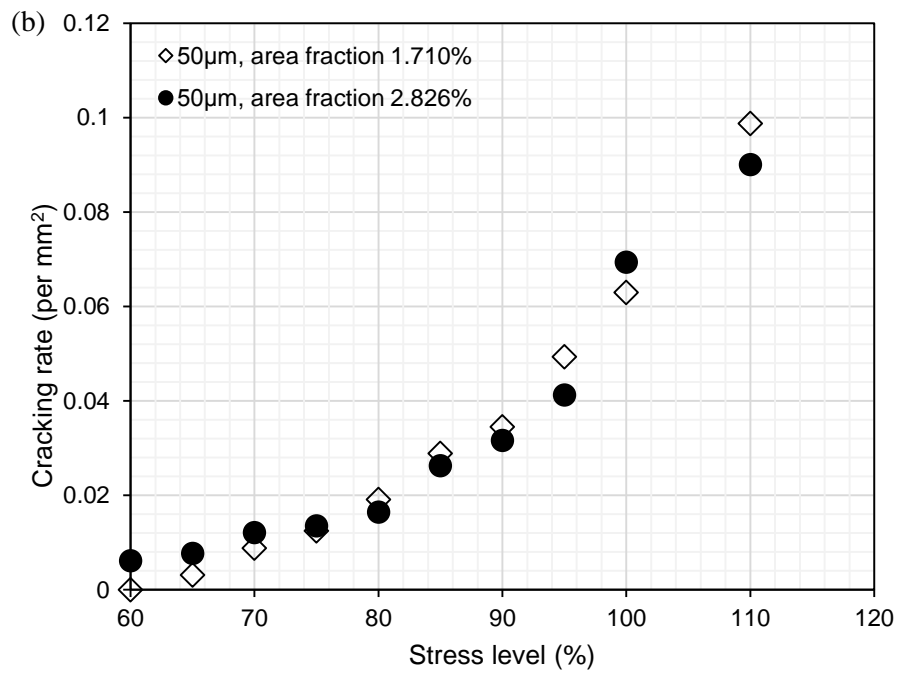
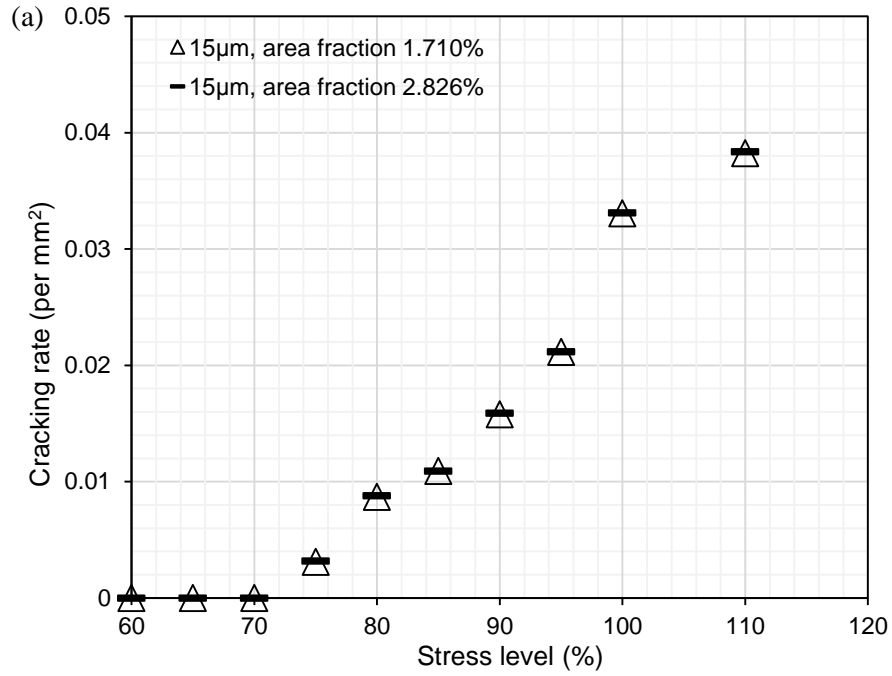


Figure 4.10 The effects of number density on the rate of crack initiation in single-sized pore model, (a) 15 µm pore; (b) 50µm pore.

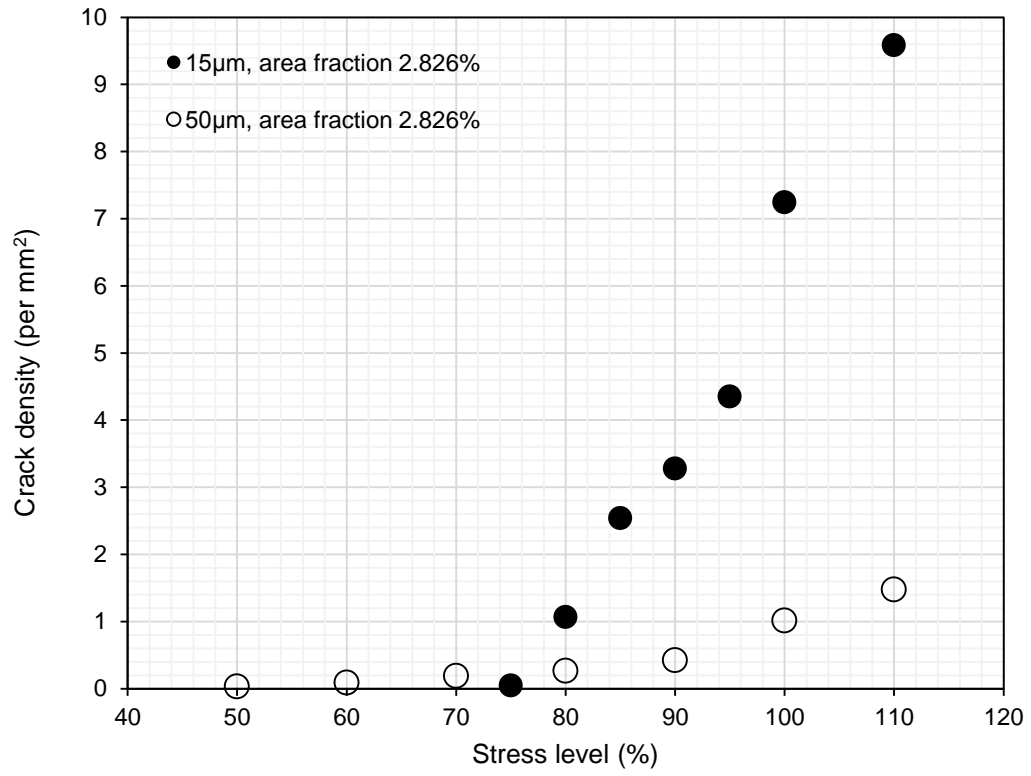


Figure 4.11 The effects of pore size on crack density.

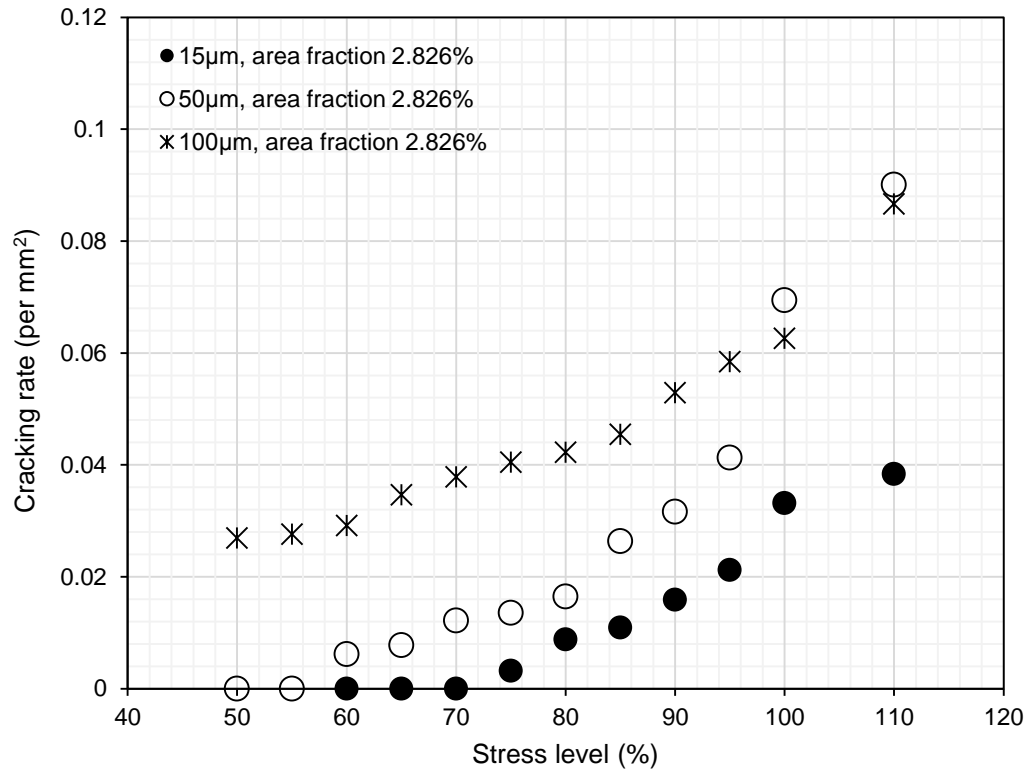


Figure 4.12 The effects of pore size on the rate of crack initiation.

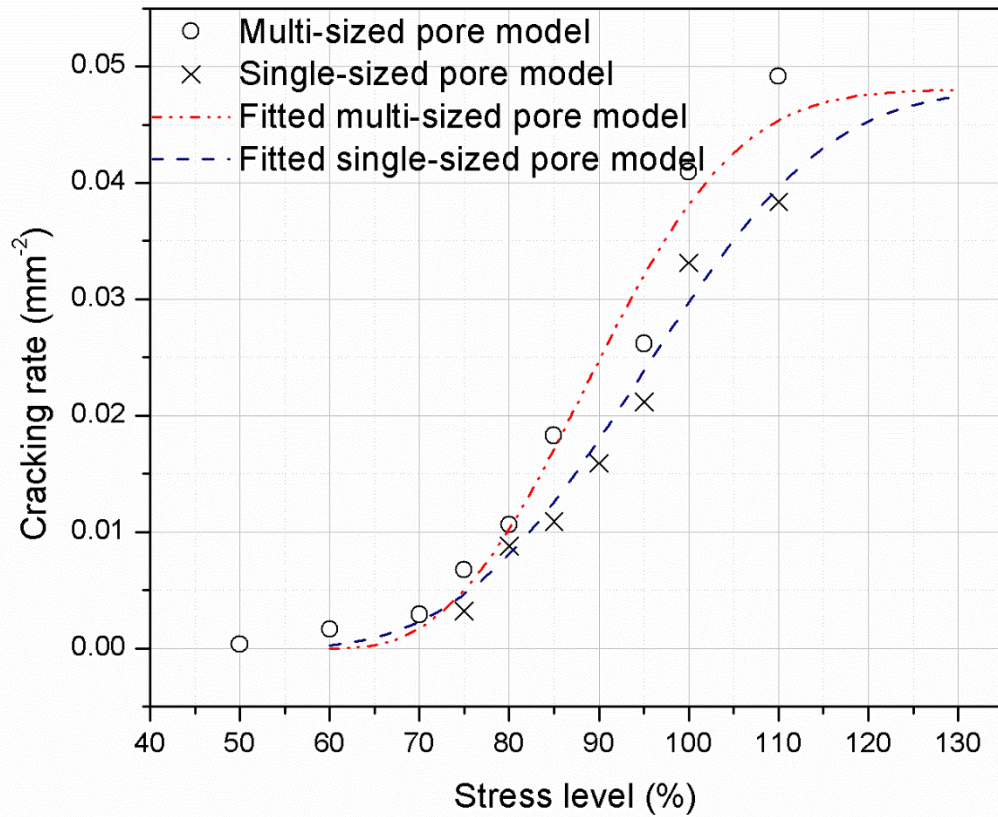


Figure 4.13 Simulated rates of fatigue crack initiation at pores in single-sized and multi-sized pore model, respectively, with a pore area fraction of 2.826%, at different maximum cyclic stresses.

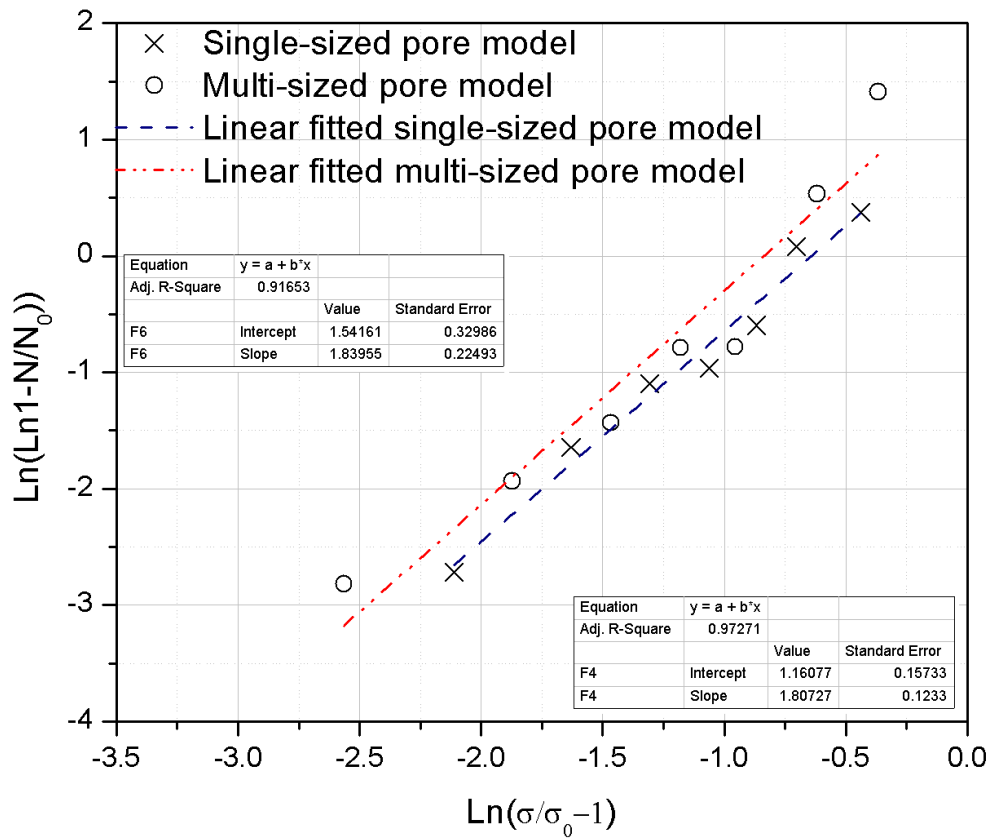


Figure 4.14 Plots of $\ln\left(-\ln\left(1 - \frac{R}{R_0}\right)\right)$ vs $\ln\left(\frac{\sigma}{\sigma_0} - 1\right)$ of simulated fatigue weaklinks at pores in single-sized and multi-sized pore model.

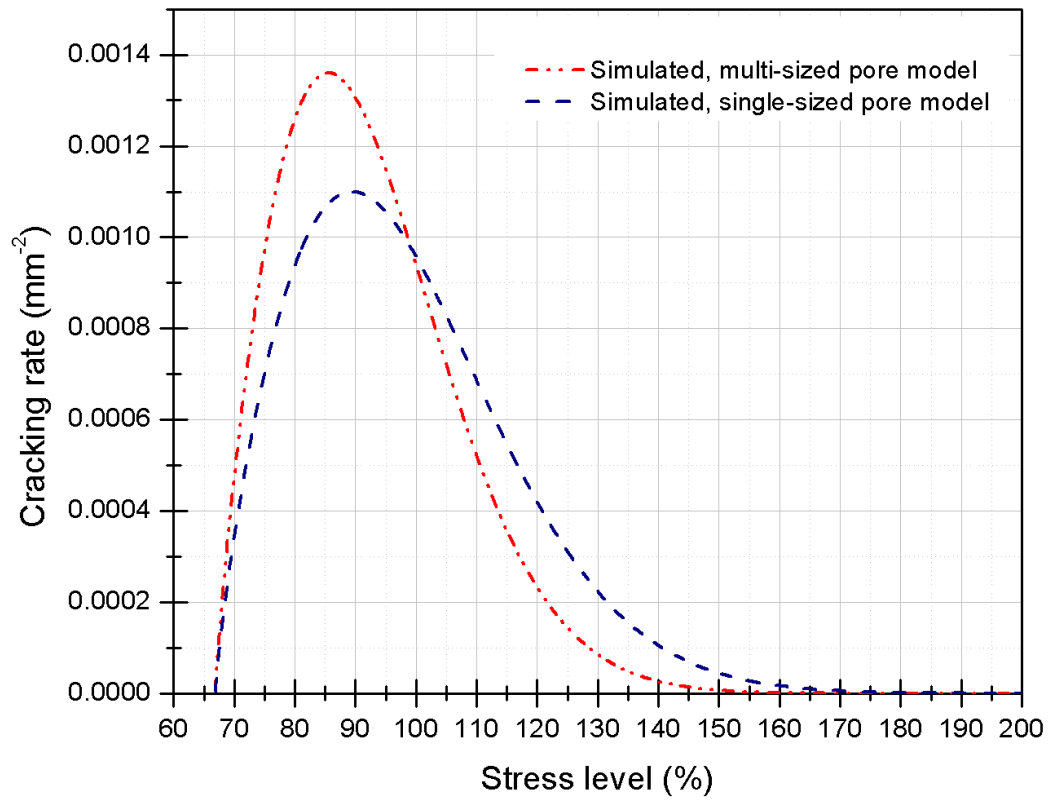


Figure 4.15 Simulated strength distributions of the fatigue weaklinks in single-sized and multi-sized pore model.

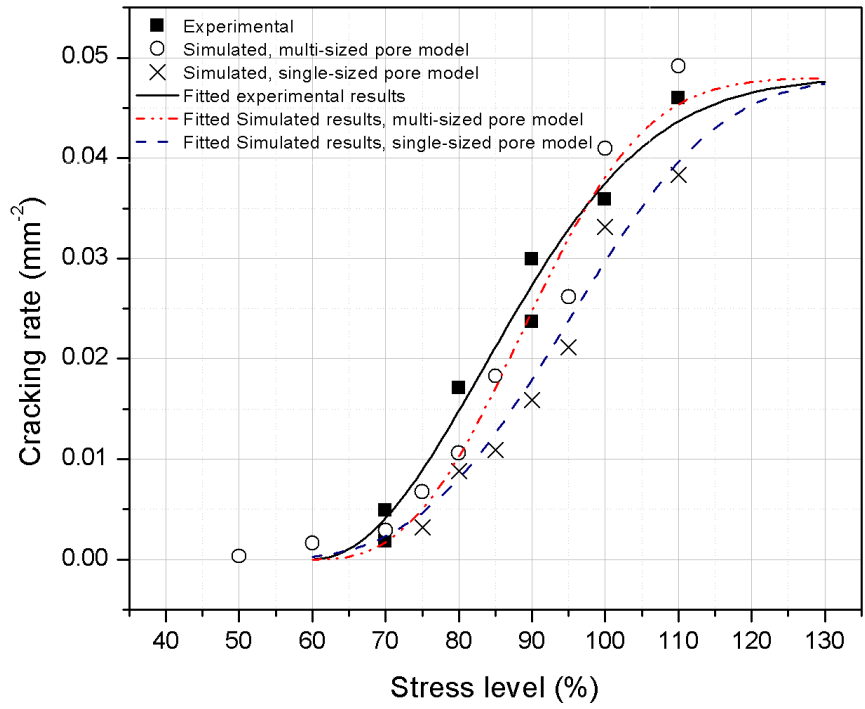


Figure 4.16 Simulated rates of fatigue crack initiation at pores with an area fraction of 2.826%, in single-sized and multi-sized pore model, respectively, as compared to the experimental result with a pore area fraction of 2.826%, at different maximum cyclic stresses in the A713 Al alloy.

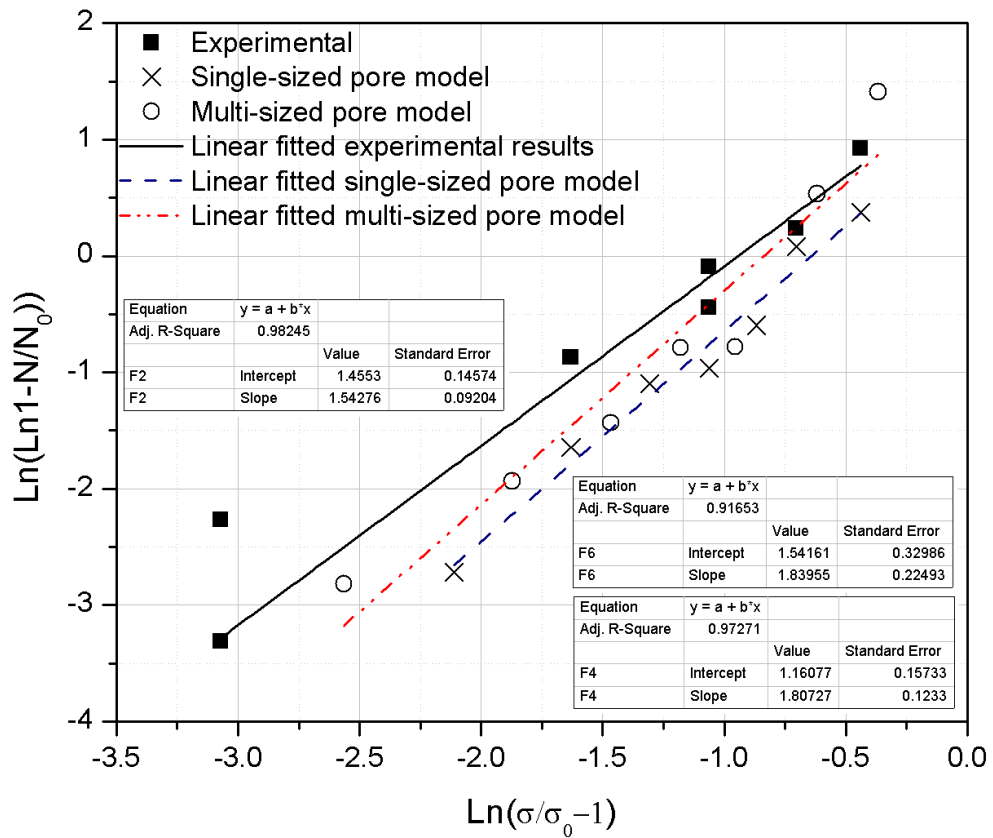


Figure 4.17 Plots of $\ln\left(-\ln\left(1 - \frac{R}{R_0}\right)\right)$ vs $\ln\left(\frac{\sigma}{\sigma_0} - 1\right)$ of experimental in the A713 Al alloy and simulated fatigue weaklinks in single-sized and multi-sized pore model.

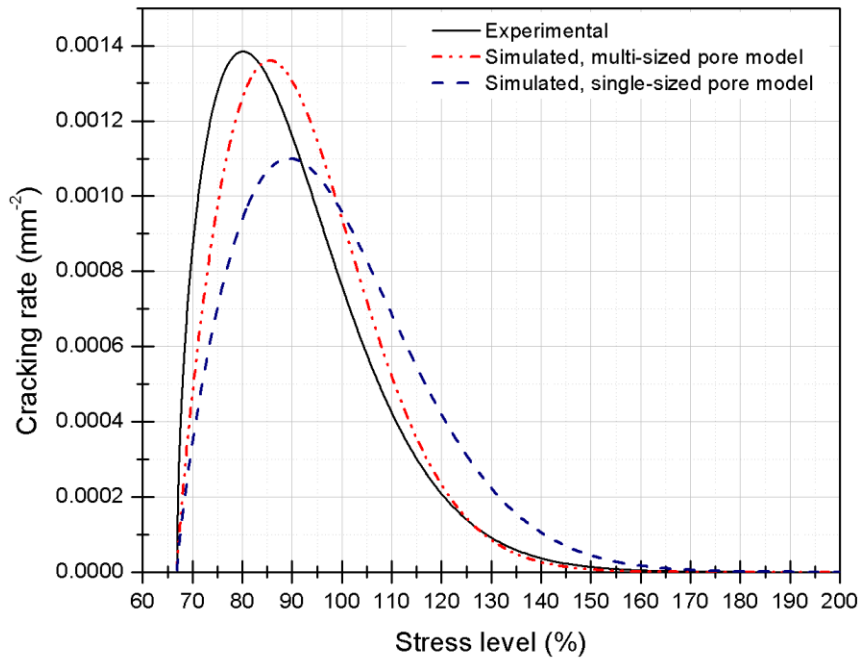


Figure 4.18 Experimental and simulated strength distributions of the fatigue weaklinks in the A713 Al alloy.

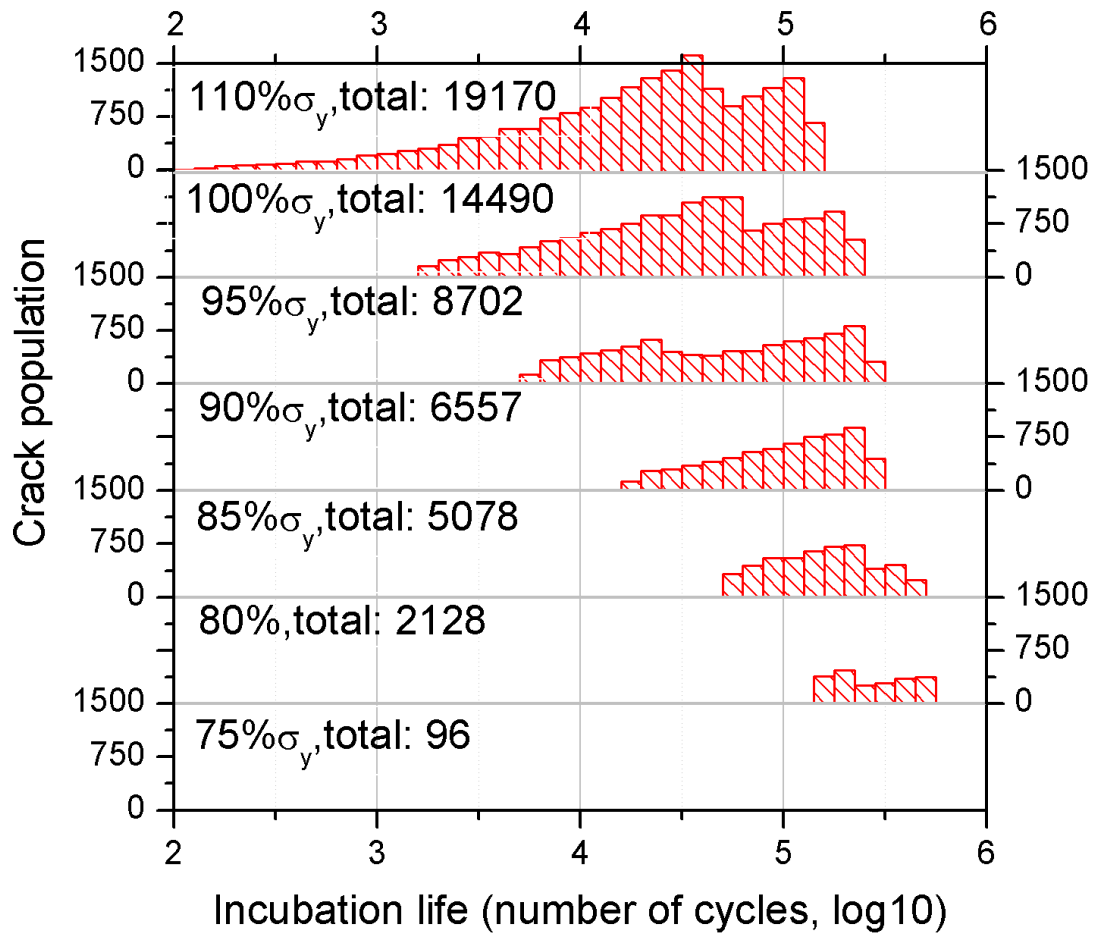


Figure 4.19 The prediction of fatigue crack incubation life distribution at pores in the single-sized pore model in the A713 Al alloy at each given applied maximum stress, the number of cracks vs the incubation life.

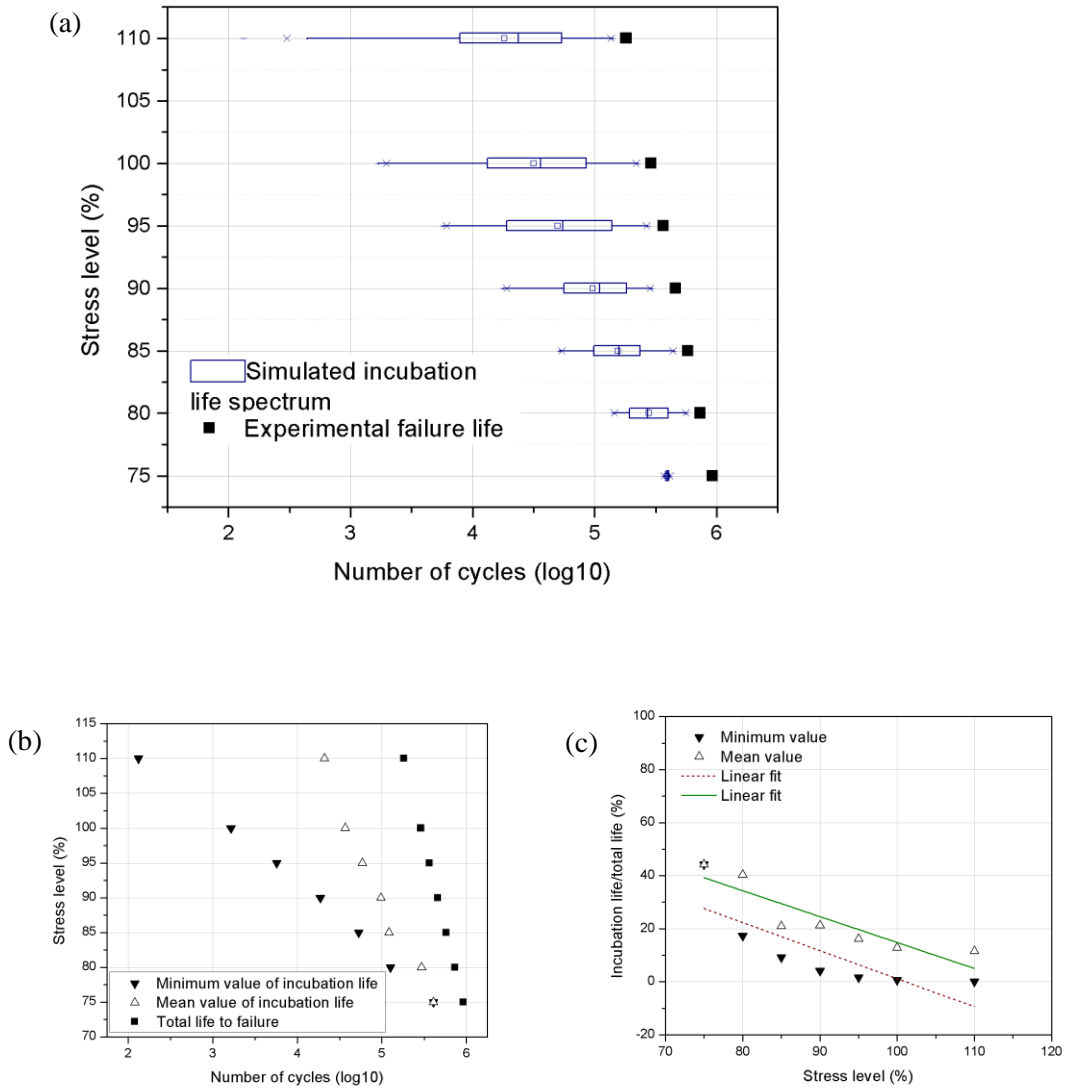


Figure 4.20 Simulated incubation life in the single-sized model, (a) comparison of stress vs. the total life to failure in experiments and the stress vs. the incubation life spectrum in simulations; (b) the minimum value, mean value and maximum value of incubation life distribution at different stresses; (c) the percentage of crack incubation life of the total life to failure vs. stress.

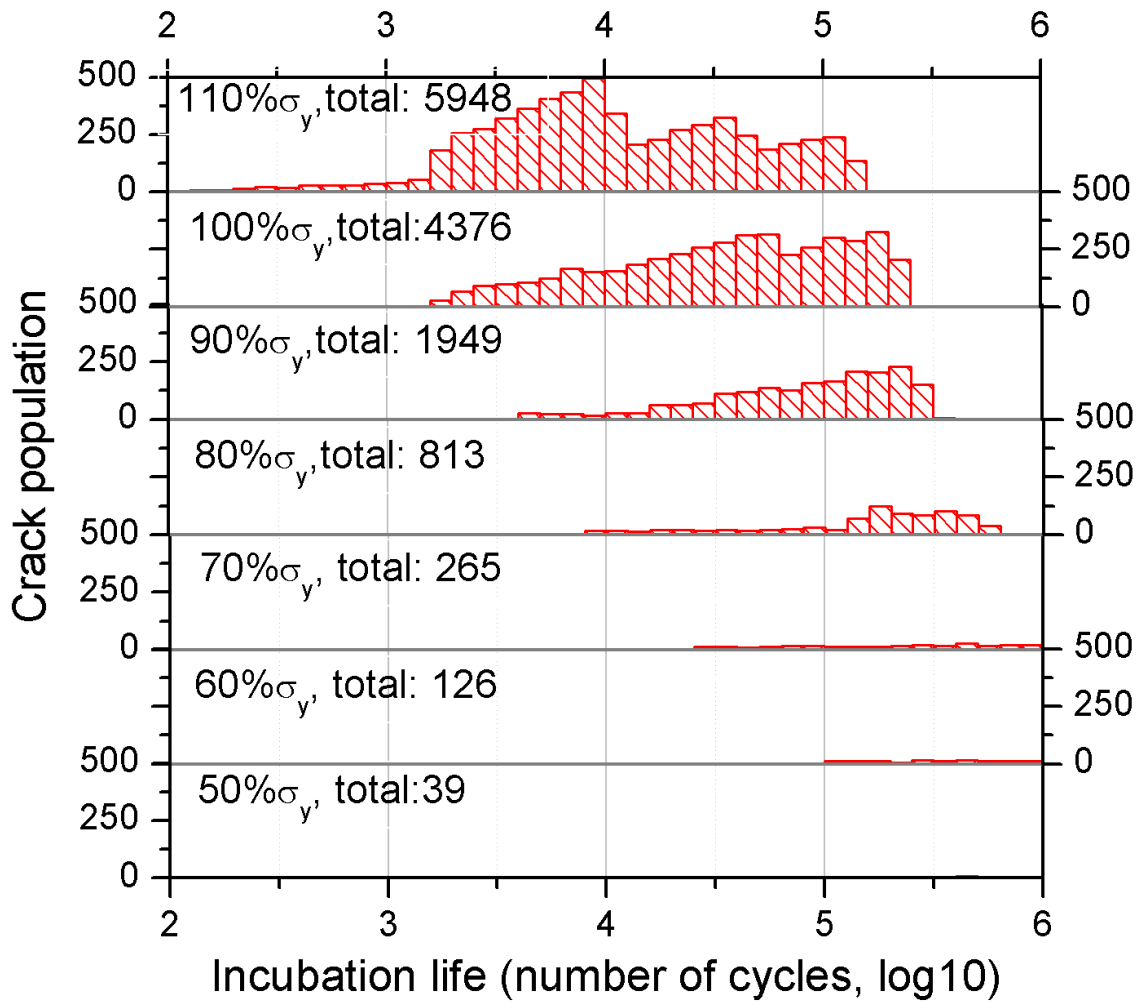


Figure 4.21 The prediction of fatigue crack incubation life distribution at pores in the multi-sized pore model in the A713 Al alloy at each given applied maximum stress, the number of cracks vs the incubation life.

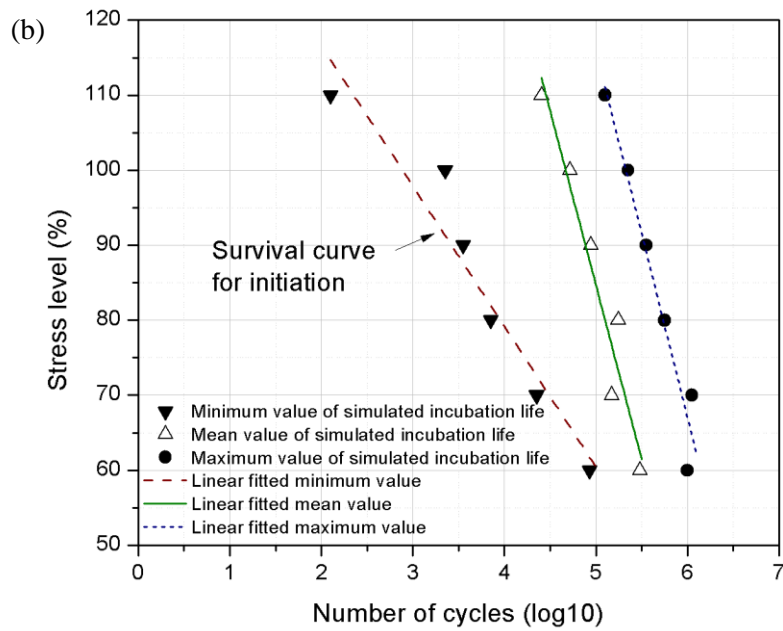
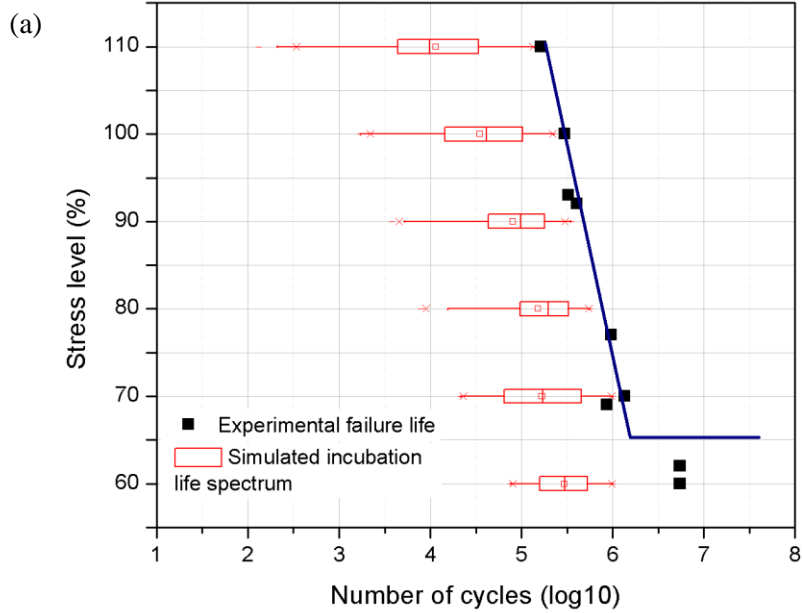


Figure 4.22 The simulated incubation life in the multi-sized pore model, (a) comparison of stress vs. the total life to failure in experiments and the stress vs. the incubation life spectrum in simulations; (b) the minimum value, mean value and maximum value of incubation life distribution at different stresses.

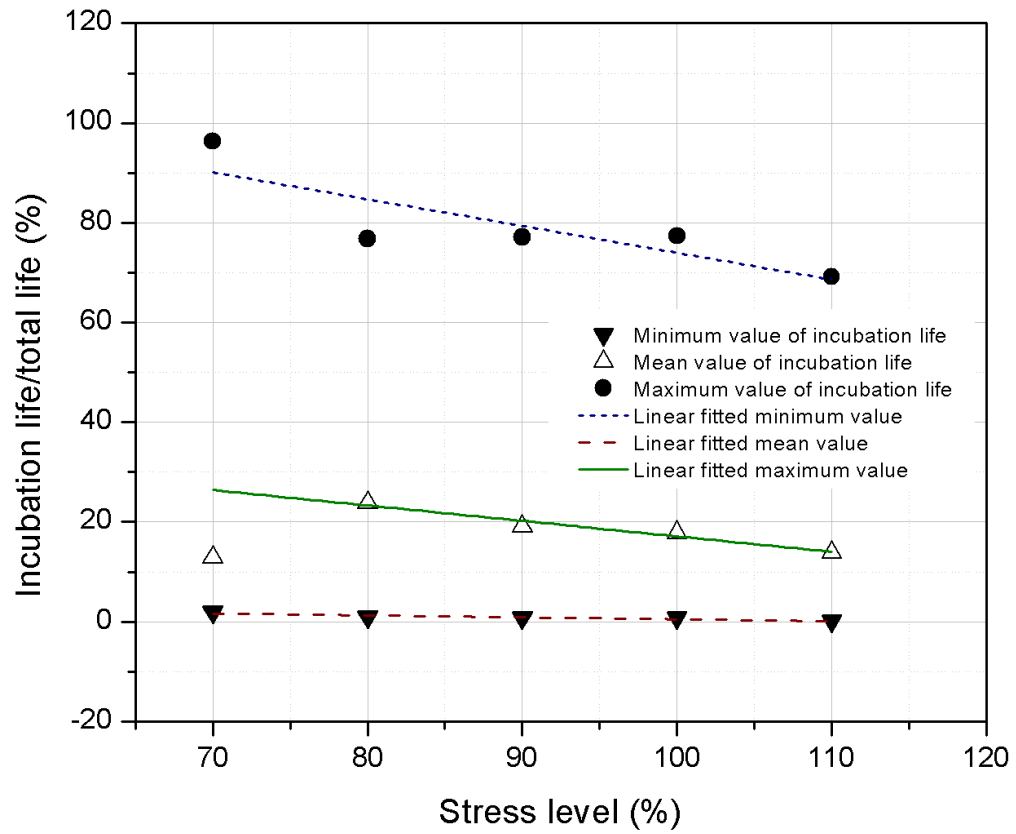


Figure 4.23 The percentage of crack incubation life of the total life to failure vs. stresses in the multi-sized pore model.

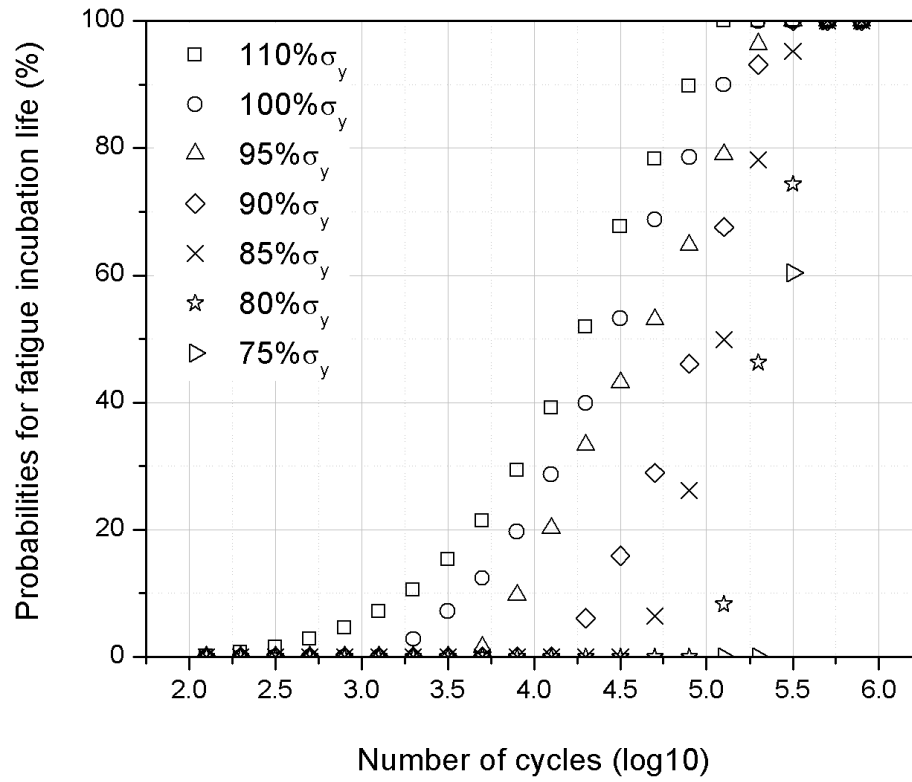


Figure 4.24 The cumulative probabilities for fatigue crack initiation life distribution at different maximum applied cyclic loading in the single-sized pore model.

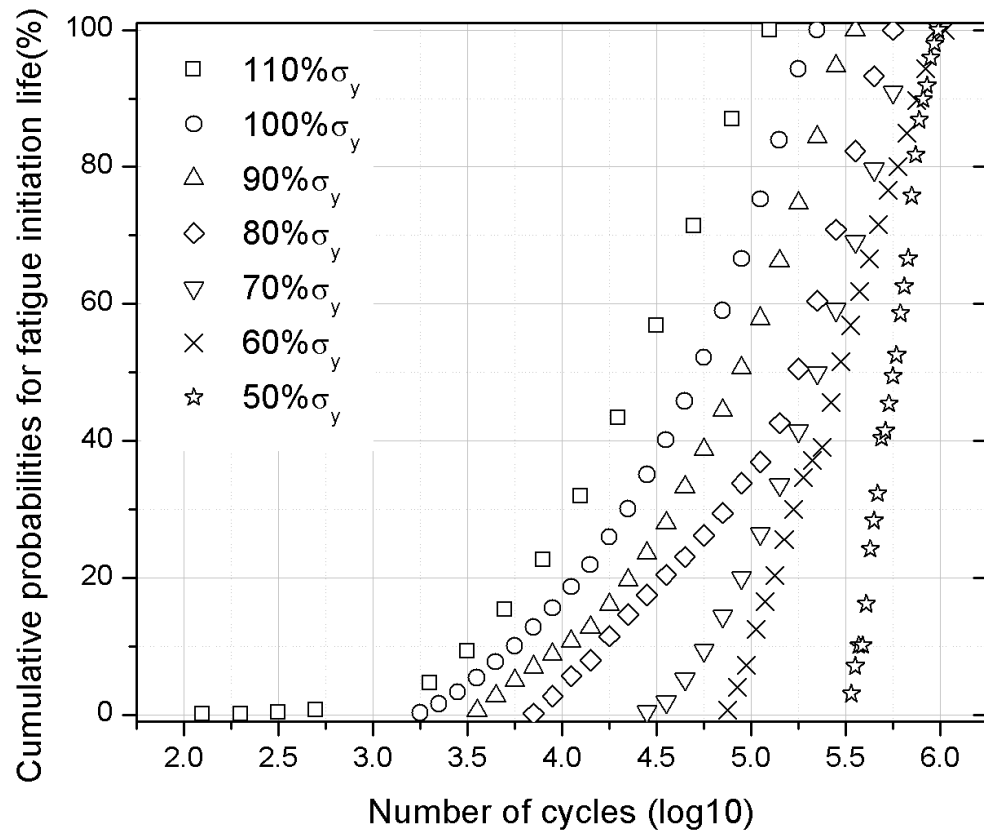


Figure 4.25 The cumulative probabilities for fatigue crack initiation life distribution at different maximum applied cyclic loading in the multi-sized pore model.

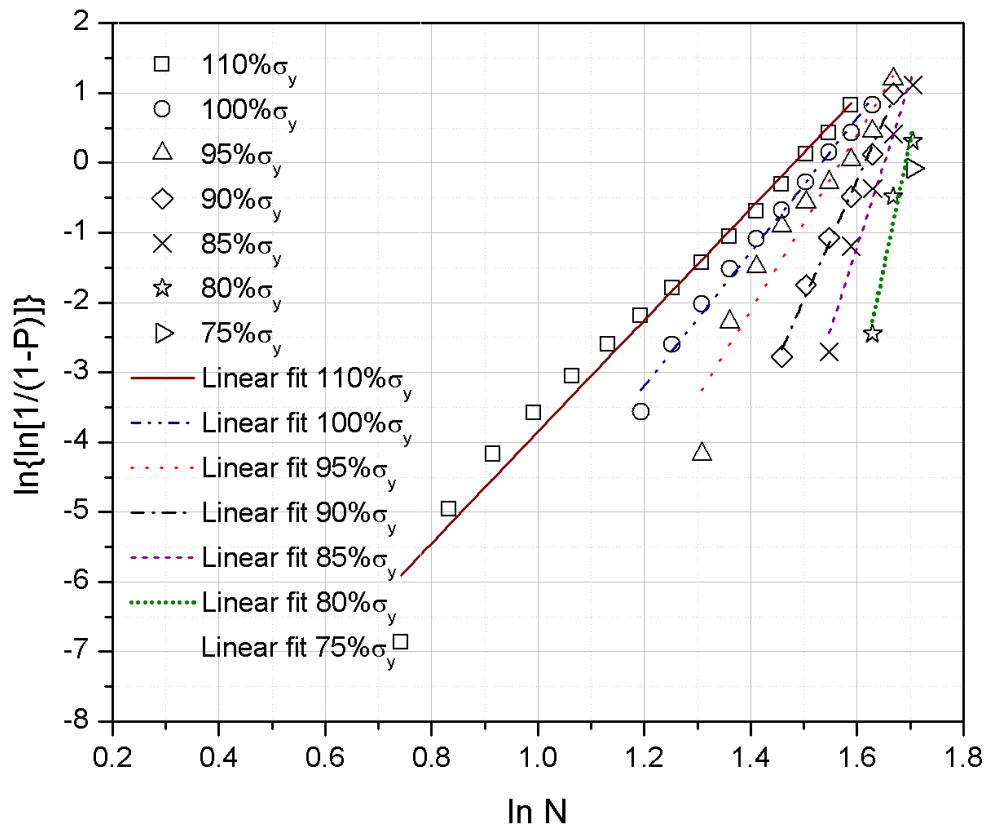


Figure 4.26 The linear plots of $\ln\{\ln[1/(1-P)]\}$ vs. $\ln N$ by a two-parameter Weibull analysis in the single-sized pore model.

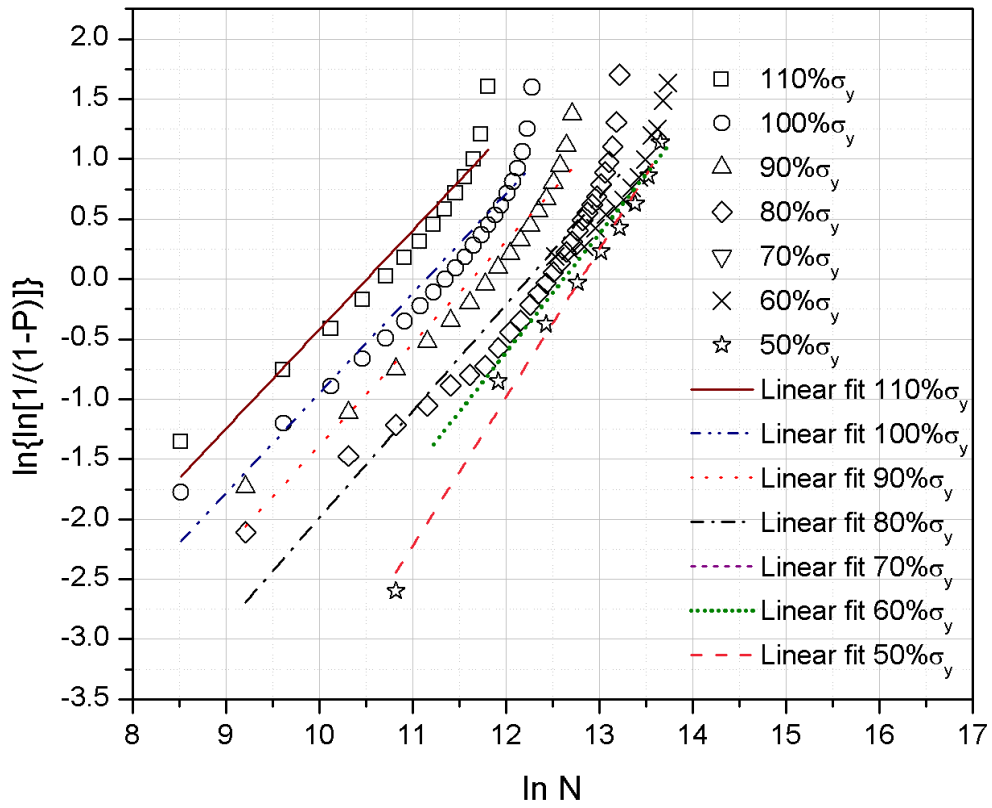


Figure 4.27 The linear plots of $\ln\{\ln[1/(1 - P)]\}$ vs. $\ln N$ by a two-parameter Weibull analysis in the multi-sized pore model.

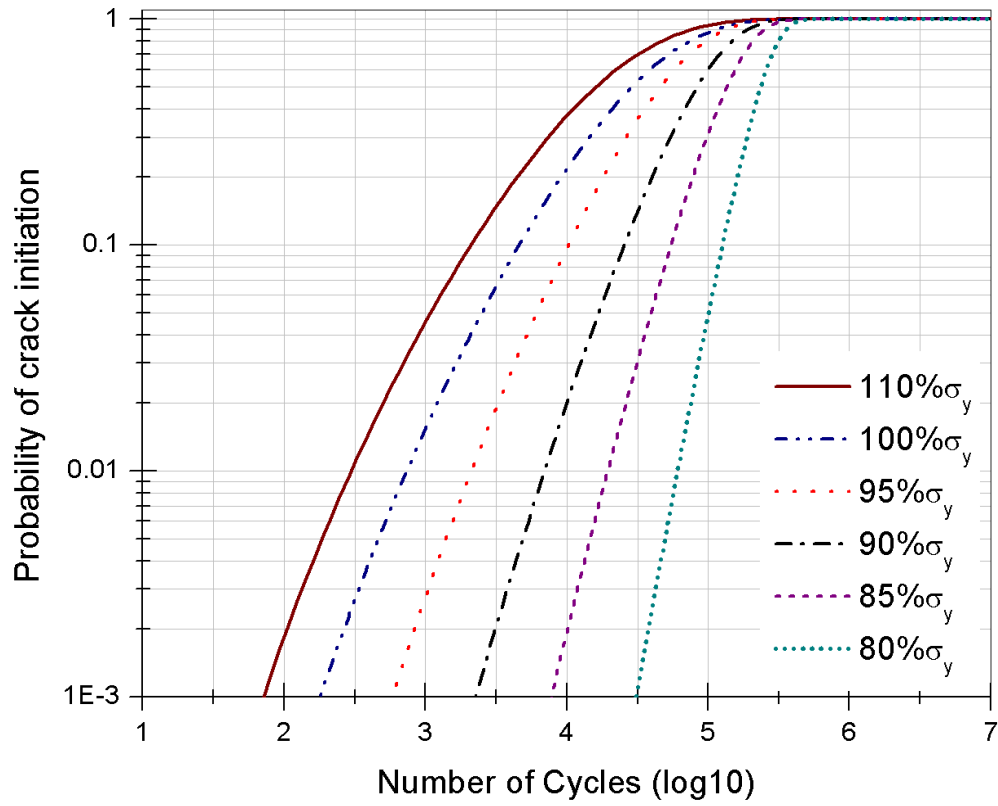


Figure 4.28 The probability of crack initiation at different applied maximum cyclic stresses in the single-sized pore model.

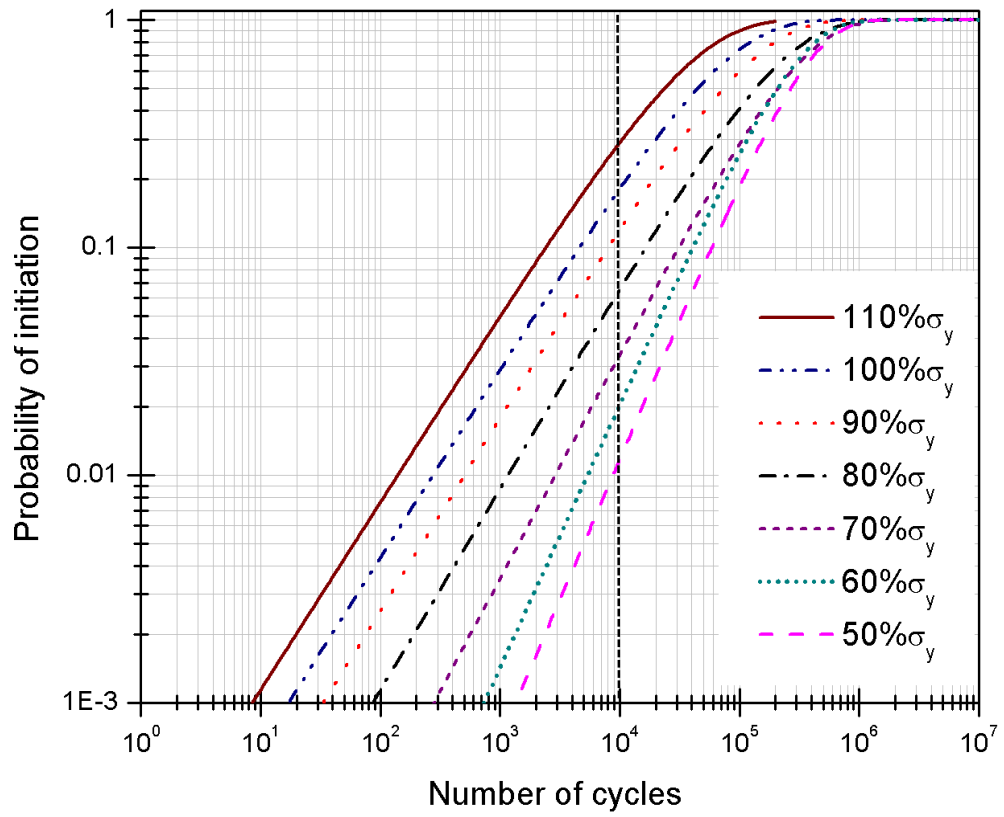


Figure 4.29 The probability of crack initiation at different applied maximum cyclic stresses in the multi-sized pore model.

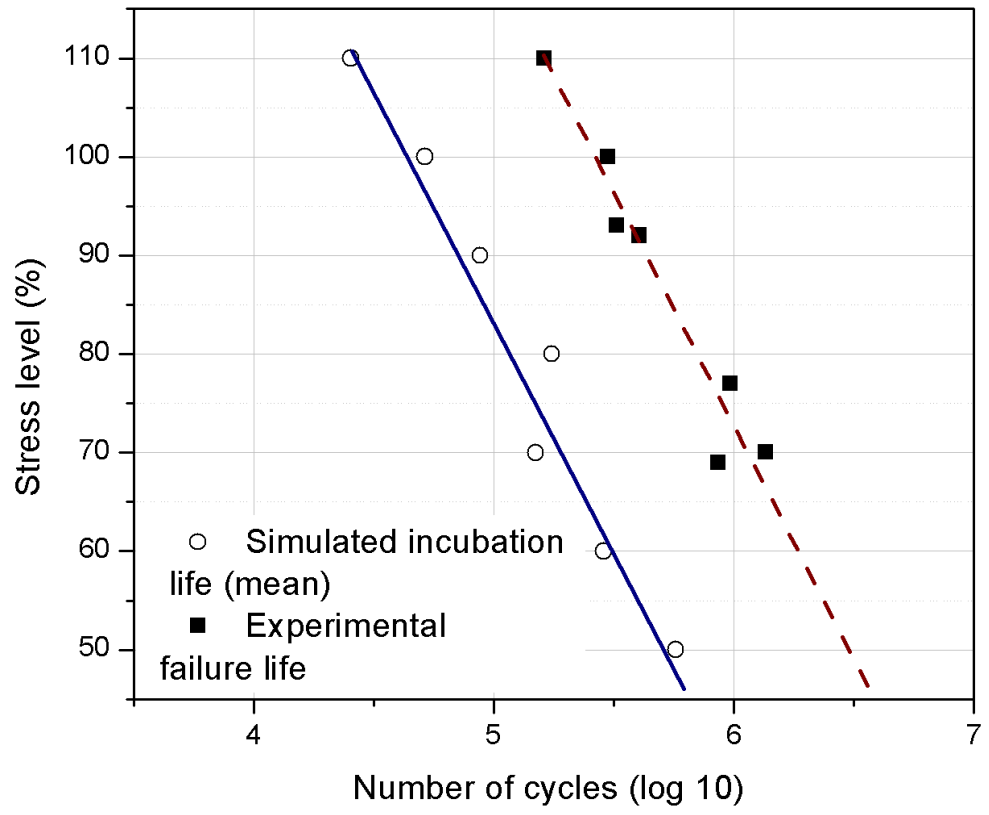


Figure 4.30 The mean value of the simulated incubation life and the experimentally measured failure life at different applied maximum cyclic stresses in the multi-sized pore model.

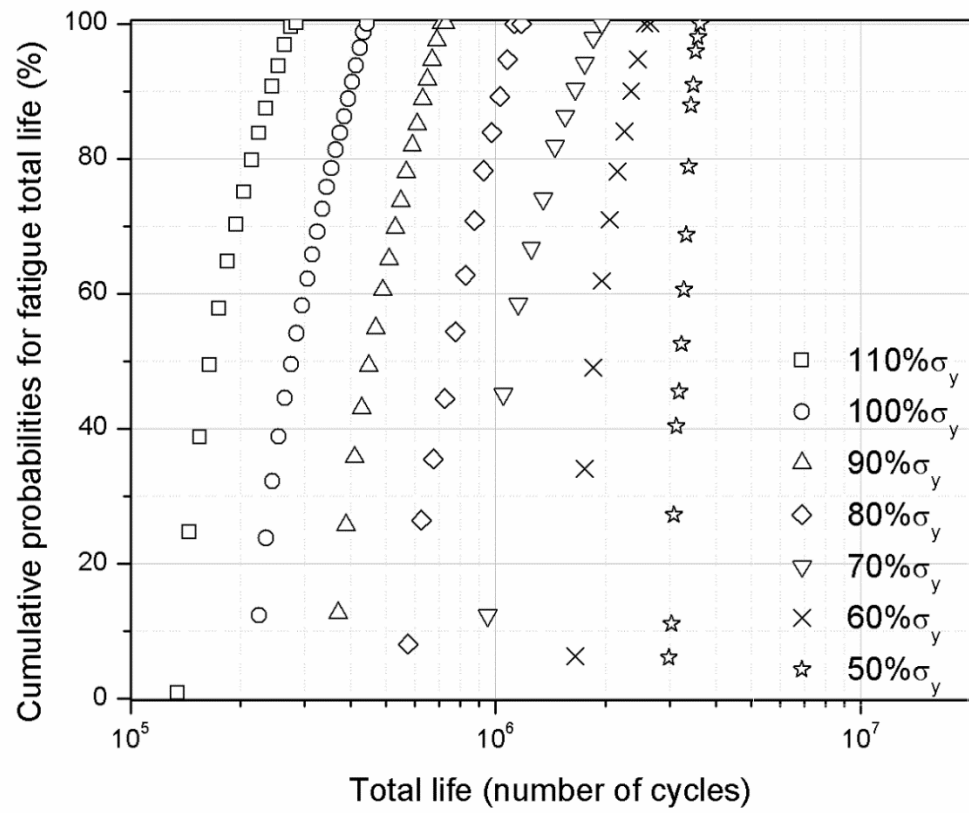


Figure 4.31 The cumulative probabilities for fatigue total life distribution at different maximum applied cyclic loading in the multi-sized pore model.

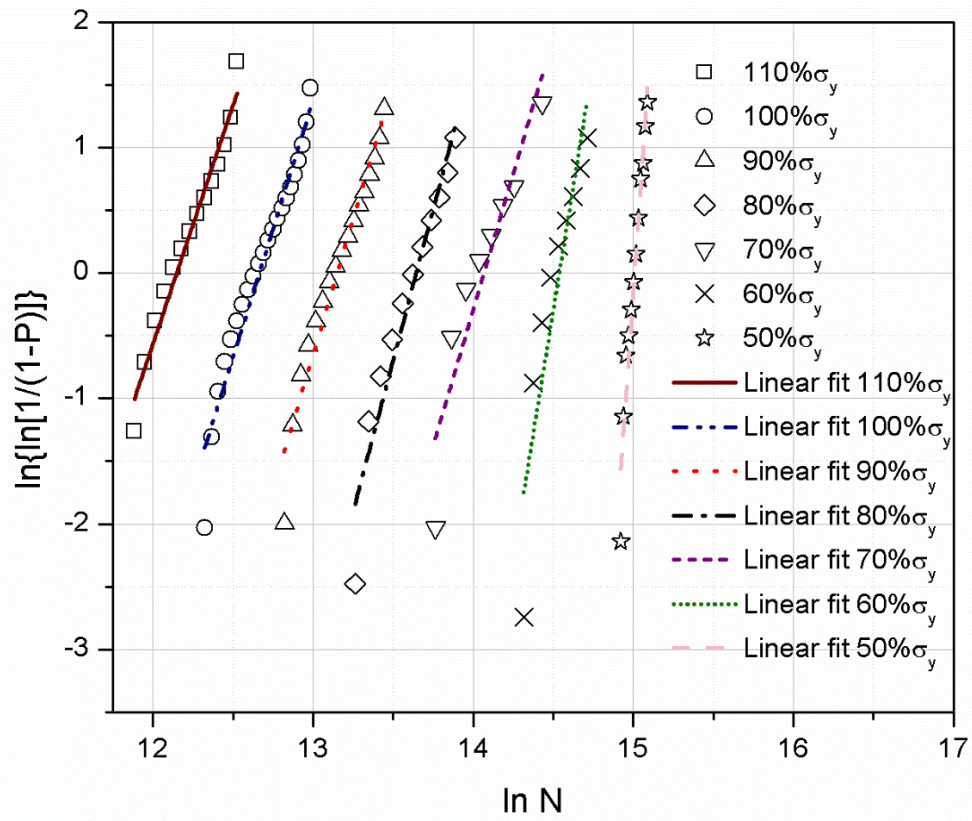


Figure 4.32 The linear plots of $\ln\{\ln[1/(1 - P)]\}$ vs. $\ln N$ by a two-parameter Weibull analysis in the multi-sized pore model.

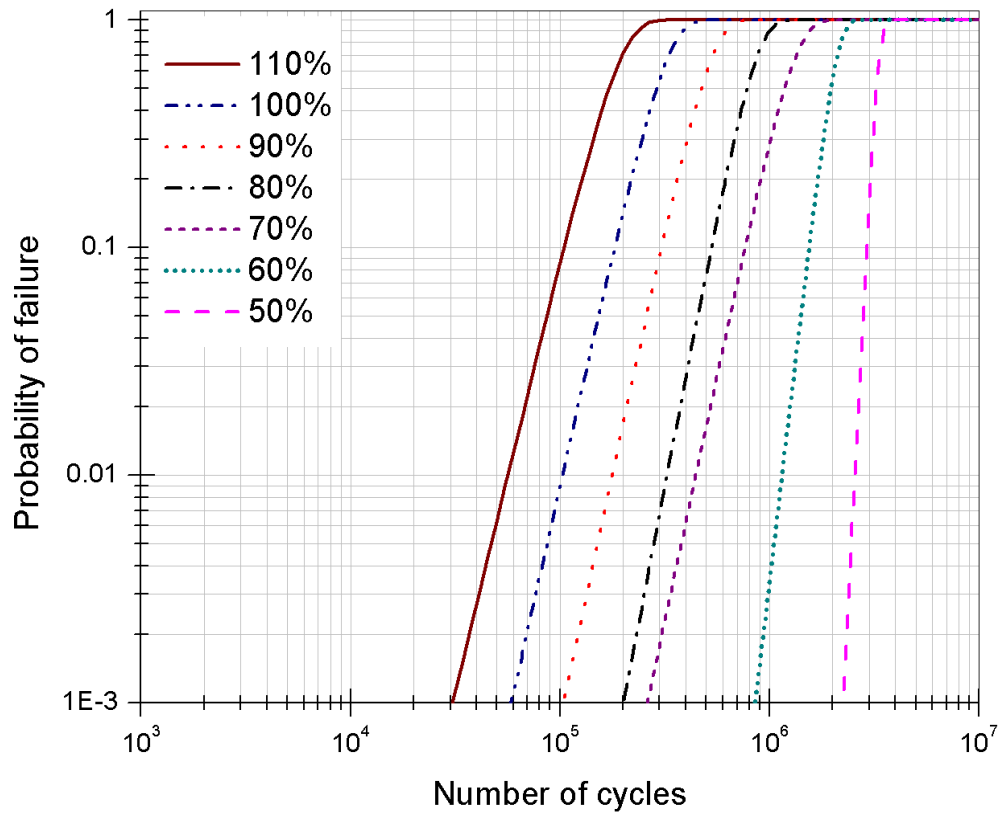


Figure 4.33 The probability of fatigue failure at different applied maximum cyclic stresses in multi-sized model.

Chapter 5 Quantification of Microstructural Effects on Fatigue Crack Branching in AA 7050 Al Thick Plates

In this chapter, a detailed fractographic and microstructural study, using stereo optical and scanning electron microscopy has been accomplished to characterize the behavior and mechanisms of fatigue crack growth with branching in thick commercial 7050-T7651 aluminum plate in the L-S orientation. The fractographs on the failed middle tension specimens which were used to determine crack growth rates, showed that the transition of lead crack from crystallographic growth (fatigue fracture) to non-crystallographic mode (overloading fracture) at ΔK value of $\sim 17 \text{ MPa}\sqrt{\text{m}}$ with few non-through thickness branches at the mid-thickness plane. The interior branch grew to through crack at ΔK of greater than $30 \text{ MPa}\sqrt{\text{m}}$. The intergranular fracture has been observed in branched cracks. A 3-D finite element model which took into account a non-through/through thickness branch in the lead crack tip was consequently developed to simulate the influence of branching on the crack growth behavior. The data collected from simulation demonstrated that ΔK data with crack branching was mainly increased as increasing the length of lead crack while the crack growth rates showed significant retardations where branching parallel to the load direction occurred, which was consistent with experimental results. The ΔK was decreased as the depth of crack branch increases with stable lead crack length.

5.1 Introduction

The thick (>5 in.) plate of aluminum alloy of age hardened 7050 is used extensively in aerospace applications where optimal mix of properties to include strength, corrosion resistance, fatigue resistance, stiffness and other desired characteristics are required [134, 135]. 7050 is a zinc-magnesium-copper type aluminum alloy to provide high stress-corrosion resistance and higher toughness than most other 7xxx series aluminum alloys by heat-treated and mechanically worked [90, 135]. The phenomenon of fatigue crack branching in precipitation hardened alloys, e.g. Al-Zn-Mg-Cu alloys, has been recognized for a long time. Driven by the increasing demand of thick plate of 7050-T7651 alloy for aircraft producers, the behavior and mechanisms of fatigue crack branching in a direction parallel to the loading axial need to be fully characterized for widespread use.

Early references to the phenomenon include microstructural studies [90-93] and mixed-mode fracture solutions [104, 114, 136-138]. The microstructure effects associated with grain boundary ductile fracture (GBDF) have been concluded with respect to the three main ideas which are (1) microvoid growth at large grain boundary precipitates, (2) strain localization in the soft, and sometimes solute-free, grain boundary precipitate free zones (PFZs) and (3) the influence of matrix precipitate shear providing inhomogeneous “planar” slip may lead to large stress concentrations to the grain boundary at the end of slip bands [94]. The published evidence strongly suggests that the first process have an overwhelming

important role though the last two ideas have been supported in many cases [94]. A bilayer model of a soft (PFZ) and a hard damaging zone (precipitates within grain) has been developed to elucidate the influence of the microstructural parameters on grain boundary intergranular failure in aluminum alloys, and the results showed that the stress triaxial, the void spacing and the PFZ thickness were the main parameters [115]. Recently, an investigation of delamination fracture by electron back-scattered diffraction (EBSD) in Al-Li alloy 2009 which has similar grain structure and fracture mode with Al-Zn-Mg-Cu alloys, demonstrated that the delamination was frequently occurred between variants of the brass texture component [101]. The other effects such as overloads and multi-axial stresses were investigated since a fatigue crack deviated from its nominal Mode I plane induces mixed-mode near-tip conditions even if the far-field applied stress is purely Mode I [137]. Suresh and Shih have presented a summary of available stress intensity factor (SIF) solutions for branched elastic cracks as function of the deflection angle and length of the deflected part of crack and examined the plastic near-tip stress and deformation fields for branched cracks [104]. To predict the path of a branched crack and calculate the associated Models I and II SIF for developing more accurate analytical solutions, a 2-D finite element program named Quebra2D was used [114]. However, the limitations of this numerical method must be pointed out that the FE calculations assumed linear-elastic condition while actual branches can cause local plastic deformation, and lack of microstructural features in their model. Recently, a numerical strategy was developed to account for fatigue fracture anisotropy for the prediction of crack branching and crack turning in advanced aluminum alloys by implementing a modified mixed-mode fatigue criterion into a 2-D FE shell structure model [139]. A comparison of the predictions with the actual crack paths, showed that the numerical method was only valid for branching angles with 0~45 degrees. In present work, a 3-D finite element method which took into account a branch at the lead crack tip perpendicular to the lead crack was developed for the quantitatively analysis of the influences of branching on crack growth behavior, by assuming conditions of elasto-plastic and large displacement. A fractographic and microstructural study providing the experimental data for simulations, has been accomplished to characterize the fatigue crack branching behavior and mechanisms in thick commercial 7050-T7651 aluminum plate in the L-S orientation.

5.2 Experimental details

5.2.1 Materials

The specimens tested in this study were cut from 7050-T7651 plate in the L-S orientation of parent thickness 139.7 mm (5.5 in.). The nominal compositions of the alloy are given in Table 5.1. Its tensile properties were characterized by using standard dogbone-shaped samples in tension as Table 5.2 shown. Figure 1 is the stress-strain curve measured by the tension test, which would be used in the finite element

simulations as constitutive behavior. This highly isotropic alloy had a high degree of lamellar, columnar, pancake-shaped grains parallel to L orientation, which was measured by electron backscatter diffraction (EBSD) as shown in Figure 5.2. The average grain size recorded as $792.12\mu\text{m}\times 206.28\mu\text{m}\times 71.63\mu\text{m}$ (L \times T \times S).

The T7651 heat treatment can be summarized as [139]: solution heat \rightarrow water quench \rightarrow stretch \rightarrow two stage aging. Discs of three millimeter diameter for transmission electron microscopy (TEM) observations were prepared by following procedures: punched out from samples with < 0.5 mm in thickness, mechanically thinned down to ~ 150 μm and electropolished using a twinjet with 30% nitric acid solution in methanol at -20 oC and 15V. TEM examinations were performed by scanning transmission electron microscopy (STEM) mode using CM 200 in Oak Ridge National Lab.

5.2.2 Fatigue tests

Fatigue tests were conducted and relevant data was provided from the Alcoa Tech. Center. Pin-loaded fatigue tests were carried out on middle tension (MT) specimens of 243.84 mm $\times 101.6$ mm $\times 6.32$ mm (in Figure 5.3) at a stress ratio $R = 0.1$, frequency of 25 Hz, and high humid air ($>90\%$). ASTM E647 standards for fatigue crack growth testing were followed to configure and prepare the MT specimens for testing to generate data. Specimens were machined to allow for 5.0 mm notch for crack initiation.

5.2.3 Fractography

The fractured middle tension specimen was provided from Alcoa Tech. Center as well as shown in Figure 5.4. It is the lower part of the fractured specimen. Both stereo optical microscopy (stereo OM) and scanning electron microscopy (SEM) were employed to study the mechanisms of crack growth with branching on the fracture surface of the alloy. A series of stereo optical micrographs were taken at $20\times$ magnification from the center-notch to both ends of the fracture surface plane and consequently a complete map for the full fracture surface could be collaged as Figure 5.5 shown. The features of crack growth with branching on the fracture surface, such as crack propagation stages and fracture modes were examined in a HITACHI S-4300 scanning electron microscope.

5.3 Simulation for Crack Branching in a 3-D FEA model

5.3.1 Methodology for calculating the driving force

A new method had been developed to calculate the driving force and crack growth rate with the configuration of a lead crack and a branch using FEM since that there is no theoretical equation can be applied in this situation. The classic fracture mechanics theory gives a solution for a center crack in an infinite elastic plane subjected to uniaxial loading as Eq. (5.1) and Eq. (5.2) [140]:

$$K = \sigma\sqrt{\pi a} \quad (5.1)$$

$$\sigma_{yy} = \frac{\sigma\sqrt{\pi a}}{\sqrt{2\pi r}} \quad (5.2)$$

where σ is far-field applied stress and a is half length of the center crack. The stress intensity factor, K , can subsequently be given. The range of stress intensity factor under fatigue condition, ΔK , is related to the stress ratio ($R = 0.1$ in present work), namely, $\Delta K = K_{max} - K_{min} = K - 0.1K = 0.9K$. σ_{yy} is the stress component along loading direction in a small distance within elastic zone, r , from the crack tip. Paris' law (Eq. 5.3) [141] relates the stress intensity factor range to the crack growth rate, da/dN , under a fatigue stress regime.

$$\frac{da}{dN} = C \cdot \Delta K^m \quad (5.3)$$

where a is crack length and N is the corresponding number of cycles. C and m can be determined by the linear graph on a log-log plot of ΔK vs. da/dN . Based on above equations, the method for calculation of the driving force of fatigue crack growth with branching would be introduced in next.

Figure 5.6(a) shows that there is a center crack in an infinite plane subjected to uniaxial loading, and a branch perpendicular to the center crack located at the tip. The stress field around the branch and center crack tip would be analyzed using FEA. The branch in Figure 5.6(a) then can be removed but keep the center crack and the exactly same stress field as shown in Figure 5.6(b). An assumption has been made that there is an imaginary far-field stress, σ_{ima} , is applied to an infinite plane with one center crack (half-length is a) which can lead to a stress field around the crack tip, and the stress field is same as the stress field which caused by the center crack and a branch subjected to a far field stress, σ , in infinite plane. To be specific, σ_{yy} in Figure 5.6(a) is the stress component along loading direction in a distance, r , from the crack tip in the configuration of a center crack and a branch under uniaxial loading (σ). At this circumstance, σ_{ima} denotes the far-field stress which can cause σ_{yy} around the center crack tip as Figure 5.6(b) shown. The Eq. (5.2) can be rewritten as Eq. (5.4):

$$\sigma_{yy} = \frac{\sigma_{ima}\sqrt{\pi a}}{\sqrt{2\pi r}} \quad (5.4)$$

σ_{yy} would be collected using FEA, σ_{ima} can then be given. Through Eq. (5.1) and Eq. (5.3), replacing σ to σ_{ima} , ΔK and da/dN for crack growth with branching can consequently be determined.

5.3.2 3-D elasto-plastic finite element modeling

A 3-D plate with a center crack and a branch was studied. The specimen, shown in Figure 5.3, has a length of 243.84 mm, a thickness of 6.32 mm, a width of 101.6 mm, under pure Mode I loading. Equal and

opposite pressures were applied at both ends in the longitudinal direction and the maximum pressure value was set equal to the value from experiments, 131.5 MPa. Symmetry conditions reduced the specimen to a quarter model in this work as Figure 5.7(a) shown, and the length was set equal to the width for computing convenient. A rectangle geometry has a length as long as the half center crack that was measured from morphology of fracture surface, and a width of 6.32 mm (as same as the thickness of the plate) was donated as the half center crack so that Figure 5.7(a) defined a model with a center crack but without a branch. In order to analyze the model with a center crack and a branch, a shell structure would be set as a branch assembled at the center crack tip perpendicular to the center crack as Figure 5.6 shown. Two kinds of shell structures were used for representing the non-through thickness branch (Figure 5.7 (b)) and through thickness branch (Figure 5.7(c)) due to the fractographic observations showed that crack branching occurred in the interior at first and branch sizes increased until large enough to span full thickness. The FEA program used in this work was Abaqus/CAE and the matrix of the alloy was assumed to be continuous, homogenous and elasto-plastic. The material data for the bulk material properties were $E = 71.59$ GPa and $\nu = 0.33$. The plastic response of constituent behavior in the model was specified by the Figure 1 curve. A very refined mesh was used in a small region around the center crack tip and branched crack tip.

Dimensions of branched cracks were determined by experimental measurements. The geometry of through branch as shown in Figure 5.7(c) was simply set as a rectangle shape. It was readily to measure the depth of the through thickness branch, b_1 (in Figure 5.7(c)), from the external surface of the specimen as in Figure 5.4 shown. In addition, the width of the through branch, b_2 , was set equal to the thickness of the plate, 6.32 mm. Despite the depth of the non-through thickness branch which occurred in the interior cannot be known directly, an assumption can be made to estimate this value. The geometry of non-through branch was elliptical shape and only half was used in the model as Figure 5.7(b) shown. The width of the non-through thickness branch, b_2 (in Figure 5.7(b)), can be measured from the morphology of the lead crack fracture surface, and the depth, b_1 , was assumed as a function of b_2 .

5.4 Experimental Results

5.4.1 Growth rates by experiments

Fatigue tests were performed on specimens machined from the thick (139.7 mm) plate material in the L-S orientation by Alcoa Tech. Center and the graph of Crack growth rates (da/dN) vs. ΔK was given in Figure 5.8 (a). It should be noted that the fatigue curve is not an expected common sigmoidal shape which can be expressed by Paris' law, but is a curve with increasingly retarded growth rate at certain points. Crack branching along the loading direction (L direction) in the specimen was the major factor for the retardation in the fatigue curve, which is consistent with the conclusion that a crack periodically

deflected from its nominal growth plane could offer one possible way of enhancing the apparent resistance to fatigue crack growth [137, 142]. Similar curve was reported in previous research [50, 143]. Figure 5.8(b) is the plot of da/dN vs. the length of lead crack which reveals the relationship between the crack growth rate and the position of the crack front.

5.4.2 Microstructure of 7050-T7651 alloy

As shown in Figure 5.9, the small particles of ~5-10 nm in size were distributed in the grain interior uniformly. These GP zones (GPZs) were formed during homogenizing in supersaturated solid solution. Some plate-like precipitates besides GP zones, were η' phase, which was semi-coherent with matrix lattice [139]. GPZs and η' phase were the main precipitates to highly strengthening the 7050-T7651 aluminum alloys. Fine precipitation was formed within the grains with the attendant formation of grain boundary precipitates and the precipitate free zone (PFZ) after the first aging. Both the matrix and grain boundary (GB) precipitates coarsened after the second aging while the PFZ width remained unchanged in Al-Zn-Mg-Cu alloys [92]. The PFZ along small angle grain boundary were observed by STEM as Figure 5.9(a) shown and the width of PFZ were measured, which were ~0.05-0.15 μm . Large grain boundary precipitates within the PFZ (Figure 5.9(c)) was ~60 nm in length. Unwin and Smith [144] studied the influence of various features of the microstructure on measured values of fracture toughness and they demonstrated that the K_{IC} and the amount of intergranular fracture can be affected significantly by the area fraction of the grain boundary covered by precipitates (A_f), while the effect of changing PFZ width on toughness should be negligible. Embury and Nes [145] showed that the fracture strain and toughness varied linearly with $1/\sqrt{A_f}$ in the Al-Zn-Mg-Cu alloys. Figure 5.9(b) and (c) shows that the high area fraction of grain boundary precipitates can be observed in 7050-T7651 alloy which can lead to grain boundary intergranular fracture and sequent lead to fatigue crack branching parallel to L direction due to the lamellar, columnar grain structure. And the strain localization at the soft PFZ also promote the grain boundary ductile fracture at the grain boundary precipitates [90, 94, 146].

5.4.3 Fatigue crack growth, branching and fracture

The fatigue test middle-tension specimen after fatigue failure demonstrated the lead crack propagation path as shown in Figure 5.4 and Figure 5.5. The crack was initiated from the both ends of the center notch, propagated in the direction perpendicular to the loading axis (rolling direction of the 7050-T7651 alloy). Fatigue crack branched repeatedly to the direction almost parallel to the loading direction at the second fatigue crack growth stage. Eventually, the crack growth direction had been changed by crack deviation and the ligament fracture occurred that was not anticipated from mechanical loading conditions. Figure 5.5 is the morphology of the fracture surface of lead crack before final ligament fracture, which showed three basic fracture mechanisms:

- i Crystallographic growth and fatigue fracture, showing flat and smooth surfaces, the pattern of river and range, visible striation markings, see Figure 5.10;
- ii Ductile transgranular fracture and overloading fracture, characterized by dimples, the center of which contain constituent particles that served as the microcavity/ microvoid nucleation site, showing rough surfaces, see Figure 5.11;
- iii Ductile intergranular fracture, characterized by relatively smooth surfaces, revealing the initial grain structure, see Figure 5.12.

The fractographs of the final ligament fracture where crack deviation occurred showed one basic mechanism: Grain boundary ductile intergranular fracture, characterized by dimples on grain boundary, see Figure 5.13.

During the early stage of the lead fatigue crack propagation, the crystallographic growth mode dominated the growth process (Figure 5.10) due to the low crack growth rate and low ΔK value. The fracture surface displayed many orderly cliffs (Figure 5.10(a)) with striation markings on step-like patterns within each grain (Figure 5.10(b)), parallel to the growth direction, which formed the pattern of river and range. In Figure 5.12 (a) and (b), several small branches ($\sim 150 \mu\text{m}$ in length and $\sim 1.5 \mu\text{m}$ in thickness) followed grain boundaries, and GB ductile dimples showed on the grain boundary of one of those branches, showing ductile intergranular fracture in this stage. This apparition of the intergranular fracture model was related to the precipitation on grain boundaries and soft PFZs as mentioned in last section. The branches that existed during the early stage were not responsible for the retardation in the crack growth rate according to the plot of da/dN vs. the length of lead crack (Figure 5.8(b)). Because the first retardation occurred at the lead crack length of $\sim 10 \text{ mm}-12.5 \text{ mm}$, but the fractographs of the lead crack propagation indicated that the early stage ended at the lead crack length of $\sim 7.50 \text{ mm}-8.5 \text{ mm}$, as shown in the Figure 14, which shows the transition of the lead crack from crystallographic growth mode in early stage to non-crystallographic mode in the second stage.

In Figure 14, the fracture surface was relatively flat and smooth, with a crystallographic growth mode during the early growth stage. When the lead crack propagated up to $\sim 7.50 \text{ mm}-8.5 \text{ mm}$, the morphology of the fracture surface became uneven and showed small black patches (see Figure 5.14(a)) where the transition period was. The subsequent fractograph turned into a completely rough and ductile dimple fracture surface, revealing visible dark regions. In Figure 5.15 (b) and (c), it can be noted from the micrographs of high magnification that the visible dark region seemed like a “valley” and branches were gathered around it, one even went through the interior of the valley. This “valley” was regarded as the beginning of the second stage of crack growth. The fracture modes of a ductile transgranular and

overloading started to dominate at ΔK value of $\sim 17 \text{ MPa}\sqrt{\text{m}}$ during this crack growth stage. Figure 5.15(e) shows the micrograph of the large dark region in further crack propagation, similar to Fig 5.15(b) and (c), i.e. many branches involved into the “valley” and “hill”, showing the feature of ductile fracture by overloading. From the higher magnification of fractographs in this stage (see Figure 5.11(b)), there were dimples containing the second phase particles or precipitates served as the microvoid or microcavity nucleation sites, which were the characterizing feature for ductile transgranular fracture.

The fractographs in Figure 5.15(b) and (c) shows that there were three ways of the lead crack re-propagation once it encountered branches that nucleated and grew along vertical direction, which is shown schematically in Figure 5.15(d): A, B and C represented three different positions in a same branch, respectively, and black arrows indicates the lead crack propagated across these three positions. (1) When the crack re-propagated across the root of the branch like what A represented, the new surface of lead crack was flat and stayed in a same plane with the original surface, the whole branch was kept in this part of specimen. (2) If the crack re-propagated from the branch tip as C represented, it would go down along the branching direction (almost vertical) and then returned to the main growth direction to form a new, relative flat and lower surface, so that a surface of the branch become the steps and another surface of the branch was removed completely. (3) B represented the situation that crack re-propagated from the middle of the branch between A and C, a part of the branch was taken off and the rest part still was remained, showing not vertical steps and rough new surface. Some branches propagated individually at first, and then intersected with each other, see Figure 5.16. These three ways and intersections between branches can be used to describe all the crack re-propagation behaviors with branching, it was A if the surface was flat, and it would be B or C when the steps and uneven surface showed up, otherwise it could be a combination. It also gave reasons to explain the phenomena of “valleys” and “hills” in the fracture surface.

Since the dark regions, namely, “valleys” and “hills”, in fracture surface were led to by branching and interactions of branches, the behaviors of branching with the lead crack progression can be demonstrated by the changing of the dark region size on fracture surface along the main growth direction. Figure 5.17 shows that the dark region started at the internal centerline of the specimen due to that the constraint and the elastic energy density in center region were maximum, and gradually increasing in size with the lengthening crack size with higher ΔK value, until the dark region with branching span the full thickness of the specimen at ΔK of greater than $30 \text{ MPa}\sqrt{\text{m}}$ and crack length of longer than $\sim 20 \text{ mm}$. That means crack branching started earlier on the inner, mid-thickness plane, and then gradually increased as the vertical lines indicated in Figure 5.17. Finally the branching started on the external surface and span the thickness of specimen, parallel to the stress axis. A similar phenomenon was found in 7050-T7451 [147]. Fractography was conducted at the first and the second through-thickness branches near the external surface in attempt to showing an intergranular, delamination-type fracture along the rolling plane, see

Figure 5.12(c) and (d). It is noted that the branch followed the grain boundary in lamellar grain structure in Figure 5.12(c) which was the first through-thickness branch. Original grains can be observed from the fractograph on the lead crack fracture surface before the first through-thickness branch close to the external surface, which revealed crystallographic-like fracture mode in Figure 5.12(c). For the second through-thickness branch nearby external surface in Figure 5.12(d), with longer lead crack and higher ΔK , the morphology of the fracture surface around it become fully transgranular ductile fracture mode. As shown in Figure 5.17, before the first through-thickness branch, the morphology around these dark regions indicated transgranular ductile fracture by rapid overloading failure which nearly formed an isosceles triangle, conversely, the internal surface without dark regions (nearby external surface) stayed crystallographic-like fracture mode due to slow crack propagation and fatigue failure. After the first through-thickness branch, the fractograph demonstrated fully transgranular ductile fracture mode for the lead crack perpendicular to the loading direction and intergranular ductile fracture mode for branches parallel to the loading direction, until the final deviation led to ligament fracture and eventually specimen failure which showed grain boundary ductile intergranular fracture as shown in Figure 5.13.

The findings of this experimental section provide the base for finite element analysis about the crack branching. See Figure 5.12, Figure 5.15 and Figure 5.16, the branches followed grain boundaries were not totally straight since the actual resistances for branching were larger than ideal assumption while it was assumed that the branches with rectangle shape or elliptical shape was perpendicular to the lead crack in FEA model. It was evident that the branches were responsible to the retardation of lead crack growth rate according to the morphology of lead crack fractural surface and the plot of da/dN vs. the length of lead crack (Figure 5.8(b)). To be specific, each individual through thickness branch correspondingly caused one fall of crack growth rate in the plot. However, before the first through branch, those falls in the plot were induced by the dark regions what were formed from a group of many non-through branches, rather than one single branch. Therefore, the dimensions of branches for FEA model can be defined as two types. For through thickness branch, see Figure 5.7(c), it is rectangle shape with a width of 6.32 mm and a depth measured from the external surface. For non-through thickness branch, see Figure 5.7(b), it is elliptical shape with a measured width and a depth as a function of width.

5.5 Simulation Results for Crack Branching

5.5.1 Determination of the depth of non-through branches for FEA model

Two constant values were tested to determine the relationship between b_1 (depth) and b_2 (width): $b_1 = b_2$ (depth = width) and $b_1 = 2b_2$ (depth = 2×width) for non-through branch of elliptical shape. Figure 18 show the stress field and energy density field along the thickness of fracture surface at lead crack front under four configurations of lead crack and branch, when the lead crack length was consistent but the branch

was different size. See Figure 5.18, ‘lead crack’ means there was only a lead crack without any branch. ‘Through branch’ is a lead crack with a rectangle shape through thickness branch which has the width as same as the thickness of the plate. ‘Non-through branch $b = 2a$ ’ (b is long axis. a is short axis. $b = b_1$) represents a lead crack with an elliptical shape branch that the depth has the same size as width. ‘Non-through branch $b = 4a$ ’ means a lead crack with an elliptical shape branch having a depth of two times of width. Figure 5.18(a) shows the stress component field along the loading direction, namely, σ_{yy} , changing with the distance along the thickness of fracture surface. In the ‘lead crack’ situation, the stress was larger at the middle portion of the plate than the portion nearby the external surface as a result of that the constraint for dislocation movement was highest in the centerline part while the surface was relatively free. As shown in Figure 18(b), the energy density field shows the similar trend that the energy density were minimum at the two side surfaces and increasing to the maximum value at the centerline of the plate. If there was a through thickness branch located at the lead crack tip, the stress and energy density almost kept constant through the full thickness of the plate from the two side surfaces to the centerline, see Figure 18(a) and (b), and the value was only half of the minimum value in the ‘lead crack’ case. This is because branching through thickness would release a part of the elastic strain energy at the lead crack tip and lower the stress field. When the branch was interior crack, non-through the thickness of the plate, the stress field and energy density field distribution depended on the dimensions of the depth of the elliptical branch. For $b = 2a$, namely, the width is as same as the depth, the stress increased sharply at the centerline due to the branch with too short depth inducing much higher stress concentration at this point, which demonstrated that the branching should continue to grow until the stress decreased to lower than the value in no branch situation. The value of energy density field fell at the middle portion of the lead crack tip where the non-through branch existed but still higher than the value in the through branch situation, which indicated that non-through branch could release some part of elastic strain energy as well, but less than the through thickness branch. In the $b = 4a$ (depth = $2 \times$ width) situation, the stress was minimum at the centerline portion and lower than the value in the lead crack without any branch case, but higher than the value in the lead crack with a through branch. The stress increased to as same as the value in the no branch case closing to the two side surfaces because of the absence of branching at this portion. The elastic strain energy was released more than in last situation as seen in Figure 5.18(b) for the branch was deeper. The stress value at this situation is appropriate for the finite element analysis. Therefore, the depth of the elliptical non-through branch has been determined as two times of the width of the branch in the following simulation of fatigue crack branching behavior.

5.5.2 Effects of the depth of branch on driving force

The plot of ΔK vs. the lead crack length in Figure 5.19(a) shows the relationship between the ΔK and the position of the crack front, demonstrating that the non-through thickness branches caused retardation at

five noticeable points (see the grey blocks in Figure 5.19(a)) with lead crack growing. These five positions at the lead crack were measured from the plot and there were: 10.625mm, 12.637mm, 14.667 mm, 16.160 mm, and 18.416 mm, respectively. The width of dark regions, caused by non-through branches and intersections, on the fracture surface at these five positions were measured from the morphology of the fracture surface of specimen and the depth were calculated as two times of the width. The depth of through thickness branches could be measured from the external surfaces of the specimen. So the relationship between the depth of branch and the length of lead crack was investigated and the result was shown in Figure 5.19(b). The result shows that the branch depth increased with lead crack propagating. The plot in Figure 5.19(c) reveals the influence of the branch depth and lead crack length on the driving force for fatigue crack propagation, ΔK . The results were collected from the finite element analysis data by simulating the stress field at the lead crack tip of those five positions where the retardation occurred due to the crack branching. Each lead crack length was simulated twice with two different depth of interior non-through branch. The methodology and equations for calculation of ΔK were introduced on previous section (Section 5.3.2 and Eq. (5.1), (5.2) and (5.4)). The plots, see Figure 5.19(c), indicated that under the same lead crack length, the value of ΔK become lower when the depth of branch increased, meaning that the driving force for crack propagation fell with the increasing branching when the lead crack was stable and not to propagate. With the lead crack increasing, the branching was increasing, leading to the larger ΔK and higher crack growth rate. Therefore, it may be concluded that the influence of the depth of branch on ΔK was not independent, but was comprehensive and related to the length of lead crack. If the lead crack length was stable, the value of ΔK was decreased as the depth of crack branch increases.

5.5.3 Validation of the simulated fatigue crack growth rate by experiments

Comparing the actual fatigue crack growth rate from the experiments to the predicted fatigue crack growth rate based on finite element analysis in Figure 5.20, one sees that these agree to each other very well. The parameters for calculation of predicted path were taken from the experimental results. $m = 1.34847$ and $C = 7.65e-06$. Those values of retardation were calculated by using the methodology introduced in section 5.3.2 with modeling a non-through branch or through branch at a lead crack tip by finite element analysis. Other points at the sigmoidal curve were calculated by Paris' law. The result proved the validation of the methodology for predicting the fatigue crack growth behavior with branching through finite element simulations.

Although the current predicted data can only agree with the experiment data for the specimen in this work, the methodology is valid for any specimen with branching and the experimental results would be consistent, at least in little differences, if the fatigue tests can be conducted at same conditions for enough times.

5.6 Conclusions

- 1) Crack branching along the loading direction (L direction) in an AA7050 Al alloy thick plate was the major factor responsible for the retardation of fatigue crack growth.
- 2) The width of precipitate-free zones was $\sim 0.05\text{-}0.15\ \mu\text{m}$ and the precipitates within the PFZ at grain boundaries were $\sim 60\ \text{nm}$ in length, which probably led to grain boundary dimple fracture and sequent fatigue crack branching parallel to L direction with the lamellar, columnar grain structure.
- 3) The transition of the lead crack growth from a crystallographic growth mode (fatigue fracture) to the non-crystallographic mode (overloading fracture) was observed at ΔK of $\sim 17\ \text{MPa}\sqrt{\text{m}}$.
- 4) A few non-through thickness branches were formed first at the mid-thickness plane. The first crack branching through the thickness occurred at ΔK greater than $30\ \text{MPa}\sqrt{\text{m}}$ and the lead crack longer than $\sim 20\ \text{mm}$.
- 5) Intergranular fracture was observed in the branched cracks, mainly due to the precipitate-free zones along grain boundaries in the Al alloy plate.
- 6) The results obtained from the finite element simulation demonstrated that ΔK for crack branching was mainly increased as increasing the length of lead crack, while the lead crack was significantly retarded where branching occurred parallel to the load direction. This was consistent with experimental results.
- 7) The ΔK for the lead crack was decreased as increase in depth of the branched crack ahead of the lead crack tip.

Table 5.1 Chemical compositions of 7050-T7651 aluminum alloy. (wt. %)

Zn	Mg	Cu	Mn	Cr	Fe	Si	Ti	Al
6.2	2.3	2.3	0.1	0.04	0.15	0.12	0.06	Balance

Table 5.2 Mechanical properties of 7050-T7651 aluminum alloy.

Young's modulus (GPa)	Passion ratio	Yield strength (MPa)	Ultimate tensile Strength (MPa)
71.59	0.33	448	500

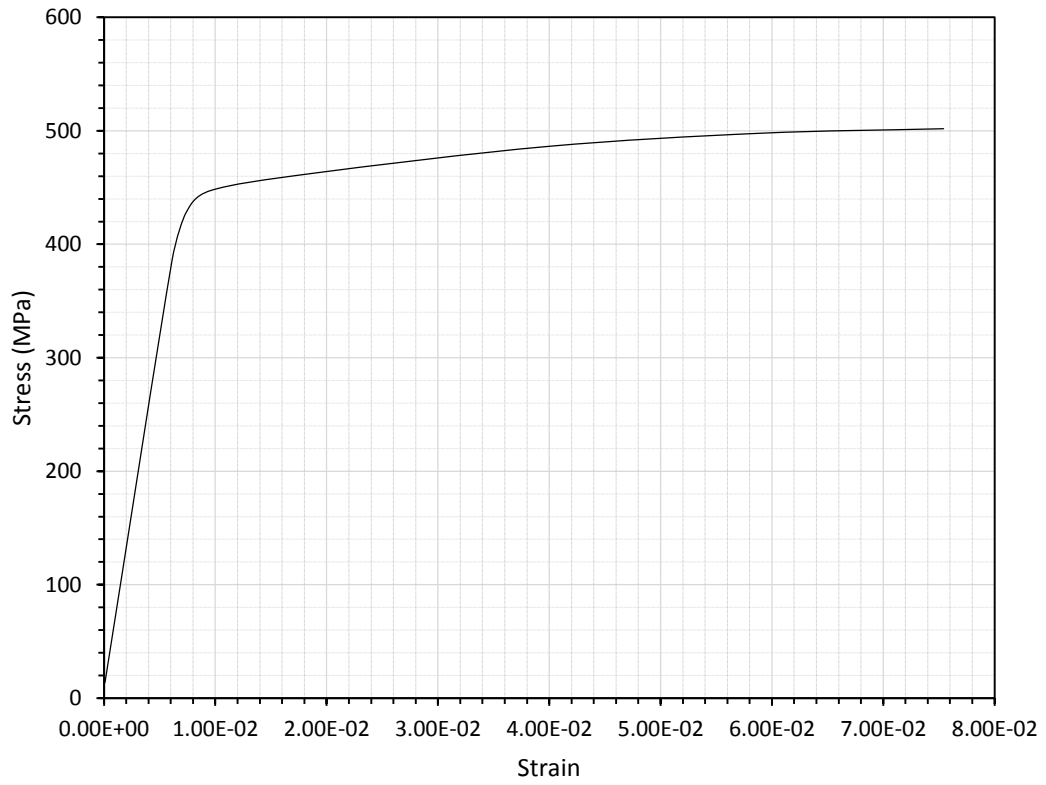


Figure 5.1 Experimental measured stress-strain curve.

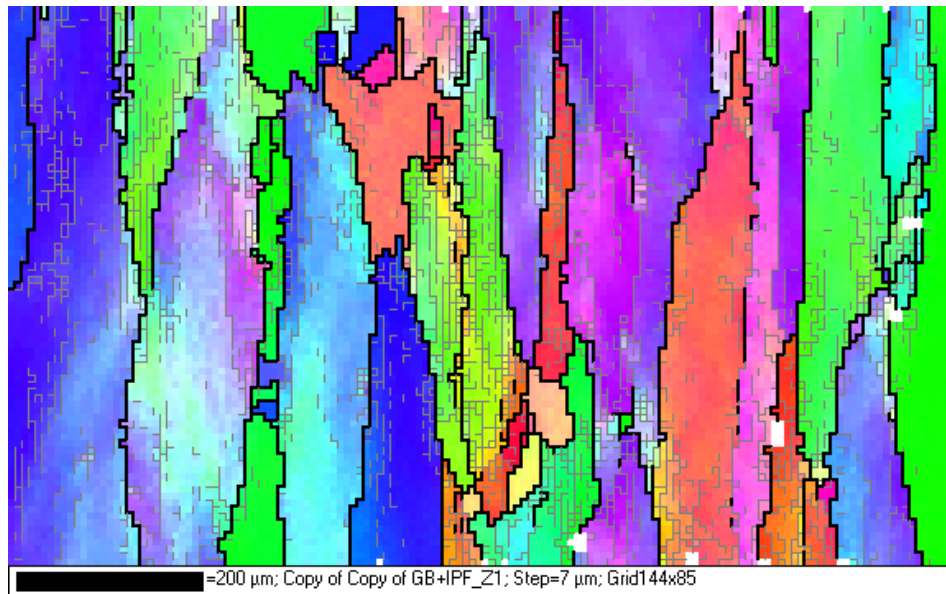


Figure 5.2 Pancake-shaped grain structure of 7050-T7651 in L-S plate measured by EBSD.

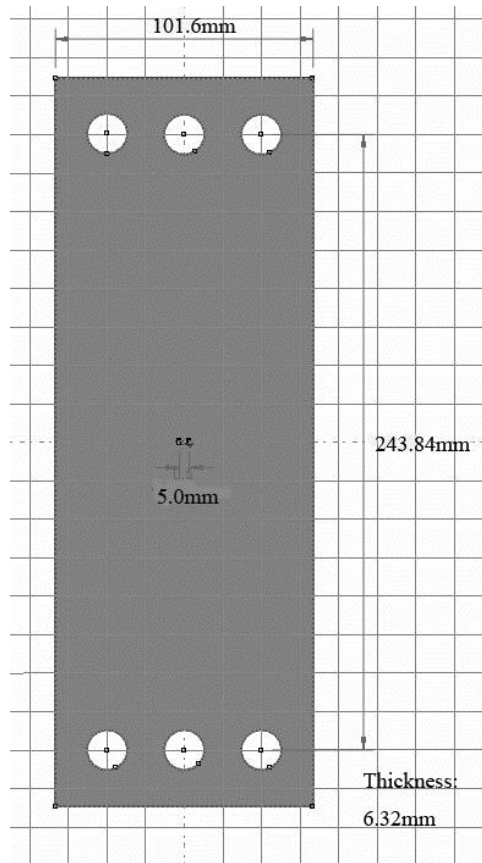


Figure 5.3 Machined specimen configuration.

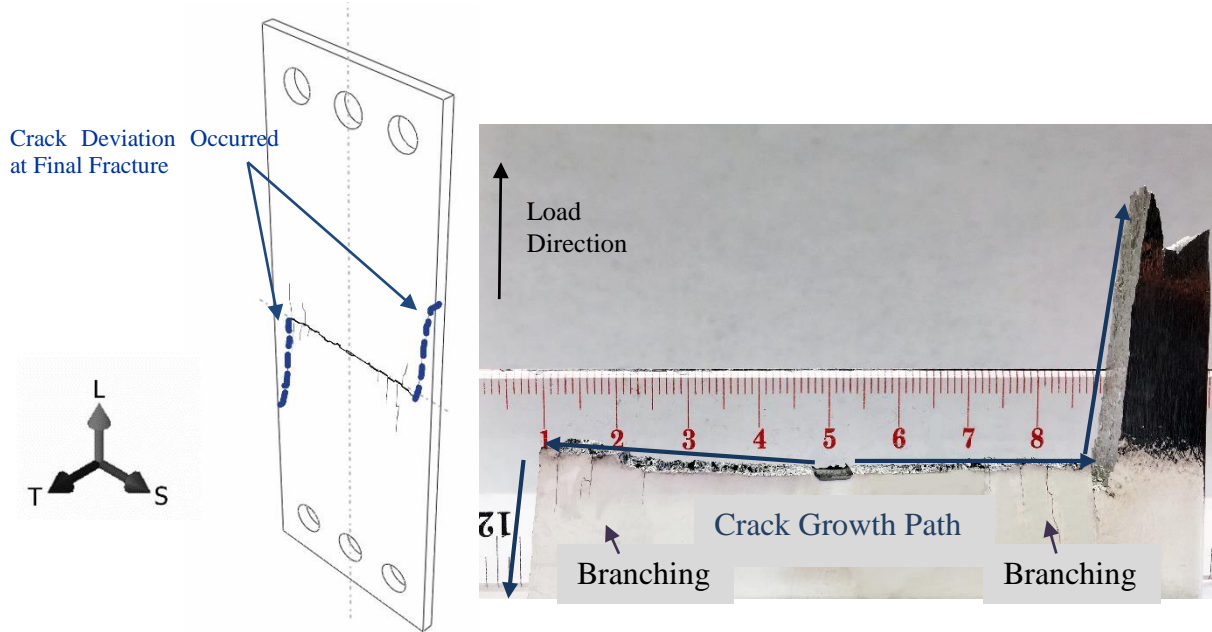


Figure 5.4 The fractured middle tension specimen of 7050-T7651.

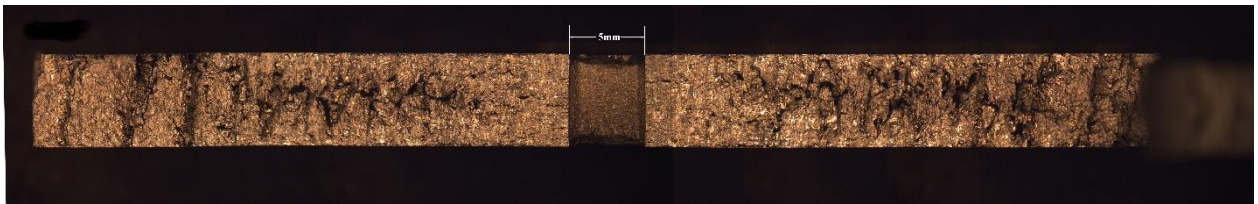


Figure 5.5 Morphology of the fracture surface of the 7050-T7651 middle tension specimen.

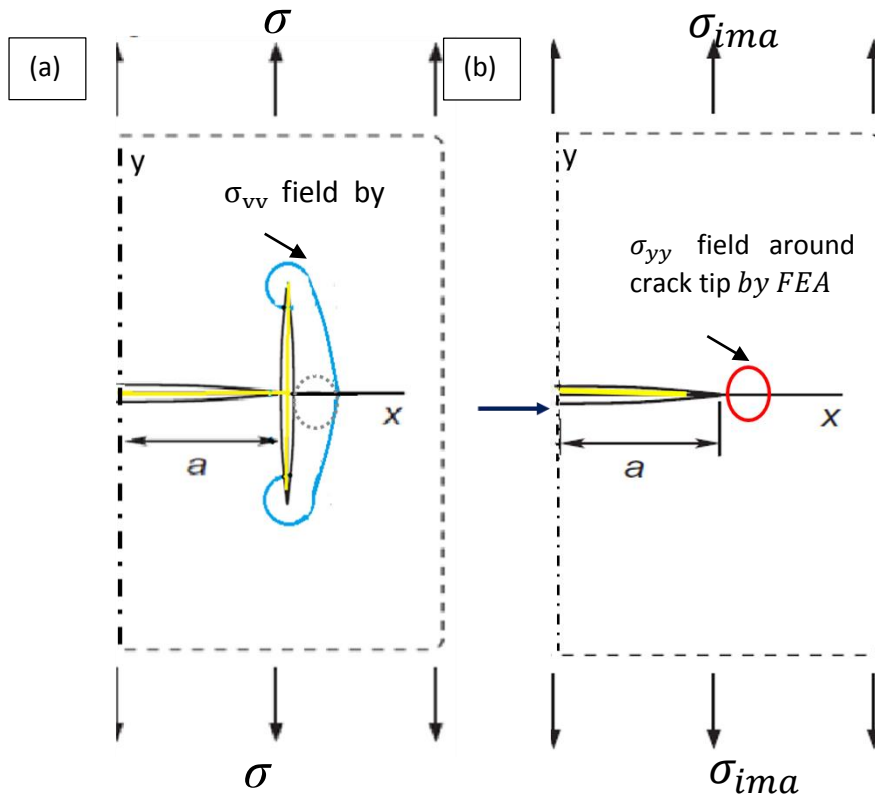


Figure 5.6 Schematic graphs for a new method to calculate the driving force with the configuration of a center crack and a branch using FEM.

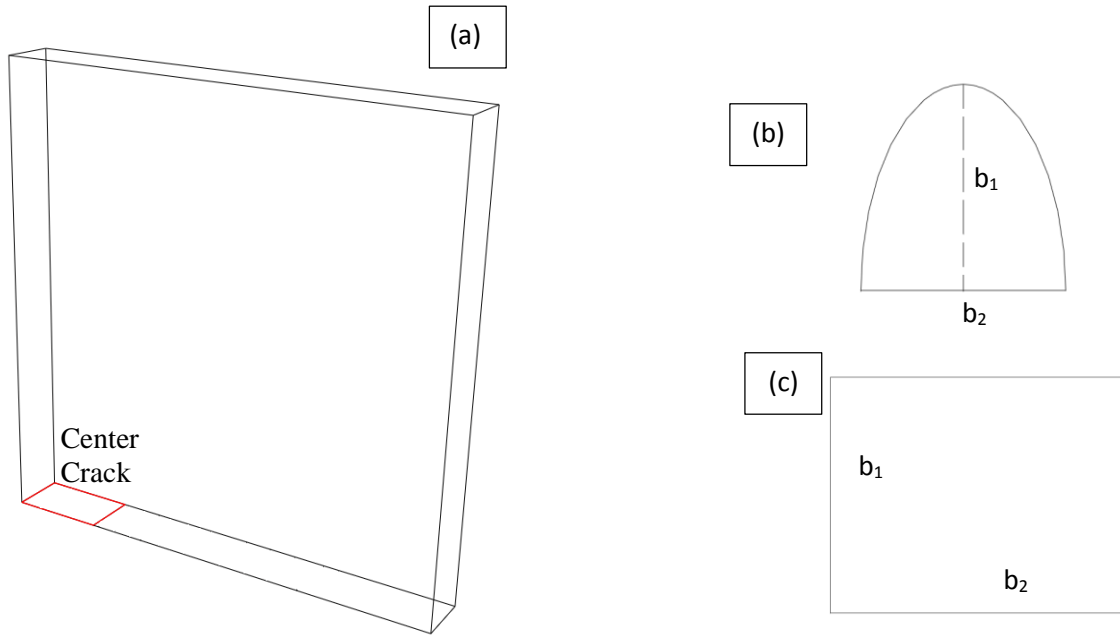
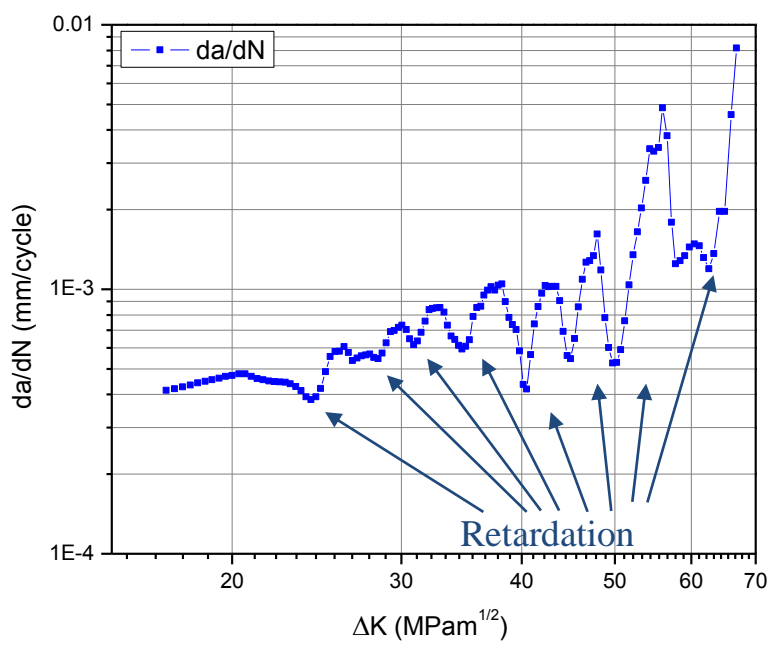


Figure 5.7 Model geometry of the plate with a center crack and a branch. (a) the model geometry without branch, (b) the geometry of non-through thickness branch, (c) the geometry of through thickness branch.

(a)



(b)

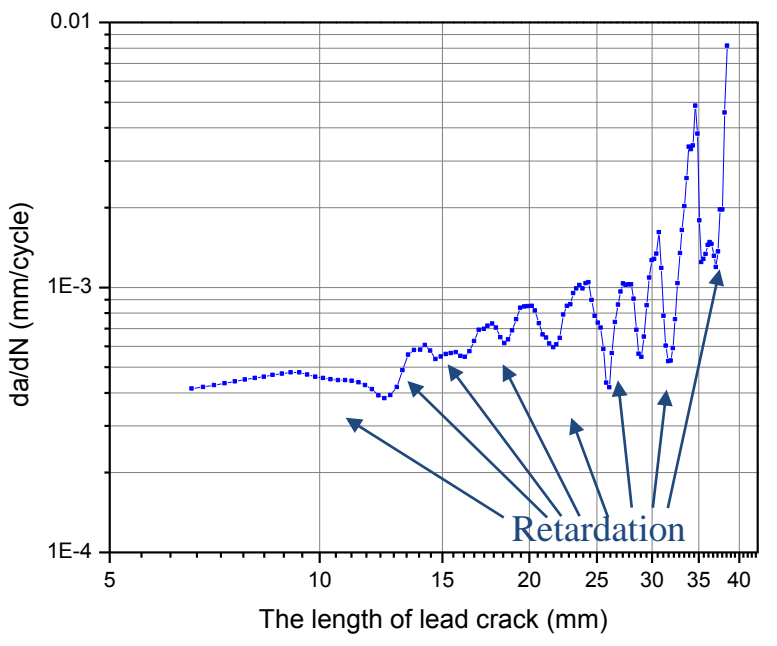


Figure 5.8 Crack growth data of 7050-T7651 aluminum alloy L-S specimen, (a) da/dN vs. ΔK , (b) da/dN vs. the length of lead crack.

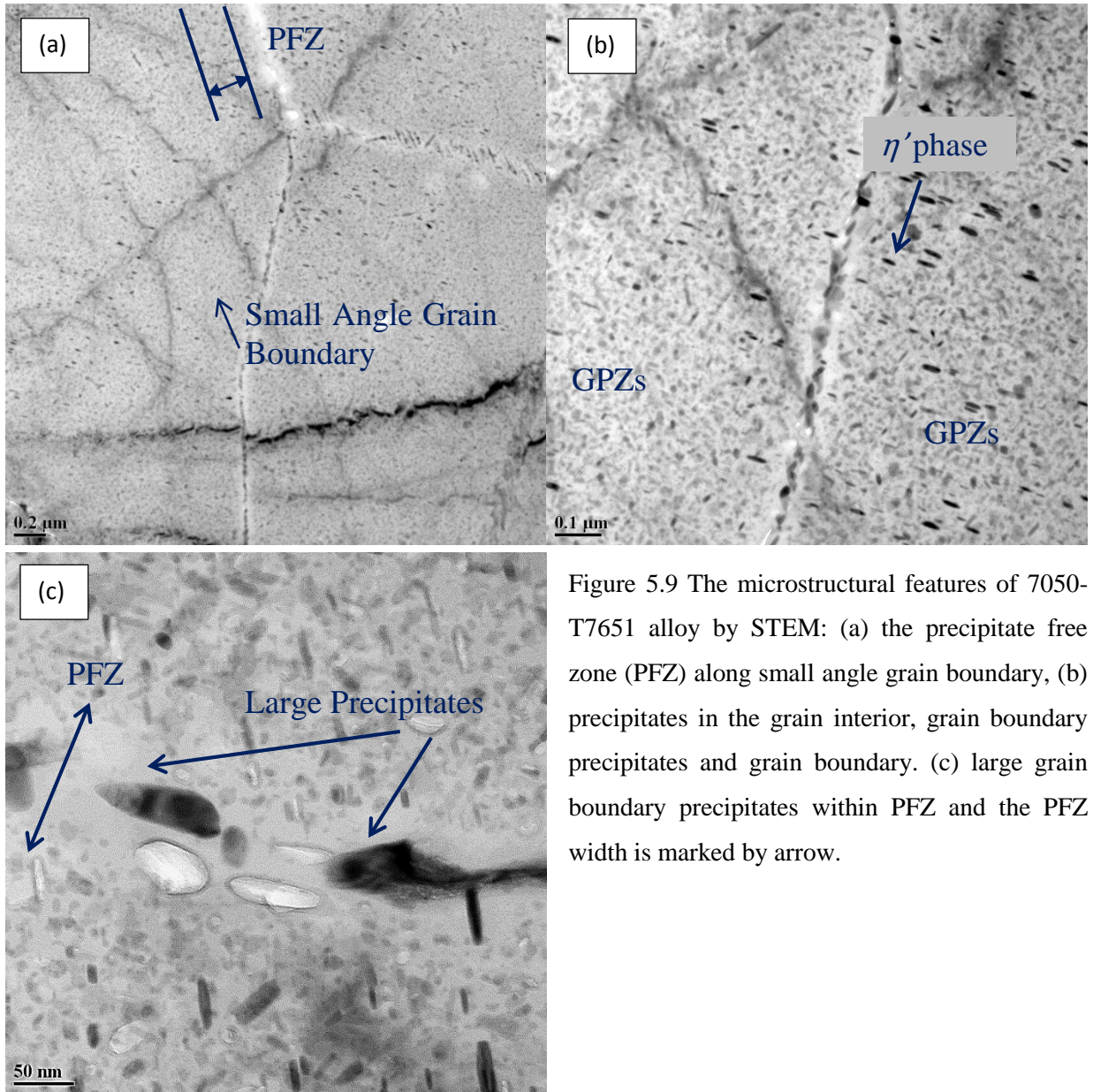


Figure 5.9 The microstructural features of 7050-T7651 alloy by STEM: (a) the precipitate free zone (PFZ) along small angle grain boundary, (b) precipitates in the grain interior, grain boundary precipitates and grain boundary. (c) large grain boundary precipitates within PFZ and the PFZ width is marked by arrow.

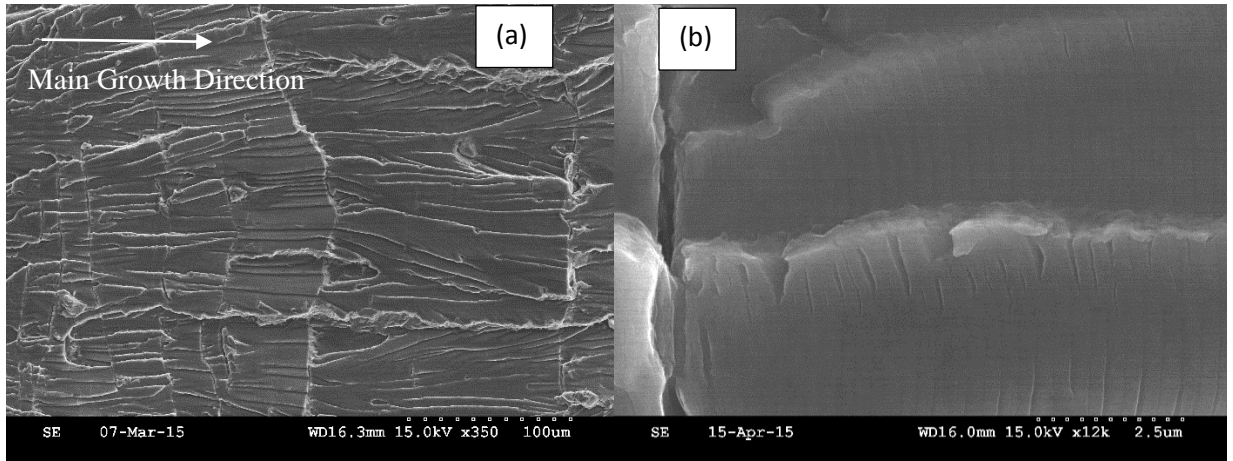


Figure 5.10 Fractographs of the middle-tension specimen with (a) crystallographic growth during the early stage of the lead crack, (b) the fatigue striations.

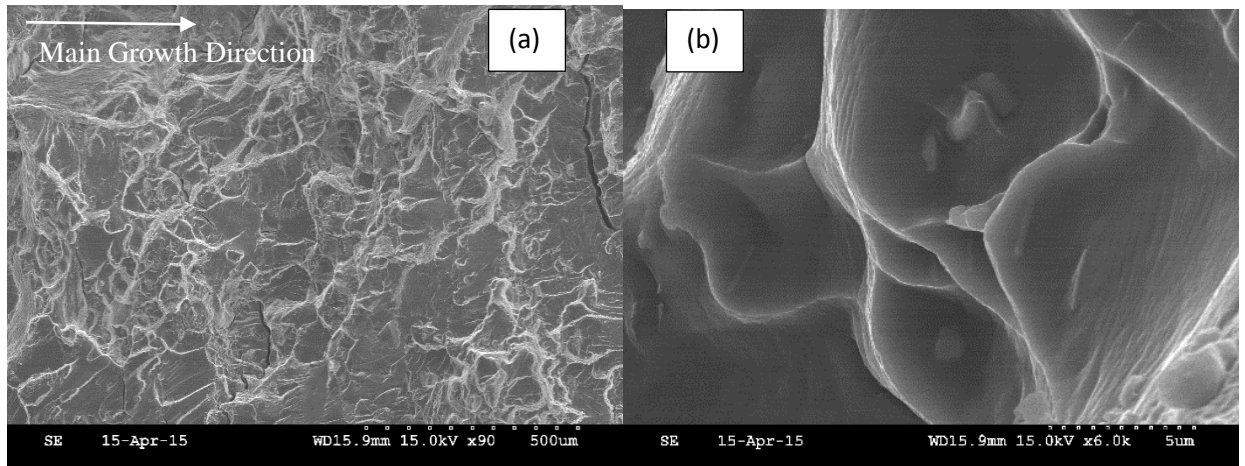


Figure 5.11 Fractographs of the middle-tension specimen during the second stage of lead crack growth (a) ductile fracture, (b) dimples containing the second phase particles.

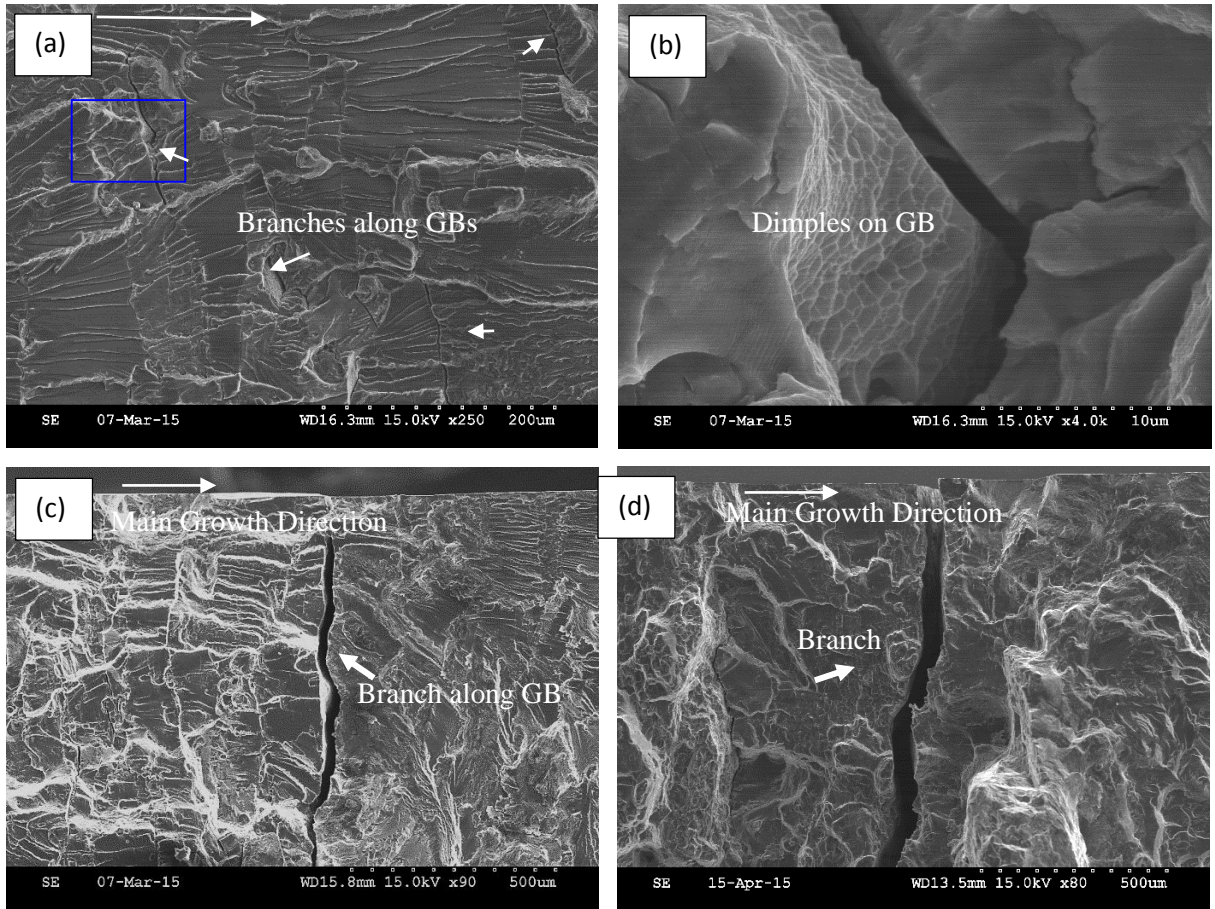


Figure 5.12 Fractographs of lead crack with branched cracks, (a) intergranular fracture during the early stage of crack growth as branches along GBs (white arrow pointed), (b) high magnification of one of branch in (a) showing GB dimples, (c) intergranular fracture during the second stage of crack growth as the first through-thickness branch along GB, (d) the second through-thickness branch.

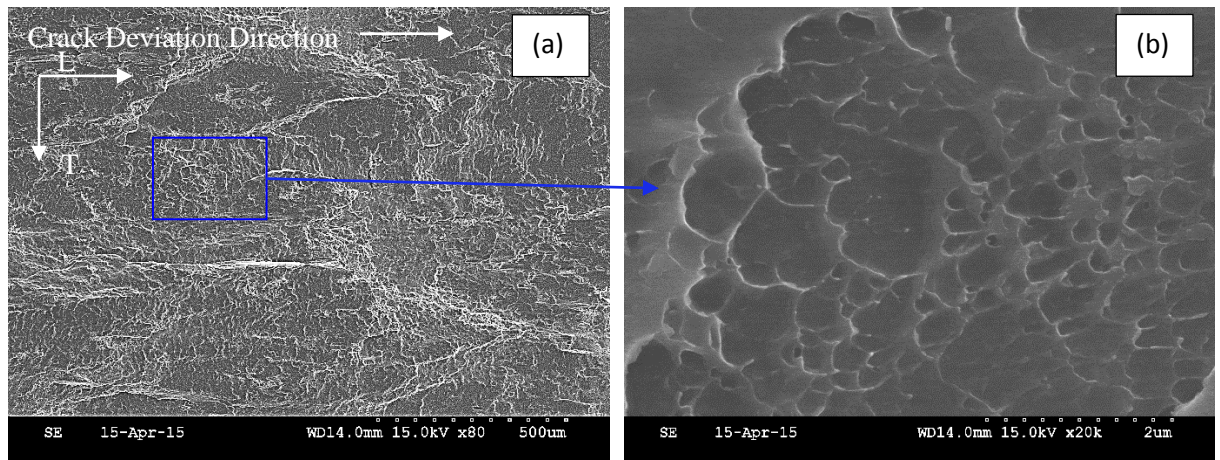


Figure 5.13 Fractography of final ligament fracture where crack deviation occurred, (a) grain boundary ductile intergranular fracture, (b) dimples on the grain boundary.

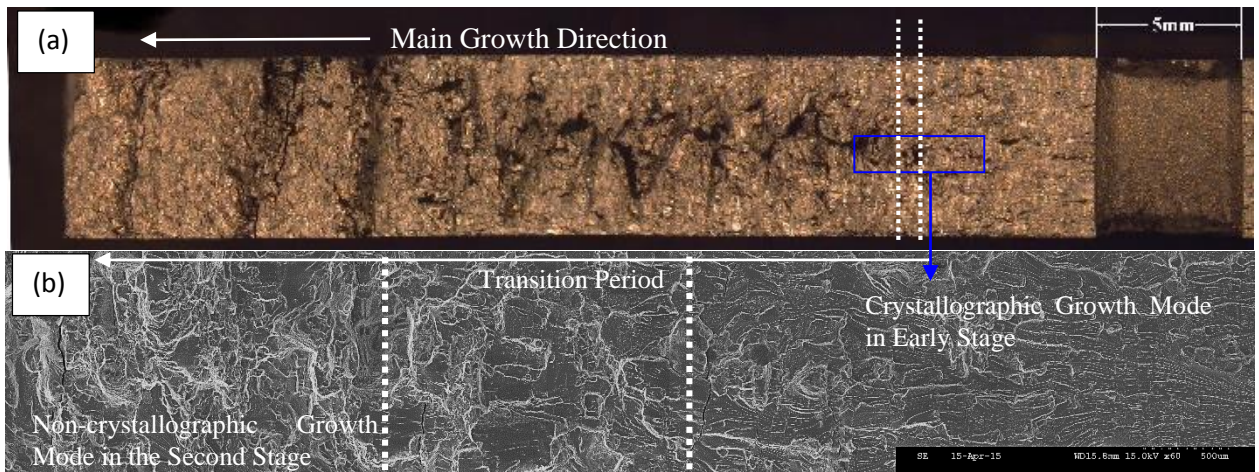
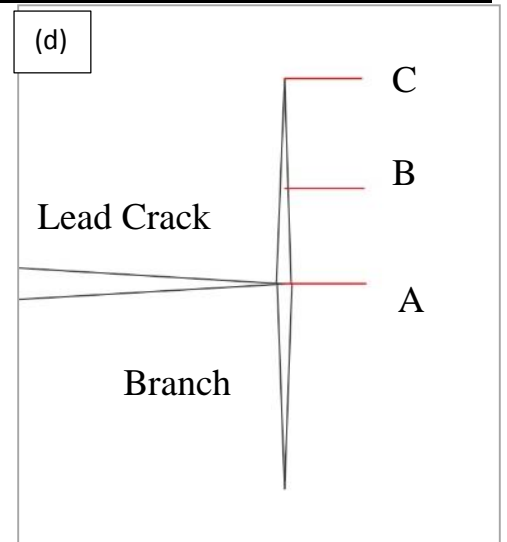
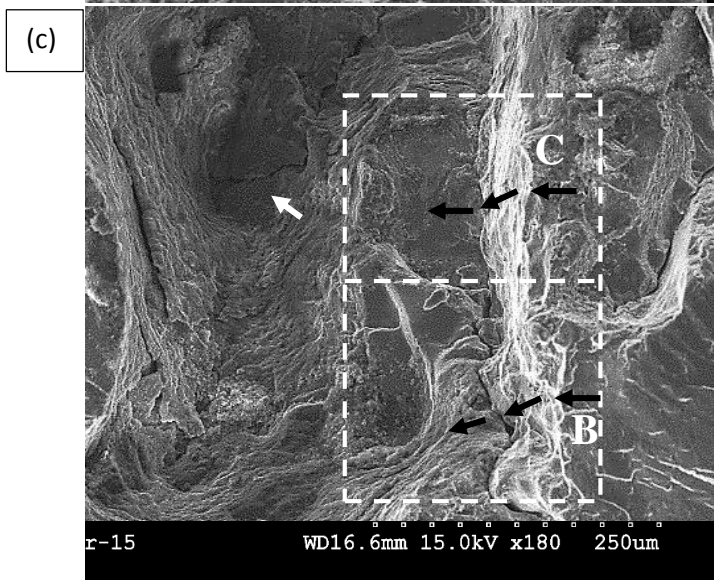
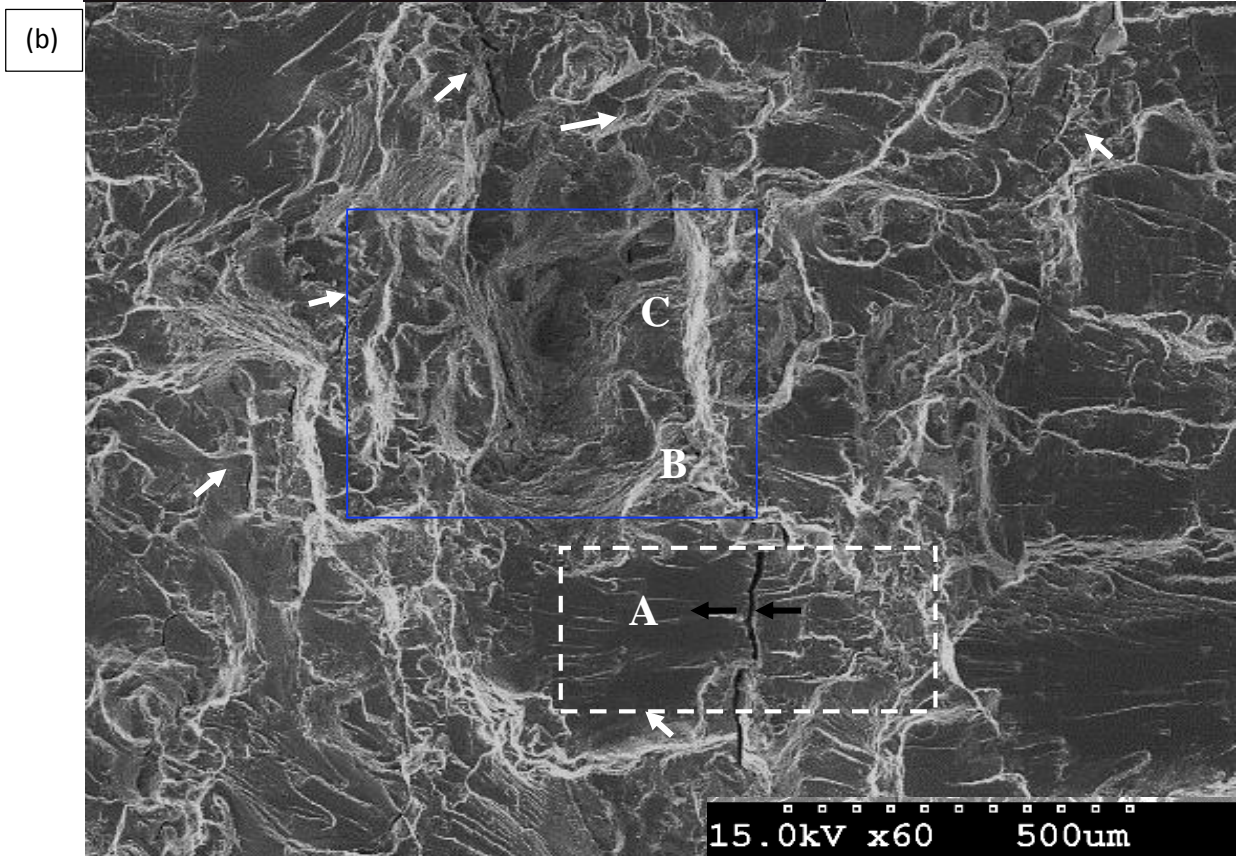
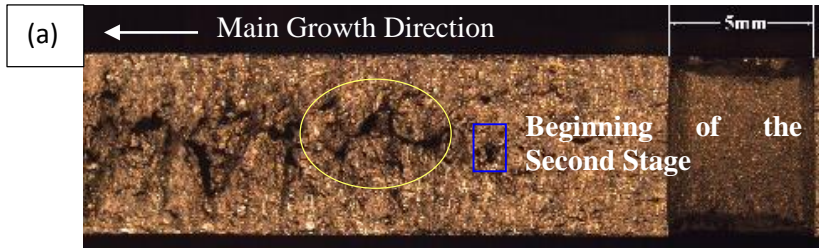


Figure 5.14 Morphology of fracture surface, (a) micrograph by stereo-optical microscope, (b) micrograph of the transition of the lead crack growth from crystallographic fracture (fatigue failure) to non-crystallographic fracture (overloading failure) by SEM.



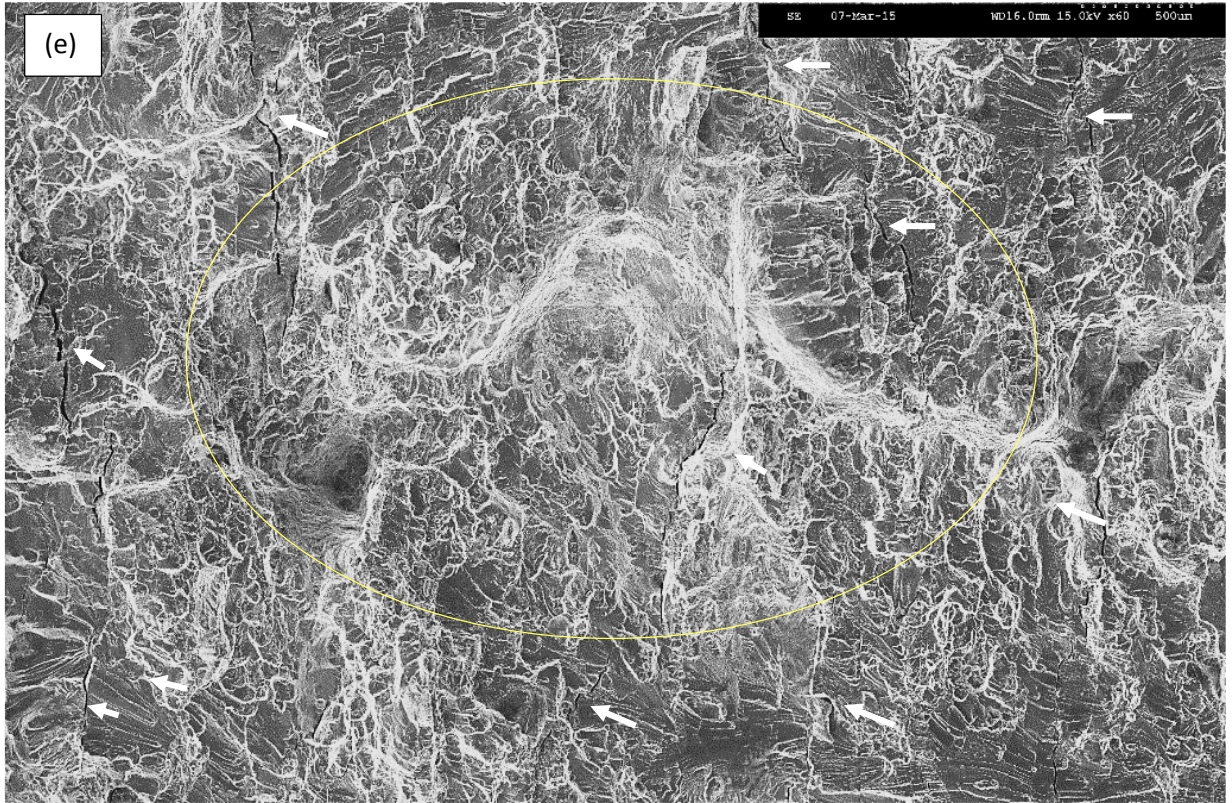


Figure 5.15 Micrographs of dark regions where many branches (white arrow pointed) gathered, (a) Morphology of fracture surface, (b) SEM of a small dark region (as rectangle in (a)), regarded as the beginning of the second stage of the lead crack growth, (c) high magnification of (b), (d) schematic representation of three ways of the lead crack re-propagation, (e) SEM of large dark region next to the one in (b), located as the elliptical shape of (a).

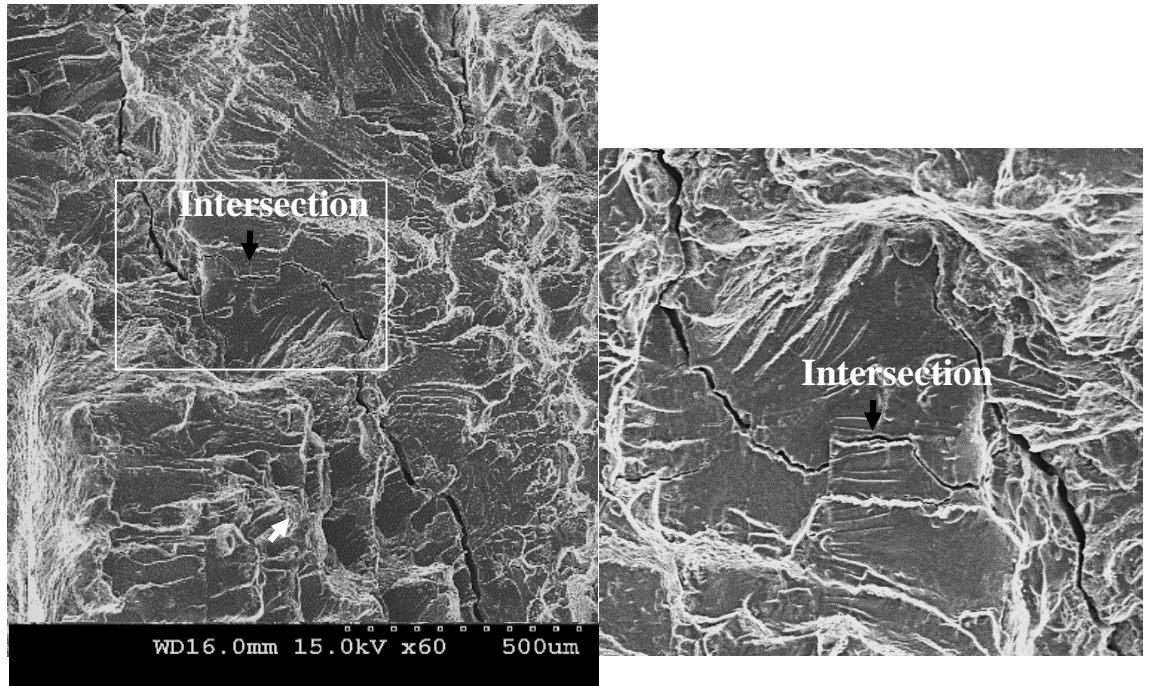


Figure 5.16 Interaction of the two individual branches.

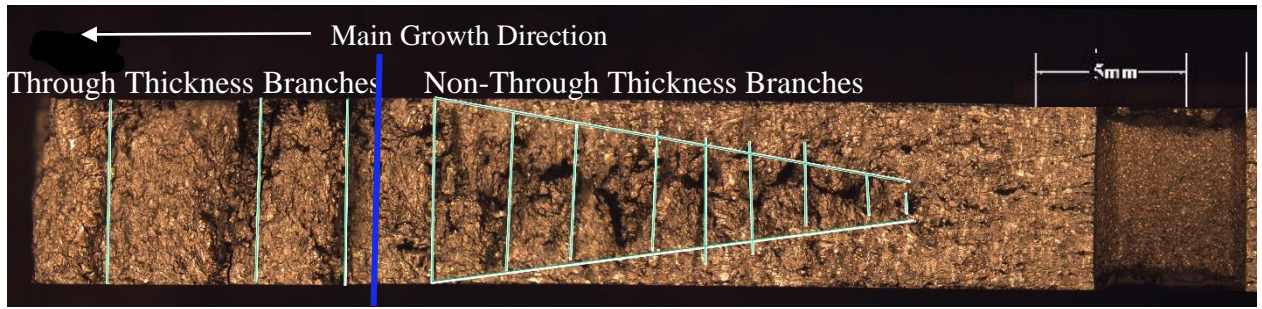
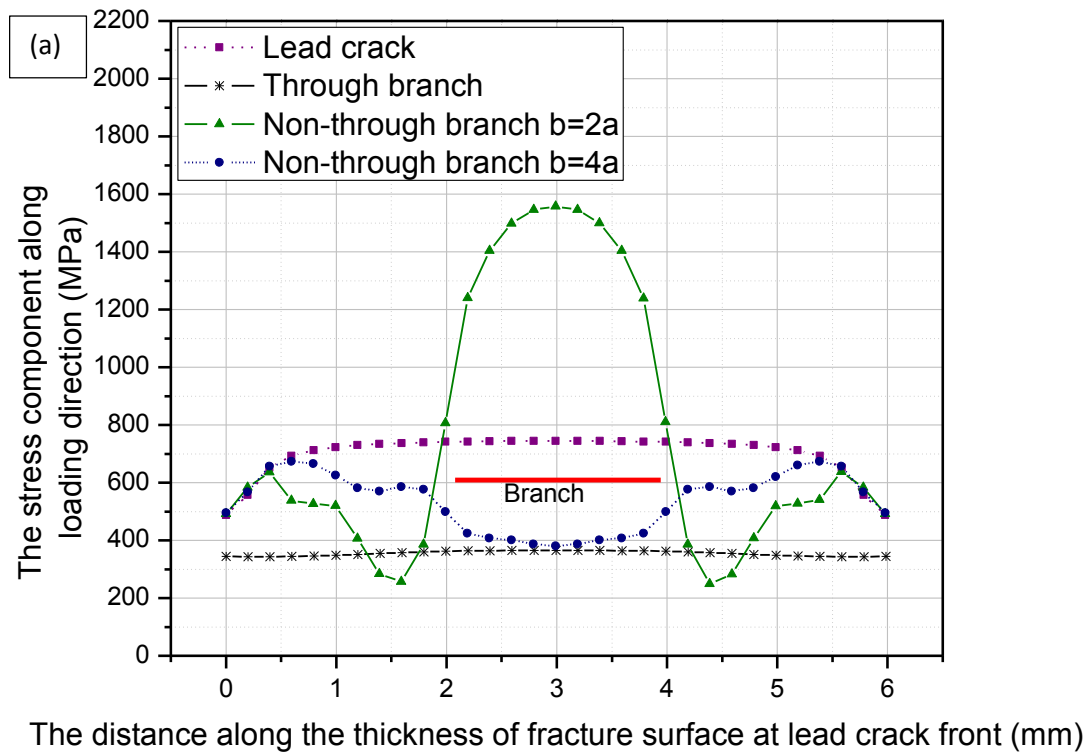
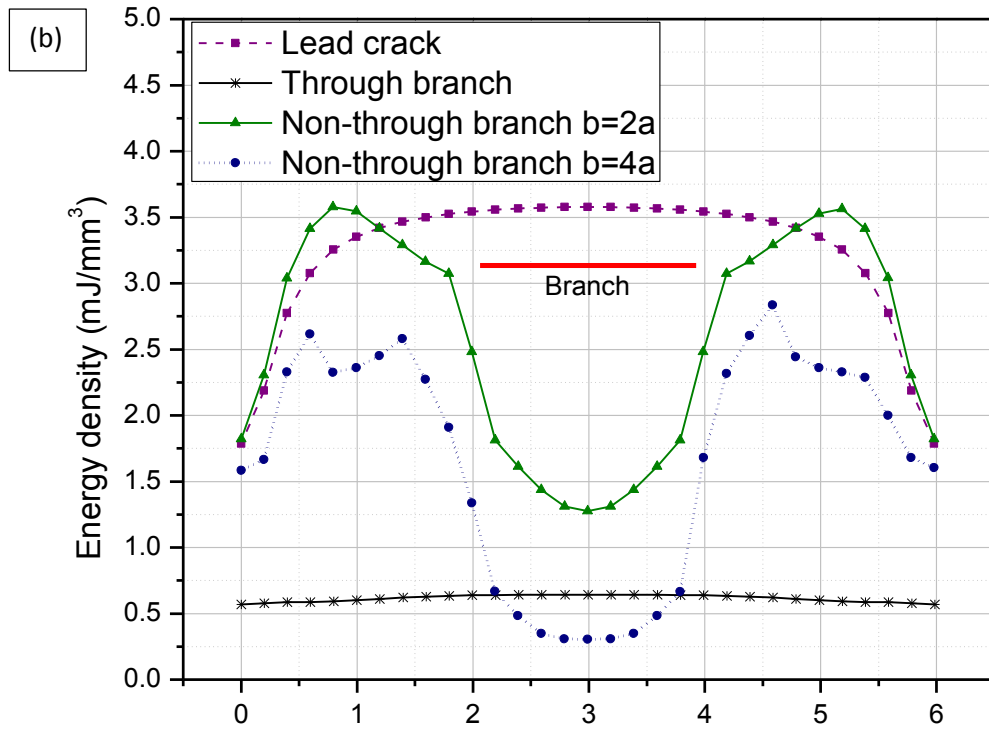


Figure 5.17 Growth behavior of branched crack.

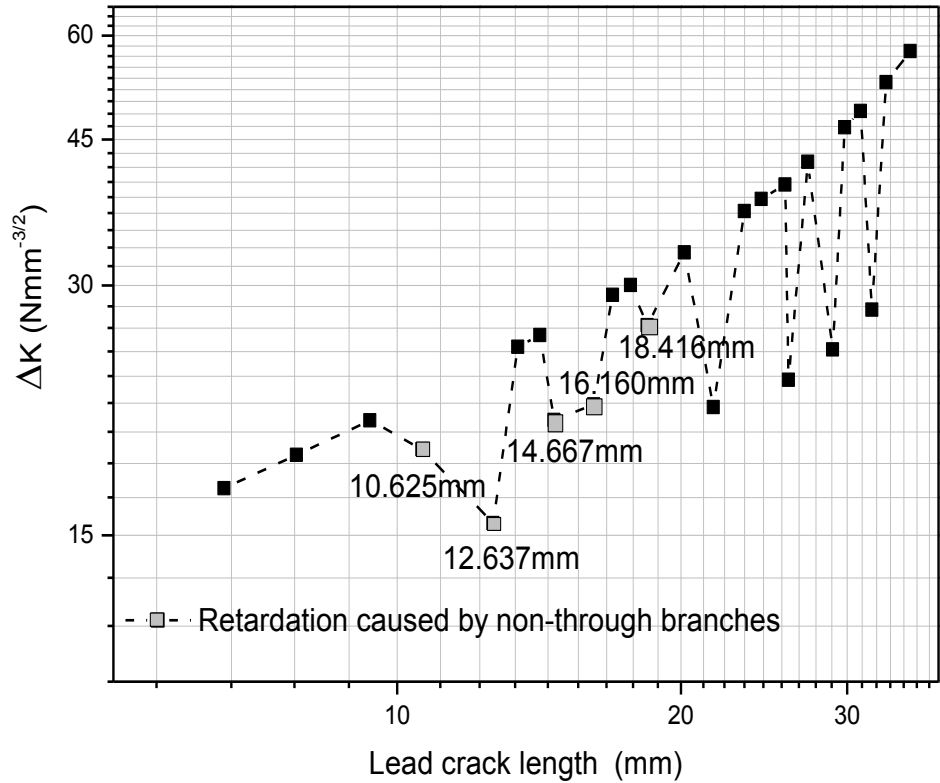




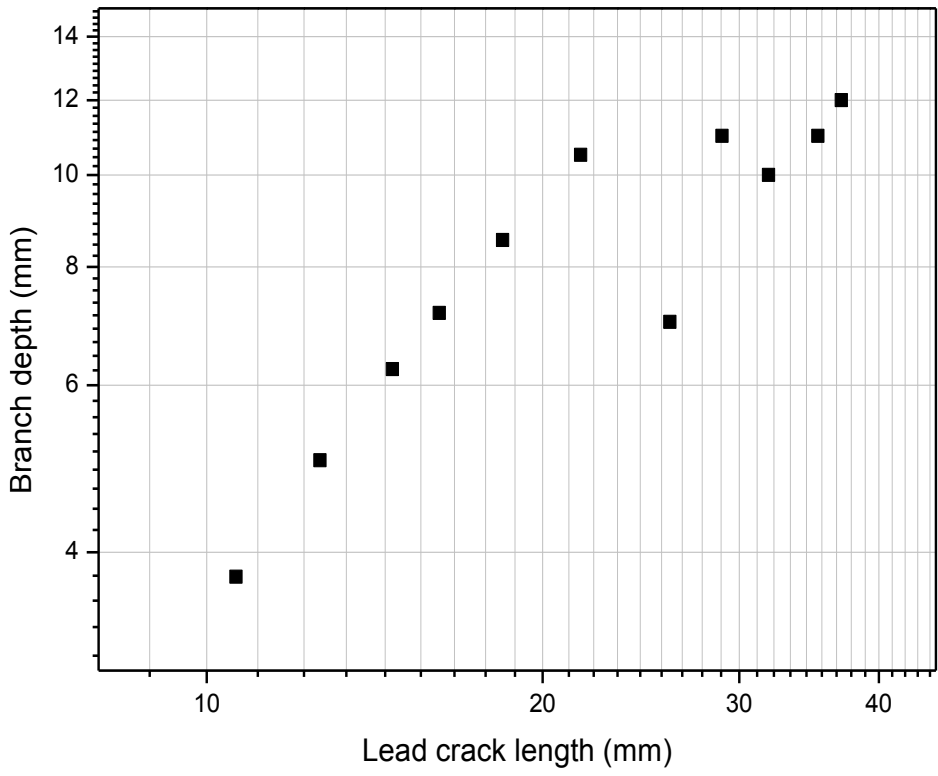
The distance along the thickness of fracture surface at lead crack front (mm)

Figure 5.18 The stress and elastic strain energy fields changing along the thickness of fracture surface of the plate at lead crack front, (a) stress component along the loading direction, σ_{yy} , (b) energy density.

(a)



(b)



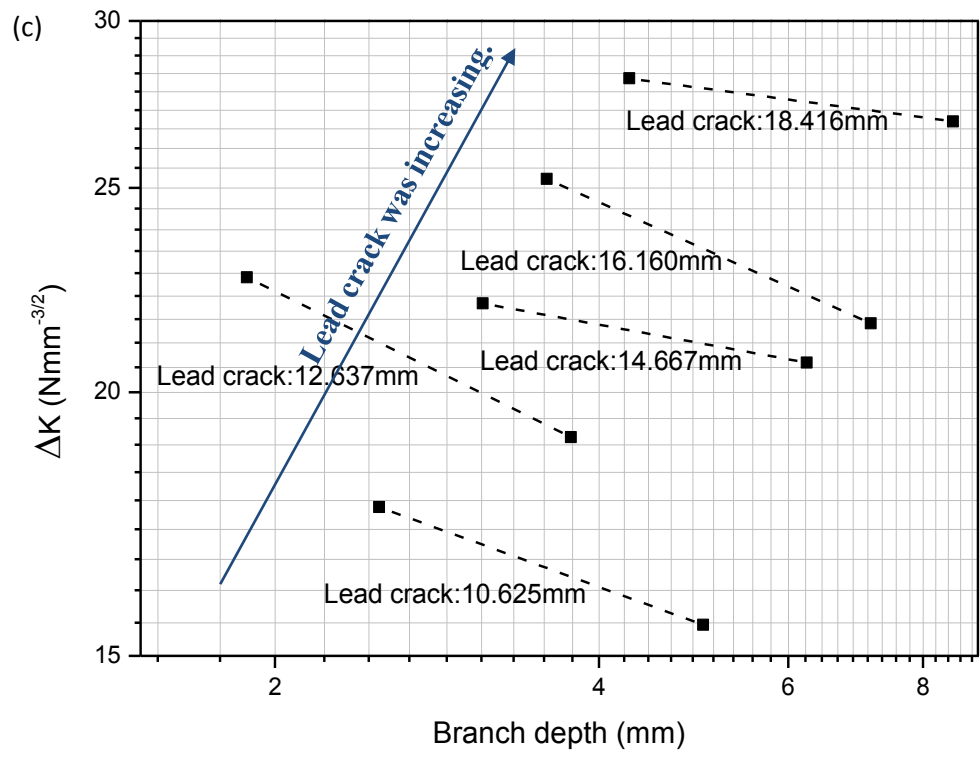


Figure 5.19 The effect of the depth of branch and the lead crack length on the driving force for fatigue crack propagation, ΔK , (a) ΔK vs. lead crack length, (b) branch depth vs. lead crack length, (c) ΔK vs. branch depth.

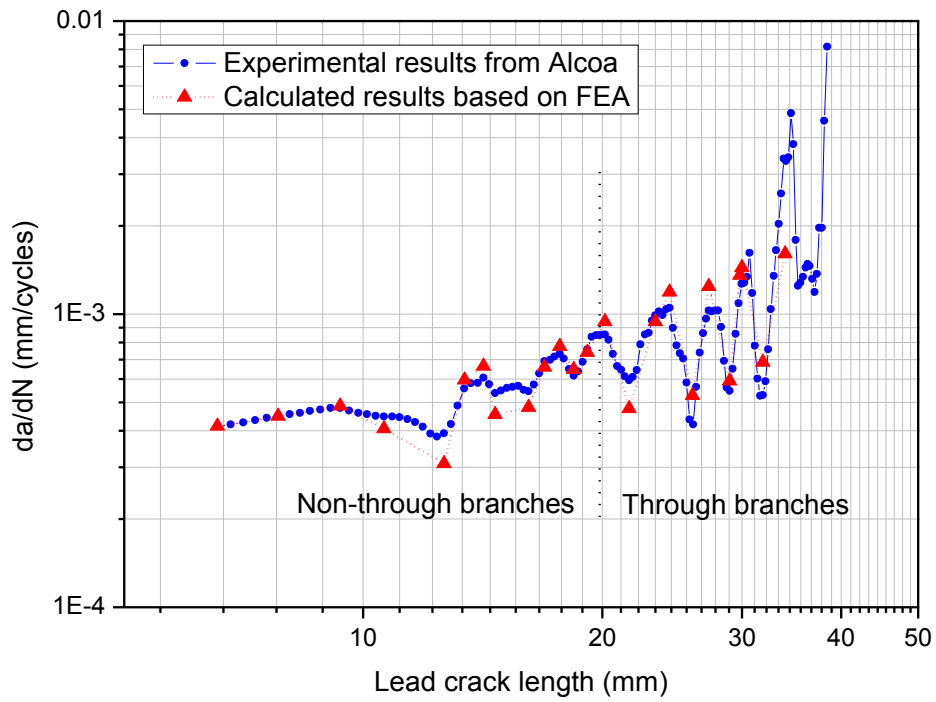


Figure 5.20 The comparison of the fatigue crack growth rate from the experiments and the predicted path with finite element simulations.

Chapter 6 Conclusions

6.1 Concluding remarks

A quantitative model which took into account the 3-D effects of pores on the local stress/strain fields was developed to quantify the fatigue weak-link density and strength distribution in an A713 Al alloy. The stochastic behaviors, including the reliability, of fatigue crack initiation were quantified at each applied cyclic stress in an A713 cast Al alloy, by analyzing the fatigue crack incubation lives at pores using a microscopic scale Manson-Coffin equation in the model with single-sized and multi-sized pores, respectively. A detailed fractographic and microstructural study was also conducted to characterize the behavior and mechanisms of fatigue crack branching in thick commercial 7050-T7651 aluminum plates in the L-S orientation. It was found that the combination of the precipitate-free zone occurring along the grain boundaries and the triaxle stress field in the vicinity of the crack tip was responsible for crack branching in the alloy plate. A 3-D finite element model which took into account the effects of a non-through/through thickness branched crack at the lead crack tip on the driving force for crack growth was consequently developed to simulate the influence of branching on the crack growth behavior. All the conclusions are summarized as follows:

- 1) A 3-D FEA method was used to quantitatively analyze the relationship of pore position in depth with stress/strain concentration, driving force for fatigue crack nucleation and fatigue crack incubation life, respectively, at various applied cyclic stresses for a pore of 15 μm in diameter.
- 2) FEA results demonstrated that both stress/strain concentration and driving force as a function of pore depth in the free surface were increased with increase in the applied cyclic stress and strain. Higher applied stress and strain led to shorter crack incubation life, and the incubation life was lowered when a pore was located closer to the surface.
- 3) The minimum critical pore size for fatigue crack initiation in the surface was determined to be about 11 μm in diameter by FEA simulation and matching to the experimentally measured fatigue life at the cyclic maximum stress of 100% yield stress in the A713 Al alloy.
- 4) The quantitative 3-D pore-sensitive model developed in this work took into account the 3-D effects of pores on fatigue crack initiation, and was capable of quantification of fatigue weak-link density and strength distribution in A713 Al cast alloys. It was validated by the

experimentally measured fatigue weak-link density and strength distribution in A713 Al alloys.

- 5) The model also demonstrated that the crack initiation rate at pores in surface was a Weibull function of the applied cyclic stress, which was consistent with the experimental results.
- 6) With increase in number density of pores, the crack population was increased, but crack initiation rate remained unchanged. The crack initiation rate was increased with increase of pore size (same area fraction of 2.826%) in the model, though the number density was lowered due to larger pore sizes.
- 7) The density and strength distribution of fatigue weak-links could be determined by fitting the curve of the crack initiation rate vs stress using a Weibull function. These results were simulated using both single- and multi-sized pores in the model, respectively, with the multi-sized pores giving rise to more consistent results with the experimentally measured ones. The difference in the peak value of the strength distribution of fatigue weak-links between the simulated and the experimental results was reduced from 20% using the single-sized pores to 1.8% by multi-sized pores.
- 8) The model developed in this work was also used to simulate the stochastic behaviors of multi-site crack nucleation by predicting the crack incubation lives at detrimental pores in the A713 cast Al alloy.
- 9) The crack initiation life was increased with decrease in cyclic stress, e.g., at a maximum cyclic stress just above the fatigue limit (70% yield strength), it could be over 96% the total fatigue life, compared to 69% at 110% yield strength.
- 10) The larger scatter was predicted in incubation life spectra at higher applied stress.
- 11) The reliability of fatigue crack initiation was quantified using the model at each applied cyclic stress in an A713 cast Al alloy. The probability of fatigue crack initiation was characterized by a two-parameter Weibull function, i.e., with 10,000 cyclic loading, the survival probability for crack initiation was 72% at 110% yield strength, and was 99% at 50% yield strength.
- 12) Crack branching along the loading direction (L direction) in an AA7050 Al alloy thick plate was the major factor responsible for the retardation of fatigue crack growth.

- 13) The width of precipitate-free zones was $\sim 0.05\text{-}0.15\ \mu\text{m}$ and the precipitates within the PFZ at grain boundaries were $\sim 60\ \text{nm}$ in length, which probably led to grain boundary dimple fracture and sequent fatigue crack branching parallel to L direction with the lamellar, columnar grain structure.
- 14) The transition of the lead crack growth from a crystallographic growth mode (fatigue fracture) to the non-crystallographic mode (overloading fracture) was observed at ΔK of $\sim 17\ \text{MPa}\sqrt{\text{m}}$.
- 15) A few non-through thickness branches were formed first at the mid-thickness plane. The first crack branching through the thickness occurred at ΔK greater than $30\ \text{MPa}\sqrt{\text{m}}$ and the lead crack longer than $\sim 20\ \text{mm}$.
- 16) Intergranular fracture was observed in the branched cracks, mainly due to the precipitate-free zones along grain boundaries in the Al alloy plate.
- 17) The results obtained from the finite element simulation demonstrated that ΔK for crack branching was mainly increased as increasing the length of lead crack, while the lead crack was significantly retarded where branching occurred parallel to the load direction. This was consistent with experimental results.
- 18) The ΔK for the lead crack was decreased as increase in depth of the branched crack ahead of the lead crack tip.

6.2 Suggestions for Future Work

It may still be desirable to develop a full-sized quantitative pore-sensitive model with experimentally measured pore size distribution for quantification of fatigue multi-site crack nucleation behaviors. A feasible method is trying to find the relationship between the pore size and the driving force by simulating one or two additional pores with each position at each stress level. With more pores, it is possible to fully quantify the pore size effects. Besides, the critical minimum pore size for fatigue crack nucleation at each stress level can be investigated as well. After developing the full-sized pore model, it may be possible to propose algorithms that can combine the Matlab program and FE codes of ABAQUS for quantifying the multi-site crack nucleation, which will be remarkably significant for exploring many other effects of pores in the materials. Based on the prediction of crack incubation life spectrum, the reliability of fatigue failure can be calculated if there is a reliable method to predict the short crack propagation life, which will be especially helpful for fatigue design

and alloy manufacturing. The technique can be extended for quantifying the effects of particles in high performance steels and high strength wrought aluminum alloys by replacing the pore with a spherical ball. Another important factor can be considered in future work is the effects of clustering in cast aluminum alloys since cluttering can cause crack initiation when the pore density is high.

As far as thick aluminum alloy plates are extensively used in aerospace applications, it would be interesting to conduct further work on simulating the crack branching behaviors with PFZs, in order to fully understand the mechanism of branching along grain boundaries. Since there is almost no precipitates within the PFZs, it is reasonable to simplify a PFZ as a very thin and soft layer vertical ahead of the lead crack tip during the finite element modeling. A bilayer model (sandwich structure) would be then constructed by tying the soft layer/PFZ and the neighboring grains/matrix together. The material properties of pure aluminum can be used for the softer layer. Therefore, the driving force for crack branching along PFZ would be calculated. Besides, the length of branch and the crack growth direction can be predicted by calculating the fatigue parameters in Fatemi- Socie critical plane criterion [68] and S-W-T criterion [107].

References

- [1] J. Schijve, *Fatigue of Structures and Materials* 2nd Edition, 2009.
- [2] W.A.J. Albert, *Archive für Mineralogie Geognosie Bergbau und Hüttenkunde*, 10 (1838) 215-234.
- [3] W.J.M. Rankine, *Minutes of the Proceedings of the Institution of Civil Engineers*, Thomas Telford-ICE Virtual Library, 1843, pp. 105-107.
- [4] P. Morin, *Journal für Praktische Chemie*, 58 (1853) 483-485.
- [5] A. Wöhler, *Zeitschrift für Bauwesen*, 10 (1860) 160-161.
- [6] F. Braithwaite, *Minutes of the Proceedings of the Institution of Civil Engineers*, Thomas Telford-ICE Virtual Library, 1854, pp. 463-467.
- [7] H. Gerber, *Bestimmung der zulässigen spannungen in eisen-constructionen*, Wolf, 1874.
- [8] G. Britain., *Report of the Commissioners Appointed to Inquire Into the Application of Iron to Railway Structures*, William Clowes and sons, 1849.
- [9] J. Ewing, J. Humfrey, *Philosophical Transactions of the Royal Society of London. Series A, Containing Papers of a Mathematical or Physical Character*, 200 (1903) 241-250.
- [10] O. Basquin, *Proc. Astm*, 1910, pp. 625-630.
- [11] S.S. Manson, "Behavior of materials under conditions of thermal stress." (1954).
- [12] L.F. Coffin Jr, *Knolls Atomic Power Lab.*, 1953.
- [13] C.E. Inglis, *Spie Milestone series MS*, 137 (1997) 3-17.
- [14] A.A. Griffith, *Philosophical transactions of the royal society of london. Series A, containing papers of a mathematical or physical character*, 221 (1921) 163-198.
- [15] P. Paris, F. Erdogan, *Journal of basic engineering*, 85 (1963) 528-533.
- [16] J. Schijve, *Fatigue of structures and materials*, Springer, 2001.
- [17] J. Schijve, *Fatigue crack closure: observations and technical significance*, *Mechanics of fatigue crack closure*, ASTM International, 1988.
- [18] P. Forsyth, *Nature*, 171 (1953) 172-173.
- [19] P.J.E. Forsyth, *Blackie and Sonltd., London*, 200 P, (1969).
- [20] A.S. Cheng, C. Laird, *Fatigue & Fracture of Engineering Materials & Structures*, 4 (1981) 331-341.
- [21] R. Keith, J. Gilman, *Acta Metallurgica*, 8 (1960) 1-10.
- [22] P. Charsley, M. Desvaux, *Materials Science and Engineering*, 4 (1969) 211-220.
- [23] J. Antonopoulos, L. Brown, A. Winter, *Philosophical Magazine*, 34 (1976) 549-563.
- [24] K. Tanaka, T. Mura, *Journal of Applied Mechanics*, 48 (1981) 97-103.
- [25] H.T. Pang, P.A.S. Reed, *Int. J. Fatigue*, 25 (2003) 1089-1099.
- [26] O. Basquin, *Proc. ASTM*, 1910, pp. 625-630.
- [27] C. Kung, M. Fine, *Metallurgical Transactions A*, 10 (1979) 603-610.
- [28] S. Axter, W.B. Jones, D. Polonis, *Metallography*, 8 (1975) 425-438.

- [29] E. DeBartolo, B. Hillberry, *International Journal of Fatigue*, 20 (1998) 727-735.
- [30] M. Couper, A. Neeson, J. Griffiths, *Fatigue & Fracture of Engineering Materials & Structures*, 13 (1990) 213-227.
- [31] J. Grosskreutz, *Metallurgical Transactions*, 3 (1972) 1255-1262.
- [32] C. Laird, D. Duquette, *Corrosion Fatigue*, 2 (1972) 88-117.
- [33] M.A. Przystupa, R.J. Bucci, P.E. Magnusen, A.J. Hinkle, *International Journal of Fatigue*, 19 (1997) 285-288.
- [34] P.J. Laz, B.M. Hillberry, *International Journal of Fatigue*, 20 (1998) 263-270.
- [35] P.S. Pao, C.R. Feng, S.J. Gill, *Corrosion*, 56 (2000) 1022-1031.
- [36] D. Harlow, R. Wei, M. Wang, *Metallurgical and Materials Transactions A*, 37 (2006) 3367-3373.
- [37] Y. Jin, P. Cai, W. Wen, H. Nagaumi, B. Xu, Y. Zhang, T. Zhai, *Mater. Sci. Eng. A*, 622 (2015) 7-15.
- [38] H. Ammar, A. Samuel, F. Samuel, *Mater. Sci. Eng. A*, 473 (2008) 65-75.
- [39] H.R. Ammar, A.M. Samuel, F.H. Samuel, *Materials Science and Engineering: A*, 473 (2008) 58-64.
- [40] J.Z. Yi, Y.X. Gao, P.D. Lee, H.M. Flower, T.C. Lindley, *Metallurgical and Materials Transactions a-Physical Metallurgy and Materials Science*, 34A (2003) 1879-1890.
- [41] Y. Zhang, J. Xu, T. Zhai, *Mater. Sci. Eng. A-Struct.*, 527 (2010) 3639-3644.
- [42] Q.G. Wang, D. Apelian, D.A. Lados, *J. Light Met.*, 1 (2001) 73-84.
- [43] P. Forsyth, *Proceedings of the Crack Propagation Symposium*, 1961, pp. 76-94.
- [44] R. Ritchie, *International Metals Reviews*, 24 (1979) 205-230.
- [45] S. S, *International Metal Reviews*, 29 (1984) 445-475.
- [46] S. Suresh, *Fatigue of materials*, Cambridge university press, 1998.
- [47] H.H. Johnson, P.C. Paris, *Engineering Fracture Mechanics*, 1 (1968) 3-45.
- [48] R.P. Gangloff, R.S. Iascik, D.L. Icus, J.C. Ewman, *Journal of Aircraft*, 31 (1994) 720-729.
- [49] M. Joyce, M. Starink, I. Sinclair, *Materials & Design*, 93 (2016) 379-387.
- [50] J.J. Schubbe, *Engineering Fracture Mechanics*, 76 (2009) 1037-1048.
- [51] J.C. Ting, F.V. Lawrence, *Fatigue & Fracture of Engineering Materials & Structures*, 16 (1993) 631-647.
- [52] S. Benedictus-deVries, A. Bakker, G. Janssen, H. de Wit, *Journal of engineering materials and technology*, 126 (2004) 199-203.
- [53] A. Merati, *International Journal of Fatigue*, 27 (2005) 33-44.
- [54] T. Zhai, *Metallurgical and Materials Transactions A*, 37 (2006) 3139-3147.
- [55] Y. Jin, P. Cai, Q. Tian, T. Zhai, *Fatigue & Fracture of Engineering Materials & Structures*, 39 (2016) 696-711.
- [56] K. Gall, M.F. Horstemeyer, B.W. Degner, D.L. McDowell, J.H. Fan, *Int. J. Fract.*, 108 (2001) 207-233.

- [57] Y.X. Gao, J.Z. Yi, P.D. Lee, T.C. Lindley, *Fatigue Fract. Eng. Mater. Struct.*, 27 (2004) 559-570.
- [58] J. Fan, D.L. McDowell, M.F. Horstemeyer, K. Gall, *Engineering Fracture Mechanics*, 70 (2003) 1281-1302.
- [59] Y. Murakami, M. Endo, *International Journal of Fatigue*, 16 (1994) 163-182.
- [60] M.J. Caton, J.W. Jones, J.E. Allison, Use of small fatigue crack growth analysis in predicting the SN response of cast aluminum alloys, *Fatigue Crack Growth Thresholds, Endurance Limits, and Design*, ASTM International, 2000.
- [61] M. Todinov, *Materials Science and Engineering: A*, 255 (1998) 117-123.
- [62] Z. Xu, W. Wen, T. Zhai, *Metallurgical and Materials Transactions A*, 43 (2012) 2763-2770.
- [63] K. Tanaka, T. Mura, *Metallurgical Transactions A*, 13 (1982) 117-123.
- [64] T. Mura, Y. Nakasone, *Journal of Applied Mechanics*, 57 (1990) 1-6.
- [65] G. Venkataraman, Y. Chung, T. Mura, *Acta metallurgica et materialia*, 39 (1991) 2621-2629.
- [66] G. Venkataraman, Y. Chung, T. Mura, *Acta metallurgica et materialia*, 39 (1991) 2631-2638.
- [67] M. Kato, S. Onaka, T. Mori, T. Mura, *Scripta metallurgica*, 18 (1984) 1323-1326.
- [68] A. Fatemi, D.F. Socie, *Fatigue & Fracture of Engineering Materials & Structures*, 11 (1988) 149-165.
- [69] A. Fatemi, P. Kurath, *Journal of Engineering Materials and Technology*, 110 (1988) 380-388.
- [70] D. McDowell, ASM International, Member/Customer Service Center, Materials Park, OH 44073-0002, USA, 1996., (1996) 263-273.
- [71] D.L. McDowell, *International Journal of Fracture*, 80 (1996) 103-145.
- [72] D. McDowell, K. Gall, M. Horstemeyer, J. Fan, *Engineering Fracture Mechanics*, 70 (2003) 49-80.
- [73] Y. Xue, D. McDowell, M. Horstemeyer, M. Dale, J. Jordon, *Engineering Fracture Mechanics*, 74 (2007) 2810-2823.
- [74] W. Weibull, *Proc. R. Swed. Inst. Eng. Res.*, 151 (1939) 45.
- [75] A.M. Freudenthal, *Fracture*, 2 (1968) 591-619.
- [76] H.J. Sutherland, P.S. Veers, *Wind Energy*, 16 (1995) 83-90.
- [77] T. Delahay, T. Palin-Luc, *International journal of fatigue*, 28 (2006) 474-484.
- [78] D.B. Lanning, T. Nicholas, A. Palazotto, *International journal of fatigue*, 25 (2003) 835-841.
- [79] T. Zhai, *Metall. Mater. Trans. A*, 37A (2006) 3139-3147.
- [80] P.C. Gope, *J. Eng. Mater. Tech.*, 124 (2002) 421-427.
- [81] D.B. Lanning, T. Nicholas, A. Palazotto, *Int. J. Fatigue*, 25 (2003) 835-841.
- [82] Y.X. Zhao, *Mater. Sci. Eng. A*, 344 (2003) 229-239.
- [83] Y. Jin, P. Cai, Q. Tian, T. Zhai, *Fatigue Fract. Eng. Mater. Struct.*, In press (2016).
- [84] ASTM, STP, 744.
- [85] S. Thangjitham, R.W. Landgraf, *SAE Technical Paper*, 1992, pp. 225-235.
- [86] K. Sobczyk, B. Spencer Jr, *Random fatigue: from data to theory*, Academic Press, 2012.

- [87] P. Wirsching, Probabilistic fatigue analysis, Probabilistic structural mechanics handbook, Springer, 1995, pp. 146-165.
- [88] P.S. Veers, ASM International, Member/Customer Service Center, Materials Park, OH 44073-0002, USA, 1996., (1996) 295-302.
- [89] W. Weibull, Journal of applied mechanics, 103 (1951) 293-297.
- [90] D. Dumont, A. Deschamps, Y. Brechet, Materials Science and Engineering: A, 356 (2003) 326-336.
- [91] E. Hornbogen, H. Kreye, Journal of Materials Science, 17 (1982) 979-988.
- [92] M. Raghavan, Metallurgical Transactions A, 11 (1980) 993-999.
- [93] M. Gräf, E. Hornbogen, Acta Metallurgica, 25 (1977) 883-889.
- [94] A.K. Vasudévan, R.D. Doherty, Acta Metallurgica, 35 (1987) 1193-1219.
- [95] A. Bowen, Materials Science and Technology, 6 (1990) 1058-1071.
- [96] J. Lindigkeit, A. Gysler, G. Lütjering, Metallurgical Transactions A, 12 (1981) 1613-1619.
- [97] T. Zhai, A. Wilkinson, J. Martin, Acta materialia, 48 (2000) 4917-4927.
- [98] T. Zhai, X. Jiang, J. Li, M. Garratt, G. Bray, International Journal of Fatigue, 27 (2005) 1202-1209.
- [99] D. Catoor, K. Kumar, Philosophical Magazine, 88 (2008) 1437-1460.
- [100] W. Schaefer, M. Marx, H. Vehoff, A. Heckl, P. Randelzhofer, Acta Materialia, 59 (2011) 1849-1861.
- [101] W. Tayon, R. Crooks, M. Domack, J. Wagner, A. Elmustafa, Exp Mech, 50 (2010) 135-143.
- [102] G.C. Sih, International Journal of fracture, 10 (1974) 305-321.
- [103] C.-F. Shih, Fracture Analysis: Proceedings of the 1973 National Symposium on Fracture Mechanics, Part II, ASTM International, 1974.
- [104] S. Suresh, C. Shih, International Journal of Fracture, 30 (1986) 237-259.
- [105] I. Sinclair, P.J. Gregson, Materials Science Forum, Trans Tech Publ, 1997, pp. 175-180.
- [106] M. Brown, K. Miller, Proceedings of the Institution of Mechanical Engineers, 187 (1973) 745-755.
- [107] K. Smith, T. Topper, P. Watson, Journal of materials, 5 (1970) 767-778.
- [108] Y. Jiang, H. Sehitoglu, Journal of Tribology, 116 (1994) 577-587.
- [109] C.-C. Chu, Journal of Engineering Materials and Technology, 117 (1995) 41-49.
- [110] G. Glinka, G. Shen, A. Plumtree, Fatigue & Fracture of Engineering Materials & Structures, 18 (1995) 37-46.
- [111] G. Glinka, G. Wang, A. Plumtree, Fatigue & fracture of engineering materials & structures, 18 (1995) 755-764.
- [112] Y. Jiang, Fatigue and fracture of engineering materials and structures, 23 (2000) 19-32.
- [113] A.C. Miranda, M. Meggiolaro, J. Castro, L. Martha, Proc Second MIT Conf on Computational Fluid and Solid Mechanics, Cambridge, MA, USA, 2003, pp. 460-463.
- [114] M.A. Meggiolaro, A.C.O. Miranda, J.T.P. Castro, L.F. Martha, Engineering Fracture Mechanics, 72 (2005) 2647-2671.

- [115] T. Pardoen, D. Dumont, A. Deschamps, Y. Brechet, *Journal of the Mechanics and Physics of Solids*, 51 (2003) 637-665.
- [116] H. Dijkers, TU Delft, Delft University of Technology, 2015.
- [117] H. Kuhn, D. Medlin, ASM International, Member/Customer Service Center, Materials Park, OH 44073-0002, USA, 2000. 998, (2000).
- [118] T. Zhai, Y.G. Xu, J.W. Martin, A.J. Wilkinson, G.A.D. Briggs, *Int. J. Fatigue*, 21 (1999) 889-894.
- [119] D. McMullan, *Scanning*, 17 (1995) 175-185.
- [120] J. Goldstein, D.E. Newbury, P. Echlin, D.C. Joy, A.D. Romig Jr, C.E. Lyman, C. Fiori, E. Lifshin, *Scanning electron microscopy and X-ray microanalysis: a text for biologists, materials scientists, and geologists*, Springer Science & Business Media, 2012.
- [121] C.A. Volkert, A.M. Minor, *MRS bulletin*, 32 (2007) 389-399.
- [122] L. Giannuzzi, F. Stevie, *Micron*, 30 (1999) 197-204.
- [123] L. Bischoff, W. Pilz, T. Ganetsos, R. Forbes, C. Akhmadaliev, *Ultramicroscopy*, 107 (2007) 865-868.
- [124] S. Reyntjens, R. Puers, *Journal of Micromechanics and Microengineering*, 11 (2001) 287.
- [125] J. Gierak, *Semiconductor science and technology*, 24 (2009) 043001.
- [126] D.L. Logan, *A first course in the finite element method*, Cengage Learning, 2011.
- [127] Y. Jin, P. Cai, Q.B. Tian, C.Y. Liang, D.J. Ke, G. Wang, T. Zhai, *Fatigue & Fracture of Engineering Materials & Structures*, 39 (2016) 696-711.
- [128] L. Yang, P. Cai, Z. Xu, Y. Jin, C. Liang, T. Zhai, *Int. J. Fatigue*, In Press. DOI: <http://dx.doi.org/10.1016/j.ijfatigue.2016.11.035> (2016).
- [129] U. Krupp, *Fatigue crack propagation in metals and alloys: microstructural aspects and modelling concepts*, John Wiley & Sons, 2007.
- [130] K. Tokaji, S. Takafuji, K. Ohya, Y. Kato, K. Mori, *Journal of Materials Science*, 38 (2003) 1153-1159.
- [131] Y. Hong, Z. Lei, C. Sun, A. Zhao, *Int. J. Fatigue*, 58 (2014) 144-151.
- [132] W. Wen, T.G. Zhai, *Philosophical Magazine*, 91 (2011) 3557-3577.
- [133] W. Wen, A.H.W. Ngan, Y. Zhang, B. Xu, T. Zhai, *Materials Science and Engineering: A*, 564 (2013) 97-101.
- [134] E.A. Starke Jr, J.T. Staley, *Progress in Aerospace Sciences*, 32 (1996) 131-172.
- [135] A. Heinz, A. Haszler, C. Keidel, S. Moldenhauer, R. Benedictus, W.S. Miller, *Materials Science and Engineering: A*, 280 (2000) 102-107.
- [136] D.L.D. J. Lankford, *Advances in fracture research*, 2 (1981) 899-906.
- [137] S. Suresh, *Metallurgical Transactions A*, 14 (1983) 2375-2385.
- [138] S. Suresh, *Engineering Fracture Mechanics*, 18 (1983) 577-593.
- [139] K. Shen, J.-l. Chen, Z.-m. Yin, *Transactions of Nonferrous Metals Society of China*, 19 (2009) 1405-1409.
- [140] Z.-H.J. C. T. Sun, *Fracture Mechanics*, Elsevier Science, 2011, pp. 105-107.
- [141] P.C. Paris, M.P. Gomez, W.E. Anderson, *The trend in engineering*, 13 (1961) 9-14.

- [142] S. Suresh, *Engineering Fracture Mechanics*, 21 (1985) 453-463.
- [143] H. Dijkers, *Thesis of Master Science, Delft University of Technology*, (2015).
- [144] P. Unwin, G. Smith, *J Inst Metals*, 97 (1969) 299-310.
- [145] J.D. Embury, E. Nes, *Zeitschrift fuer Metallkunde/Materials Research and Advanced Techniques*, 65 (1974) 45-55.
- [146] G. Ludtka, D. Laughlin, *Metallurgical Transactions A*, 13 (1982) 411-425.
- [147] J.J. Schubbe, *Engineering Failure Analysis*, 16 (2009) 340-349.

VITA

Place of Birth: Xining, Qinghai, China

Education:

- University of Kentucky, Lexington, KY
Jan 2012-Dec 2016 Ph.D. Candidate, Materials Science and Engineering
- University of Science and Technology Beijing, Beijing, China
Sept 2009-Jun 2011 M.S., Solid Mechanics
- University of Science and Technology Beijing, Beijing, China
Sept 2005-Jun 2009 B.S., Materials Science and Engineering

Research:

- 3-D models for quantifying the fatigue multi-site initiation in an cast Al alloy
- 3-D Model for fatigue crack branching in an Al alloy thick plate
- A model for effects of particle on crack nucleation behavior in a high strength steel
- Effects of constituent particles on fatigue crack nucleation in an Al plate
- Fracture mechanism to stress-corrosion cracking in an Mg alloy

Professional Service:

- Reviewer of Fatigue & Fracture of Engineering Materials & Structures

Publications:

- L. Yang, Y. Jin, P. Cai, F. X. Yin, Q. Li and T. Zhai, “Quantification of Fatigue Weaklinks in High Strength Al Alloys”, *Materials Science Forum*, Vol. 877, pp. 427-434, 2017
- L. Yang, Y. Jin, Z. Xu, P. Cai and T. Zhai, “A 3-D model for quantification of fatigue weak-links strength in an A713 cast aluminum alloy”, *International Journal of Fatigue*, 2016, <http://dx.doi.org/10.1016/j.ijfatigue.2016.11.035>
- L. Yang, Y. Jin, Z. Xu and T. Zhai, “Simulating the stochastic behaviors of fatigue crack incubation in an A713 cast aluminum alloy based on a multi-sized pore-sensitive model” (To be submitted)
- L. Yang, Y. Jin and T. Zhai, “Fatigue crack branching in 7050-T7651 aluminum thick plates” (To be submitted)
- L. Yang, Y. Nie, X. Li and T. Zhai, “Distribution of particle size and 3-D effect of particle on fatigue crack initiation in high strength steel” (In preparation)

- Y. Jin, L. Yang, P. Cai and T. Zhai, “3-D effects of anisotropic fatigue crack initiation at constituent particle in an AA7075 T651 Al alloy plate using focused ion beam combined with EBSD, AFM and Nano-indentation” (To be submitted)

Academical Oral Presentations:

- L. Yang, Z. Xu, Y. Jin, etc. “A 3-D Model for quantification of fatigue weak-link strength in an A713 cast aluminum alloy”, *TMS 2016 Annual Meeting*, Nashville, TN, 02/2016
- L. Yang, “A 3-D Model for quantification of fatigue weak-link strength in an A713 cast aluminum alloy”, *TMS 2016 Annual Meeting*, Nashville, TN, 02/2016 (poster)
- Y. Jin, L. Yang, P. Cai and T. Zhai, etc. “A 3-D understanding of the anisotropy in fatigue crack nucleation in an AA7075 T651 Al alloy plate”, *TMS 2016 Annual Meeting*, Nashville, TN, 02/2016 (invited)
- L. Yang, Y. Jin, etc. “Simulation of fatigue crack branching in AA7050 T7651 Al alloy thick plates”, *TMS 2015 Annual Meeting*, Orlando, FL, 03/2015
- Y. Jin, L. Yang, T. Zhai and T. Leonhardt. “Textures in pure Mo processed by different thermo-mechanical processes”, *TMS 2015 Annual Meeting*, Orlando, FL, 03/2015
- Lin Yang and T. Zhai, “Quantification of fatigue weak-links”, *TMS 2014 Annual Meeting*, San Diego, CA, 03/2014
- Lin Yang, Y. Jin and T. Zhai. “A 3-D Model for quantification of multi-site crack nucleation behaviors in an A713 cast aluminum alloy”, *2016 ASM Chapter meeting*, Lexington, KY, 11/2016 (invited)